THESE DE DOCTORAT DE L'UNIVERSITE PARIS 13

INSTITUT GALILEE

Mention **Sciences de I'Ingénieur**

Option **Génie des Procédés**

Présentée et soutenue publiquement par

NGUYỄN Thị Hằng Nga

Pour obtenir le titre de

Docteur de l'Université Paris 13

Elaboration and modifications of nanofibrous Al_2O_3

Soutenue le 28 september 2016

Devant le jury composé de:

Abderrahmane BOUABELLOU	Professeur, Université Constantine, Algérie	Rapporteur
Eduard FELDBACH	Chercheur, Université de Tartu, Estonie	Rapporteur
Giuseppe LEO	Professeur, Université Paris 7	Examinateur
Jean-Louis VIGNES	Professeur émérite, Université Paris-Est Creteil	Examinateur
Khay CHHOR	Professeur, Université Paris 13	Examinateur
Andrei KANAEV	Directeur de Recherche CNRS	Directeur de thèse
Mohamed AMAMRA	Assist. Professeur, Université Paris 13	Encadrant de thèse

Laboratoire des Sciences de Procédés et des Matériaux CNRS UPR 3407

Acknowledgements

The PhD work has been performed at LSPM UPR3407 CNRS (*Laboratorie des Sciences des Procédés et des Matériaux*) at the Paris 13 University. During my research work, I have received the help and support of very kind people around me, and my work cannot complete without them.

First of all, I am much obliged to my thesis supervisor Director of Research (CNRS) Andrei KANAEV for his patience and guiding during my work. His superior knowledge extended my vision in research work and helped me to get directly goals. I am most grateful to my second supervisor, assistant Professor Mohamed AMAMRA, for many advices and instructions given to me and for making much experimental work together during 3 years.

I would like to pay my heartfelt gratitude to Professor Anatole KHODAN, he has given me the original knowledge about alumina and valuable advices on my research work.

I want to thank Professor Jean-Louis VIGNES, who was called by a funny name 'father of alumina', for his fundamental knowledge about alumina he provided to me.

I want to thank Professor Giuseppe LEO and Dr. Oleksandr STEPANENKO of University Paris 7, who have guided me in dielectric measurements of samples, processing and explanations of data.

Also, I wish to extend my thanks to all members of the examination committee: Professor Abderrahmane BOUABELLOU, Dr. Eduard FELDBACH and Professor. Khay CHHOR.

Many thanks to the entire LSPM staff members, who shared professional knowledge and provided personal support to me. Therein, I am grateful to technicians Ovidui BRINZA and Valéri BOCKELEE, they took their time to measure many samples for me. Especially, I want to thank members of NINO group: Mamadou TRAORE, Sana LABIDI, Khley CHENG, Ana Paola DIAZGOMEZ TREVINO, Patrick PORTES, Abdelkader RAHMANI and Didier FANOU. Other thanks to members in my office: Sarah DINE, Nassima OUAR, Amine BOUSSADI, Benoit BAUDRILLART, Hazan AL MEHEDI, and thanks for an excellent time we passed together, which I will always remember.

I would like to express my gratitude to Assoc. Prof. H.N. TRAN and Dr. T.H.L. NGHIEM and members of NanoBio-Photonics group of Institute of Physic of Vietnam

Academic of Science and Technology (VAST), who have guided and advised me in the beginning of my research work.

I want to thank my dear friends in Vietnam: THU, MAI, NGỪNG, QUỲNH, VÂN ANH, THÀNH, KHANG, HUYỀN QUÂN and THANH AN for their greetings and encouragement.

Sincerely thanks to my dear friends in Paris 13 University and in France: LỘC PHƯỢNG, TRUNG, QUANG, DUNG, TRANG, NHUNG, CHIẾN, NGHĨA, NGUYÊN, HOÀNG, VIỆT, HIẾU, HUYỀN, NGÀ HOÀN, KHUÊ, HẢI, TUẤN, ĐIỆP, NHẬT, THI, GIA, ÂN, BÌNH, CHIẾN, HUYỀN, KIM HOÀNG, YẾN, THÁI, TRỌNG, KỴ, THỦY, THỌ, LIÊN, MINH… they are members in a big family, and I really appreciate their help and support.

Finally, thanks from the bottom of my heart for everything you give me, my family. My parents are my power- they gave life to me and constant love. I want to thank my sisters MƠ, VUI who grew up with me and always love and take care of me, and two my brothers-in-law HIẾN for their great encouragement. Thanks to my little lovers my niece and nephews: GIA NINH, GIA HƯNG, HÙNG LONG and PHÚC LONG for their love they give me.

There are not enough words to express my gratefulness to them.

Villetaneuse, July 06, 2016

Nguyễn Thị Hằng Nga

Table of content

Acknowledgements i
Table of content iii
Abbreviation captions vii
General introduction 1
Chapter 1 Bibliography 4
1.1. Alumina 4
1.1.1. Introduction 4
1.1.2. Phase transformation of alumina 4
1.1.3. Structure crystalline of alumina phases 6
1.1.3.1. Alumina γ and η 6
1.1.3.2. Alumina δ 6
1.1.3.3. Alumina θ 7
1.1.3.4. Alumina θ', θ" and λ 7
1.1.3.5. Alumina χ 8
1.1.3.6. Alumina κ and κ' 8
1.1.3.7. Alumina α 8
1.1.4. Transformation mechanism of alumina 9
1.1.4.1. Reorganization of crystalline structure 9
1.1.4.2. Nucleation growth type 10
1.1.5. Influence of different factors on transformation of alumina 11
1.1.5.1. Temperature 11
1.1.5.2. The addition of ion metal 11
1.2. The transformation of alumina with present of silica 11
1.2.1. Mechanism 11
1.2.2. Trimethylethoxysilane (TMES) 12
1.2.3. Tetraethoxysilane (TEOS) 12
1.3. Synthesis 13
1.3.1. Sol gel processes 13
1.3.2. Mercury mediated method 16
1.3.3. Flame aerosol method 17

1.3.4. Vapor-Liquid-Solid process 19
1.3.5. Electrospinning 20
1.4. Alumina monolith 23
1.4.1. Fibrous alumina 23
1.4.2. Nanofibrous alumina monoliths 24
1.4.2.1. Synthesis and properties 24
1.4.2.2. Electronic band structure 26
1.5. Mullite 27
1.5.1. The crystal structure of mullite 27
1.5.2. Properties of mullite 28
1.5.2.1. Mechanical property 28
1.5.2.2. Electronic property 29
1.5.2.3. Optical property 30
1.6. Applications of ultraporous alumina 31
1.6.1. Removal of arsenic 31
1.6.2. Photocatalytic media 32
1.7. Conclusion 34
Chapter 2 Characterization methods 35
2.1. X-ray diffraction 35
2.2. Electron microscopy 37
2.2.1. Scanning electron microcopy 37
2.2.2. Transmission electron microscopy 38
2.3. Brunauer-Emmett-Teller method 39
2.4. Inductively Coupled Plasma/ Optical Emission Spectrometry 41
2.5. Thermogravimetric analysis 42
2.6. UV-visible luminescence spectra 43
Chapter 3 Elaboration of nanofibrous alumina 46
3.1. Metallic precursors 46
3.1.1. Materials 46
3.1.2. Purity measurements of aluminum precursors 46
3.2. Synthesis of ultra-porous alumina (UPA) 49
3.2.1. Materials and conditions 49
3.2.1.1. Materials 49
3.2.1.2. Conditions 49

3.2.2. Process 51
3.2.2.1. Depassivation 51
3.2.2.2. Amalgamation 51
3.2.3. The growth speed 54
3.2.4. Impurities of alumina monoliths 57
3.2.5. The micro-structure of aluminas 60
3.3. Structural, chemical and phase transformations of alumina 61
3.3.1. Effect of annealing on structure composition 62
3.3.2. Chemical and structural transformations 63
3.3.3. Intermediate metastable phases and structural and chemical state 68
3.4. Conclusion 69
Chapter 4 Silica modified alumina 71
4.1. Synthesis 71
4.1.1. Chemical treatment 71
4.1.2. Thermal treatment 72
4.2. Structural, chemical and phase modification of UPA treated TMES 73
4.2.1. Effect of annealing on the structure composite 73
4.2.2. Effect of annealing on chemical and structural transformations 75
4.2.3. Intermediate metastable phases and structural and chemical state 79
4.3. Structural, chemical and phase modification of UPA treated TEOS 80
4.3.1. Effect of treated silica and annealing temperature on the structural 80
4.3.2. Effect of annealing on chemical and structural transformations 83
4.3.3. Mullite 86
4.4. Optical properties 89
4.4.1. TMES treated alumina 89
4.4.2. TEOS treated alumina 91
4.4.3. Effect of quantity SiO_2 on the optical property 96
4.5. Conclusion 97
Chapter 5 Model of morphological modifications 99
5.1. The 3D model of UPA monoliths 99
5.1.1. Mass density 100
5.1.2. Porosity and specific surface area 101
5.2. Morphological modifications 102
5.2.1. Pure UPA 102

5.2.1.1. Annealing below 100 °C 102
5.2.1.2. Annealing below 870 °C 102
5.2.1.3. Annealing above 870 °C 105
5.2.2. TMES treated UPA 108
5.2.2.1. Annealing temperatures below 100 °C 108
5.2.2.2. Annealing below 870 °C 108
5.2.2.3. Annealing above 870 °C 109
5.2.3. TEOS treated UPA 109
5.2.3.1. Annealing temperatures below 100 °C 109
5.2.3.2. Annealing below 870 °C 110
5.2.3.3. Annealing above 870 °C 111
5.2.4. Comparison between UPA impregnated with TMES and TEOS 111
5.3. Conclusion 113
Chapter 6 Ultra porous alumina for application in microwave planar antennas 115
6.1. Motivation 115
6.1.1. Protocol 116
6.1.2. Hydrophobic treatment 119
6.2. THz measurement 119
6.3. Results and discussion 121
6.3.1. Refractive index and dielectric loss 121
6.3.2. Factors affecting 122
6.3.2.1. Effect of mass density 122
6.3.2.2. Effect of silica treatment 123
6.3.2.3. Effect of fabrication method 124
6.3.2.4. Effect of hydrophobic treatment 124
6.3.3. THz transmission 125
6.3.4. Comparison with reference materials 126
6.4. Conclusion 127
General conclusions and perspectives 128
Scientific productions 131
References 132
Annex 1 142

Abbreviation captions

Al-HP: High purity aluminum

Al-Mono HP: High purity mono-crystalline aluminum

Al-Tech: Technical aluminum

BET: Brunauer-Emmett-Teller

CCD: Charge-coupled device

CVD: Chemical Vapor Deposition

DC: Direct current

ICP/OES: Inductively Coupled Plasma/ Optical Emission Spectrometry

fcc: face-centered cubic

FTIR: Fourier transforms infrared spectroscopy

FWHM: Full width at half maximum

hcp: hexagonal-close-packed

HF: High frequency

MAF: Metoxy-{3-[(2,2,3,3,4,4,5,5,6,6,7,7,8,8,8-pentadecafluorooctyl)-oxy]-propyl}-silane

hkl: Miller index

NMR: Nuclear magnetic resonance

NP: Nano particulate

PEO: Poly ethylene oxide

PL: Photoluminescence

PLE: Photoluminescence excitation

PVA: Polyvinyl alcohol

PVP: Polyvinyl pyrrolidone

SEM: Scanning electron microcopy

SR: Synchrotron-radiation

TEM: Transmission electron microscopy

TEOS: Tetraethoxysilane

TGA: Thermogravimetric analysis

TMA: Trimethylaluminum

TMES: Trimethylethoxysilane

UPA: Ultra-porous nanofibrous alumina

VLS: Vapour-Liquid-Solid

W: Tungsten

General introduction

The nanofibrous ultraporous alumina (UPA) was extensively studied last two decades after a new method for its fabrication has been proposed [Vignes 1997, Beauvy 2004]. The UPA growth kinetics is mainly controlled by such factors as environmental humidity and temperature [Vignes 1997, Beauvy 2004]. The raw UPA monoliths have an amorphous structure and containing from 40 to 43 wt.% of water at room temperature, an extreme low mass density 0.025 g/cm^3, high porosity >99 % and specific surface about 300 m^2/g [Costanzo 2001, Vignes 2008]. The microstructure includes tangled hydrated alumina fibers with a diameter of about 5 nm and the monoliths are very fragile and easy are destroyed in contact with turbulent air or liquids [Vignes 2008]. The mechanical stability of UPA can be improved by applying the thermal treatment. Furthermore, the treatment by high temperature leads to the transformation phase of alumina from the anhydrous alumina which is an amorphous structure with γ phase appeared at 870 °C, θ at 1100 °C and a stable α phase at temperatures above 1200 °C. The characteristic diameter of the alumina fibrils and specific area of these crystalline polymorphs are respectively: 7 nm and 150 m^2/g (γ), 10 nm and 100 m^2/g (θ) and 250 nm and 10 m^2/g (α) [Vignes 2008]. The UPA mass density strongly increases up to 3 g/cm^3 with an increase of the thermal treatment temperature. In order to increase the mechanical rigidity, chemical vapor treatment of the raw UPA with silica precursors was also applied [Costanzo 2001]. The silica-treated UPA extends stability of γ and θ polymorphs respectively until 1200 °C and 1400 °C. The electronic structure of UPA undergoes significant modifications during the thermal treatment and a blue shift of the fundamental absorption onset has been reported from 6.85 eV in γ-Al_2O_3, 7.60 eV in θ-Al_2O_3 to 9.36 eV in α-Al_2O_3 [Museur 2013]. Along with these properties, UPA shows a large field of applicability in the environmental process, e.g. as adsorbent of metal ions in aqueous solutions and supporting matrix for photocatalyst nanoparticles [Tchieda 2016, Bouslama 2011, Bouslama 2012].

The results of several researches have been given the fundamental knowledge about the characteristics of alumina and the method for fabrication. However, there is a lack of a detailed model description for the chemical, structural and morphological modifications of the ultraporous nanofibrous alumina. In this PhD work, we continue investigation of structural properties of UPA and propose a model for their prediction. The model provides physical parameters related to the UPA transformations, which are evaluated. We showed an extension of the silica treated UPA towards formation of mullite phase. Furthermore, our first measurements of refraction and absorption of UPA for GHz-THz frequency range show their suitability for the fabrication of optics.

The manuscript of this PhD work is organized in sixes chapters as explained below.

Chapter 1: introduces general information about alumina and its phase transformations. We summarize the synthesis methods of alumina nanofibers and its chemical and thermal transformation process. The synthesis and electronic properties of ultraporous nanofibrous alumina monoliths are presented. Applications of the ultraporous nanofibrous alumina for absorption of metal ions in water and photocatalysis are described.

Chapter 2: presents the principle methods used for the characterizations of alumina: X-ray diffraction, Electron microscopy, Brunauer-Emmett-Teller technique, Inductively Coupled Plasma / Optical Emission Spectrometry, Thermogravimetric analysis and UV-visible luminescence spectroscopy.

Chapter 3: describes the experimental installation for the elaboration of ultraporous nanofibrous alumina monoliths. An analysis is presented of principal impurities in metallic aluminum precursor and their influence on the growth kinetics. The experimental data on the structural (fiber size, mass density), compositional (water content) and crystalline phase transformation of ultraporous nanofibrous alumina during thermal treatment are summarized.

Chapter 4: describes the modifications of ultraporous nanofibrous alumina chemically modified by the impregnation of silica precursors: trimethylethoxysilane (TMES) and tetraethoxysilane (TEOS). The fibril size, specific surface area and mass density of the silica treated alumina are analysed. Farther, the process of thermal treatment of these materials at temperatures above 1400 °C leading to mullite formation is studied by XRD and photoluminescence spectroscopy methods.

Chapter 5: in this chapter the 3D model of nanofibrils ultraporous alumina monolith is proposed, which distinguishes two principal domains of temperature modifications: surface diffusional mass transport over a single fibre and material sintering. The crossover between these two domains' kinetics takes place at moderate temperatures close to the crystallization onset at 870 °C. This model is applied to the experimental data achieved in Chapters 3 and 4 to obtain and compare the characteristic process activation energies.

Chapter 6: reports on the fabrication of samples for investigation of THz frequency measurements of different forms of the nanofibrous ultraporous alumina, which show their perspective for use in microwave planar antennas.

Finally, in **Conclusion** I summarize all result obtained in this PhD work and suggest perspectives for future studies.

Chapter 1
Bibliography

The general knowledge about alumina structure and phase transformation has been reported in many articles. In this chapter, we summarize main structural and morphological data of alumina. Furthermore, mullite and its mechanical, electrical and optical properties are explained. In addition, methods for alumina fabrication are described with accent on those for synthesis of nanofibrous ultraporous alumina monoliths. Results of investigations of electronic properties and applications of porous alumina are presented.

1.1. Alumina

1.1.1. Introduction

Alumina is also called aluminum oxide or aloxide, aloxite, or alundum depending on the crystalline structure. Alumina has been widely used in industries as ceramic materials, catalysis, filters, etc. thanks to its electrical insulating and high thermal conductivity properties. In common, mineral alumina consists of three kinds of species where each one depends on the number of hydrate groups (n) with the general formula Al_2O_3, nH_2O [Wefers 1987]:

- Hydroxides aluminum (Al_2O_3, $3H_2O$ or $Al(OH)_3$ with n=3) Gibbsite, bayerite and norstrandite.

- Oxide hydroxides aluminum (Al_2O_3, H_2O or AlOOH with n=1) boehmite and diaspora.

- Hydroxides dehydrated (Al_2O_3,$1/5H_2O$ or $5Al_2O_3$, H_2O with n=0.2) tohdite.

1.1.2. Phase transformation of alumina

The thermal decomposition of aluminum hydroxides or oxyhydroxides results in appearance of transition aluminas and terminates by the most stable phase – α phase alumina. This transition alumina includes a variety of polymorphs, such as χ, κ, γ, δ, η, θ and α phase. The structure of the transition alumina depends on the arrangement of oxygen atoms and a distribution of aluminum ions on sublattice in tetrahedral and octahedral interstitial sites [Lejus 1964, Wefers 1987]. In α-Al_2O_3, the oxygen in sublattice is hexagonal-close-packed (hcp) structured with 2/3 of octahedral sites occupied with cations, while γ, δ, η, θ have a face-centered cubic (fcc) arrangement of oxygen atoms and cations present in various proportions in both octahedral and tetrahedral sites [Levin 1998, Boumaza 2009]. Fig. 1.1

below depicts the structural evolution of alumina, which evidences effects of the transition temperature and alumina precursor.

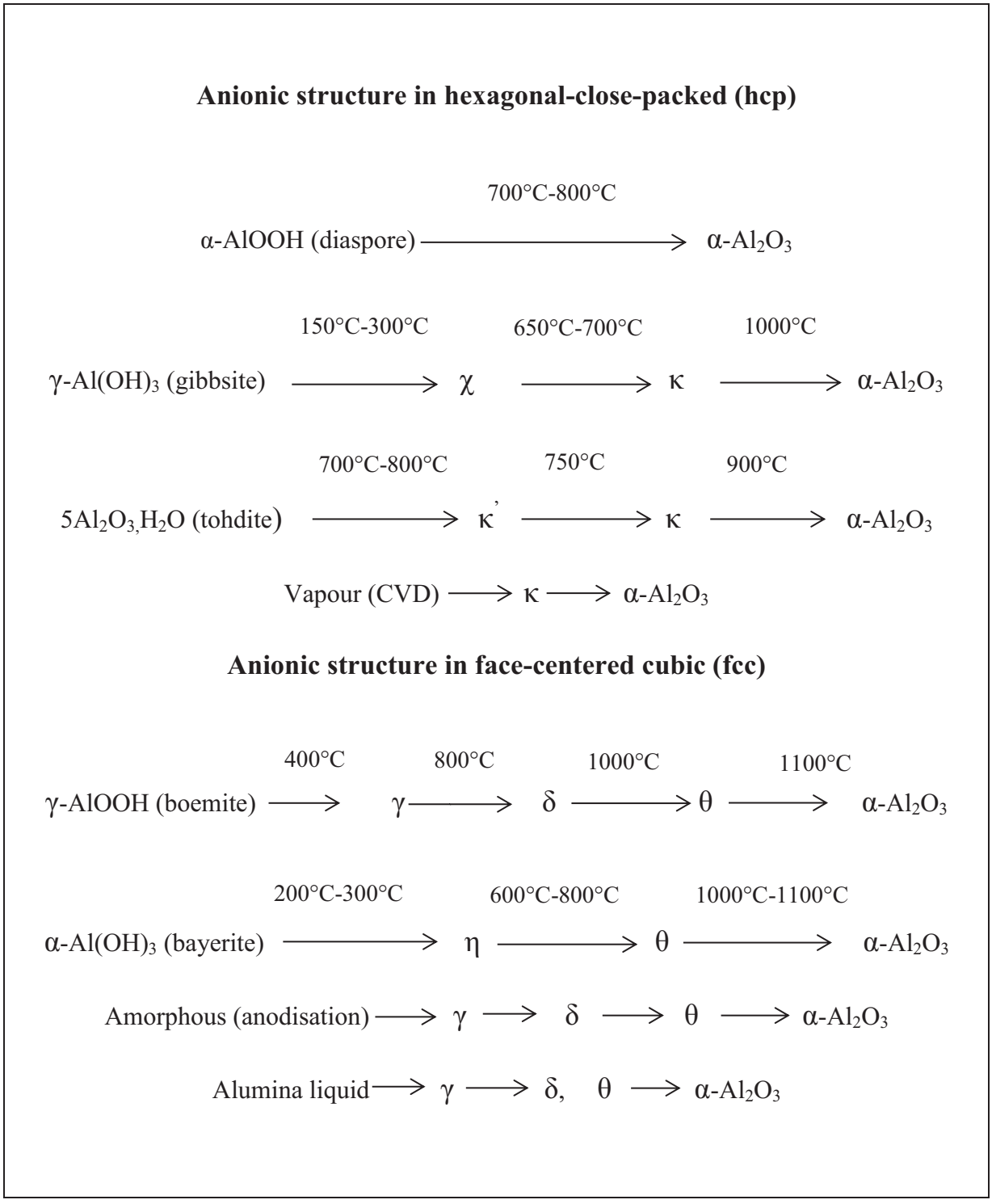

Figure 1.1: The diagram of the transition alumina [Wefers 1987].

1.1.3. Structure crystalline of alumina phases

1.1.3.1. Alumina γ and η

The γ and η alumina have a spinel structure with space group Fd3m, Z=8 [Lippens 1964, Zhou 1991, Wang 1999]. In the normal spinel AB_2O_4, the unit cell was made by 32 oxygen anions and 24 cations. However, only $21\frac{1}{3}$ Al^{3+}ions are available for the cation positions in η-alumina and in the isomorphic γ-alumina with Al cations are distributed in 16d and 8a sites [Zhou 1991, Hahn 1995, Levin 1998, Cai 2002, Cai 2003] therefore, the spinel-type lattice of η and γ-alumina contains cation vacancies [Zhou 1991].

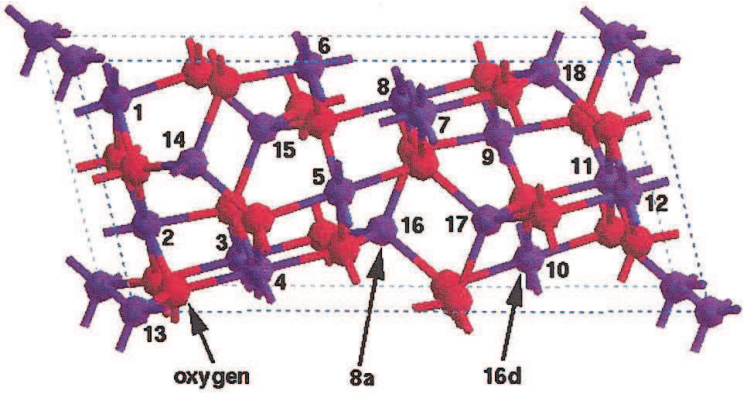

Figure 1.2: Vacancy free cell of γ alumina [Cai 2002].

Lippens and De Boer [Lippens 1964] have shown that the *c/a* ratio of η-alumina is between 0.985 and 0.993 and the *c/a* ratio of γ-alumina is varying between 0.983 and 0.987 by method selected-area electron diffraction. In the indicated that, γ-alumina is more tetragonal and the oxygen sublattice is fairly well ordered much more than that of η-alumina. The strong anisotropy of the shrinkage in *a* and *b* axes of boehmite is the cause of the more pronounced tetragonal character of γ-alumina [Lippens 1964].

1.1.3.2. Alumina δ

The δ-alumina phase is the transition one between γ and θ phases. δ-Al_2O_3 has been described as a super-lattice of the spinel structure with ordered cation vacancies. The δ supercell has been confirmed to be a tripled unit cell of spinel with 160 ions per unit cell. Three kinds of δ alumina are:

- Tetragonal: $a_\delta = b_\delta = a_\gamma$ and $c_\delta = 3a\gamma$ with space group P41 [Zhou 1991, Hahn 1995].

- Orthorhombic: $a_\delta = a_\gamma$, $b_\delta = 1.5a_\gamma$ and $c_\delta = 2a_\gamma$with space group $P2_12_12_1$ [Jayaram 1989, Bonevich 1993].

- δ-Al_2O_3: $a_\delta = a_\gamma\sqrt{2}/2$ and $c_\delta = 3a_\gamma$ with space group P4m2 [Jayaram 1989, Repelin 1990].

1.1.3.3. Alumina θ

The θ-alumina possesses a monoclinic symmetry with the space group C2/m. There are 20 ions units per unit cell with all of the ions located at 4i Wyckoff positions [Yamaguchi 1964, Zhou 1991]. The aluminum cations occupy four octahedral and four tetrahedral interstitials of the oxygen sublattice [Cai 2002, Cai 2003]. The parameter of θ-alumina are $a = 1.5a_\gamma$, $b = a_\gamma\sqrt{2}/4$ and $c = a_\gamma\sqrt{2}/2$ [Levin 1998].

1.1.3.4. Alumina θ', θ" and λ

Besides these most common alumina polymorphs, three types of other alumina were found, which structures are: θ', θ", and λ-Al_2O_3 [Levin 1997, Levin 1998]. Therein, λ-Al_2O_3 was detected when observed reproducibly in both plasma-sprayed Al_2O_3 and thermally oxidized aluminum. Alumina θ' has been found occasionally in annealed anodic Al_2O_3 films, and θ"-Al_2O_3 has been identified reproducibly in plasma-sprayed Al_2O_3. The parameter of each phase was presented in Table 1.1 [Levin 1997, Levin 1998].

Table 1.1: Metastable Al_2O_3 structures based on fcc packing of oxygen anions [Levin 1997]

Phase	Lattice parameter	Space group	Cations/unit cell
θ'-Al_2O_3	$a \approx a_\gamma\sqrt{(\frac{3}{2})}$ $b = a_\gamma/\sqrt{2}$ $c = a_\gamma\sqrt{3}/2$	C2/m	16
θ"-Al_2O_3	$a \approx 1.5a_\gamma$ $b = a_\gamma/\sqrt{2}$ $c = a_\gamma/\sqrt{2}$	A12/n1	64
λ-Al_2O_3	$a \approx 3\sqrt{2}a_\gamma/2$ $b \approx 2a_\gamma$ $c = 1.5a_\gamma$	$P2_1/c$	64

1.1.3.5. Alumina χ

The χ-alumina has three different types of form:

- The cubic crystalline structure with parameter *a* = 0.795 nm [Stumpf 1950].

- Hexagonal: *a* = 0.557 nm, *c* =1.334 nm with space group P6/mm or P63mcm [Zura 1978] or *a* = 0.557 nm and *c* = 0864 nm.

In the hexagonal crystal, the structure will be layers with the anionic of sublatice being identical ABBA sequences like that the structure of gibbsite [Giese Jr 1976]. Aluminum ions occupy octahedral sites present between the oxygen ion layers.

1.1.3.6. Alumina κ and κ'

The κ-alumina has orthorhomic structure with space group $Pna2_1$, Z=8. The lattice parameter are *a* = 0.48437 nm, *b* = 0.8330 nm and *c* = 0.89547 nm [Liu 1991, Ollivier 1997]. It consists of the stacking of pseudo-close-packed layers of oxygen atoms (ABAC type) in between which aluminum atoms are inserted in octahedral and tetrahedral coordination (in the ratio 3:1) [Ollivier 1997].

The κ'-Al_2O_3structure was observed by X-ray diffraction, the crystal structure is similar with tohdite. The tohdite has a hexagonal crystal structure and closed-packed oxygen ion layers with an ABAC... stacking sequence. The aluminum ions occupy both octahedral and tetrahedral positions [Krischner 1966, Okumiya 1971]. Thus, κ'-$A1_2O_3$ was described as a partly cationic redistributed structure of tohdite and as an unstable intermediate phase in the transformation from tohdite to κ-$A1_2O_3$ [Liu 1991].

1.1.3.7. Alumina α

The α-Al_2O_3 (corundum) has a rhombohedral structure with space group R-3c and has 10 atoms in the unit cell [Kronberg 1957, Bilde-Sørensen 1996, Levin 1998]. The structure of α-Al_2O_3 can be considered as a hexagonal close packed sublattice of oxygen anions, with 2/3 of the octahedral interstices filled with aluminum cations in an ordered array [Levin 1998].

The hexagonal parameters for α-Al_2O_3 are *c* = 1.297 nm and *a* = 0.475 nm, with *c/a* = 2.7374 [Badkar 1976, Bourdillon 1984] and corresponds to six oxygen layers along the c-axis of the unit cell. The oxygen anions in α-Al_2O_3 occupy 18*c* and aluminum cations occupy 12c Wyckoff positions [Bourdillon 1984, Waseda 1995].

1.1.4. Transformation mechanism of alumina

Several literature data since 70's have evidenced that the phase transformation of alumina occurred not directly from gamma to alpha phase. The transformation leading to the crystalline structure reorganization takes place in a sequence from γ to δ and/or θ phase (or both together) and finally to α phase under the thermal treatment [Badkar 1976, Morrisser 1985, Cai 2002, Cava 2007, Boumaza 2009]. The nucleation-growth mechanisms of these crystalline phases have been studied in many works [Dynys 1982, Yang 1988, Nordahl 1998, Wen 2002, Palmero 2011].

1.1.4.2. Reorganization of crystalline structure

Boumaza et al. [Boumaza 2009] and Shu Hui-Cai et al. [Cai 2002, Cai 2003] have investigated the phase transformation of alumina at the thermal treatment starting from boehmite and, more precisely, in the processing sequence $\gamma \rightarrow \delta \rightarrow \theta \rightarrow \alpha$. They found that the transition $\gamma \rightarrow \delta \rightarrow \theta$ is accompanied by a migration of cations from octahedral to tetrahedral sites, while maintaining a face-centered cubic symmetry of the sub oxygen network.

The $\gamma \rightarrow \theta$ transformations can be described as a reorganization of the cationic network while interatomic distances of the anion network remain substantially unchanged. And the phase transition from $\theta \rightarrow \alpha$ is accompanied by a restructuring of the subnet of oxygen [Badkar 1976]. S. Cava et al. [Cava 2007] have shown by using X-ray diffraction and transmission electron microscopy that the transition from γ to α phase in alumina powders proceeds in three steps.

- During the first step and at temperatures between 800 and 950 °C, only one phase is presented: γ-phase with the cubic symmetry and a particle size of about 10 nm.

- In the second step and at temperatures between 950 and 1050 °C, there is coexistence of two phases in competition: (γ + α) Al_2O_3 with an average grain size of the order of 55 nm.

- Finally and above 1050 °C the material is completely converted into α-alumina. Grain size observed in the latter stage is greater than 60 nm (Fig. 1.3).

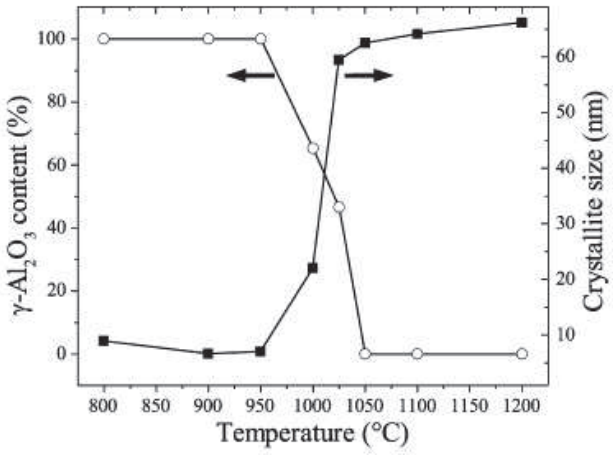

Figure 1.3: Relationship between γ-Al_2O_3 to α-Al_2O_3 phase transition and crystallite size calculated from XRD diffraction patterns [Cava 2003].

1.1.4.3. Nucleation growth type

The phase transformation of θ to α-Al_2O_3 is reconstructive: it results in a disruption of the anionic structure, which transforms from a cubic face-centered lattice becoming hcp [Palmero 2011]. This transformation is nucleation-growth-type [Dynys 1982, Yang 1988, Nordahl 1998, Wen 2002]. In these references, models describing this mechanism have been proposed.

Hui-Ling Wen et al [Wen 2002] have reported that one θ-Al_2O_3 crystallite forms one α-Al_2O_3 crystallite from the critical size of θ-Al_2O_3 crystallite about 20 nm. The nuclei grow up to a size of 45-55 nm by coalescence of nuclei of the original crystallite size. The agglomerates or α-Al_2O_3 poly-crystals with size from 10 nm to >200 nm are formed depending on the temperature treatment. The coalescence between the grains of θ-Al_2O_3 trigs the growth of α alumina [Chang 2001].

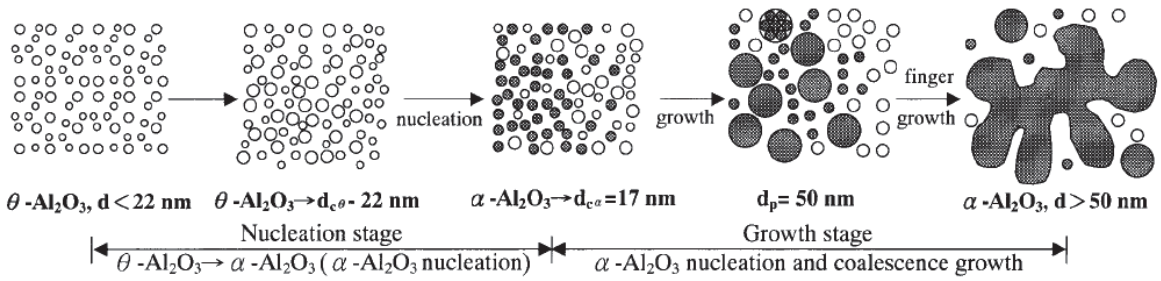

Figure 1.4: Schematic depiction of the growth phenomena of α-Al_2O_3 and α-Al_2O_3 crystallites as θ to α-Al_2O_3 phase transformation [Chang 2001].

1.1.5. Influence of different factors on transformation of alumina

1.1.5.2. Temperature

The temperature is the dominant factor responsible for the phase transformation process. The key influence of temperature on phase transformations of pure and silica modified alumina has been documented [Vignes 1997, Vignes 1998, Costanzo 2004].

The structural properties and phase composition of alumina are largely related to its surface area. In case of many nanostructured materials possessing a high specific area (of high interest for applications e.g. in catalysis) the phase transformations do not occur at low temperatures and suitable additives have to be found in order to conserve the specific surface after the thermal treatment at elevated temperatures. In the case of the material sintering, the phase transformation $\gamma \rightarrow \alpha$, accompanies the consolidation solid process, which avoids formation of high residual porosity, however total removal of porosity remains a difficult task.

1.1.5.3.The addition of ion metal

The addition of metal ions leads to a different behavior of the phase transformations. For example, Fe^{3+} [McArdle 1993, Ozawa 1996], Cr^{3+} [McArdle 1993, Ozawa 1998] Cu^{2+} and Mn^{2+} [Xue 1992, Okada 2000], decrease the temperature of the $\gamma \rightarrow \alpha$ transformation. The addition of the following ions were also studied: Ca^{2+}, Sr^{2+}, Ba^{2+} [Okada 2000], Cr^{6+} [McArdle 1993], Zr^{4+} [Pijolat 1987, Djuricic 1997], Li^{+}, Na^{+}, Ag^{+}, K^{+}, Rb^{+}, Cs^{+} [Yasumori 2000]. The proposed mechanisms are varied. For instance, in the case of Zr^{4+}, zirconia ZrO_2 formation on the surface of γ and θ alumina grains prevents the grains of these two phases to grow to a critical size nucleation enabling them to transform into α alumina. Other ions such as Co^{2+}, Ni^{2+} and Mg^{2+} [Ozawa 1996, Okada 2000] have no appreciable effect on the transition temperature.

1.2. The transformation of alumina with present of silica

1.2.1. Mechanism

The addition of silica to alumina can cause the acceleration or inhibition of the transformation of alumina γ phase to α phase. This process depends on the host material structure [Saito 1998]. For example, the addition of silica to crystalline alumina generally causes a decrease of the transition temperature; in contrast, the addition of silica to amorphous alumina leads to an increase of the temperature.

In fact, the crystalline silica grains manifest themselves as α alumina nucleation sites on the surface of γ alumina, which decreases the activation energy and increases the rate of phase transformation γ → α. In the amorphous phase, the added silica envelopes the alumina grains preventing them from coalescing to reach the critical size necessary for the new phase nucleation. The amorphous silica thus proves to be an exemplary dopant stabilizing the transition alumina with a high specific surface area to temperatures exceeding 1200 °C [Mizushima 1993, Horiuchi 1999].

1.2.2. Trimethylethoxysilane (TMES)

T. di Costanzo et al. [Costanzo 2001] have investigated the effect of doping with amorphous silica of ultraporous monolithic alumina using the trimethylethoxysilane (TMES) silica precursor. They found that silica inhibits the transformation θ → α and proposed three explanations:

- The low bulk density monoliths means that the alumina grains θ can hardly coalesce to achieve critical mass germination of α alumina, as the number of contact points between the alumina crystallites θ per unit volume is lower than in the case of a commercial γ alumina.

- The second explanation supposed the presence of an amorphous layer of silica over the entire surface of the alumina grains. This layer will decrease ion diffusion and growth of alumina crystallites, hence the need to operate at higher temperatures to reach the phase transition.

- Finally, the proposal assumed that the silica precursor used changes the chemical composition of the alumina grains and the Si^{4+} ions would be distributed among the tetrahedral gaps in the spinel structure of γ alumina. They inhibit the diffusion of ions and thus the germination of the α alumina.

1.2.3. Tetraethoxysilane (TEOS)

Several other studies have been devoted to the introduction of silica from tetraethoxysilane (TEOS, $Si(OCH_2CH_3)_4$), which hydrolyses on the γ alumina, in liquid form [Beguin 1991, Horiuchi 1999] or as a vapor (CVD: Chemical Vapor Deposition) [Katada 1995].

In both cases of the deposition methods, TEOS precursor reacts at room temperature with the hydroxyls groups of the alumina surface and decomposes at 500 °C according to the reactions:

$$\text{-Al -OH} + Si(OC_2H_5)_4 \rightarrow \text{Al -O- } Si(OC_2H_5)_3 + C_2H_5OH \quad (1.1)$$

$$\text{-Al -O- } Si(OC_2H_5)_3 \rightarrow \text{-Al -O- } Si(OH)_3 + 6CO_2 \quad (1.2)$$

Going towards higher temperatures the groups $-Si(OH)_3$ is dehydrated to form Si-O-Si or Si-O-Al on the surface of the alumina grains. In the case of γ alumina, the amount of silica necessary to achieve optimal stabilization seems to depend on the deposition method.

For the deposition through the liquid TEOS hydrolysis, it has been found that the stabilization increases with the amount of silica dopant and reaches a plateau with the addition of more than 3 wt.% [Beguin 1991]. This amount corresponds to the half surface hydroxyls groups reacted.

In the case of the vapour deposition method, the phase stabilization increases mainly with the quantity of introduced silica up to about 15 wt.% and then decreases when exceeding amounts greater than 20 wt.% [Katada 1995].

1.3. Synthesis

Various methods have been developed in order to synthesize Al_2O_3 nanofibers, such as sol-gel [Teoh 2007, Wang 2007, Ma 2009], template [Jin 2003, Zuo 2006], chemical vapor deposition in flame [Guo 2009], and mercury mediated technique [Pinnel 1972, Yang 2009]. These methods are presented below.

1.3.1. Sol gel processes

The sol gel process is a common method for alumina fibers fabrication staring with different precursors: boehmite, metallic Al, alkoxides or aluminum osproposide [Noordin 2010]. The first step in the nanofibrous alumina synthesis is the precursor hydrolysis.

The boehmite formed has the formula $AlOOH.nH_2O$ and the initial spherical particles of boehmite are sol solution with a low viscosity. In the reaction process, network structures and fibers are formed and the sol transformed into gel with a high viscosity. In the same time, the solid in the gel has initially spherical nanoparticles that are transformed into the crystalline boehmite. The solid was heated at higher temperature dehydrates and dehydroxy later forming the different transition alumina phases in stages at progressively higher temperature than 400 °C. Finally is the α-alumina phase, it appears at 1000 °C or higher temperature. These reactions may be represented as follows [Teoh 2007, Wang 2007, Ma 2009]:

$$Al(OH)_3.\ nH_2O \rightarrow \text{amorphous } Al(OH)_4\text{-} + H_2O\text{+} + (n - 1)\ H_2O \quad (1.3)$$

$$Al(OH)_4\ \text{-}\leftrightarrow \gamma\text{-}AlOOH.nH_2O + (1- n)\ H_2O \quad (1.4)$$

$$\gamma\text{-}AlOOH{\cdot}nH_2O \rightarrow \gamma\text{-}Al_2O_3 + 2(1- n)\ H_2O \quad (1.5)$$

$$\gamma\text{-}Al_2O_3 \rightarrow \alpha\text{-}\ Al_2O_3 \quad (1.6)$$

In case of metallic Al nanoparticles are used as a precursor, the reactions are [Park 2004, Teoh 2007, Chandradass 2008]:

$$2\ Al + 4\ H_2O \rightarrow 2\ AlO(OH) + 3\ H_2 \text{ without stirring} \quad (1.7)$$

$$2\ Al + 6\ H_2O \rightarrow 2\ Al(OH)_3 + 3\ H_2 \text{ with stirring} \quad (1.8)$$

The reaction (1.7) produced boehmite while the reaction (1.8) formed trihydroxide, bayerite and continued to dehydrate resulting in boehmite:

$$Al(OH)_3 \rightarrow AlO(OH) + 2\ H_2O \quad (1.9)$$

The tranfformation $AlO(OH) \rightarrow \gamma\text{-}Al_2O_3$ has occurred during the dehydration process. In both cases, the bohemite is a precursor for $\gamma\text{-}Al_2O_3$ and further dehydration at temperatures up to 700 °C appears without a significant change in the morphology, which is preserved at this stage of hydrolysis. The result also assumed that the morphology of final Al_2O_3 is dominated by structural properties of the hydrolytic precipitates, of which the phase and morphology have a strong nature of interrelation, induced by a spontaneous nucleation and a growth processes during a hydrolysis. A conclusion that a phase control of bohemite AlO(OH) is important to produce the desired Al_2O_3 nanofibers [Teoh 2007, Noordin 2010].

With alkoxides $Al(OR)_3$, as the starting materials, the initial hydrolysis with a water yield alcohol and the hydroxylated aluminum centers as follows [Teoh 2007]:

$$Al(OR)_3 + H_2O \rightarrow Al(OR)_2(OH) + ROH \quad (1.10)$$

$$Al(OR)_2\ OH) + H_2O \rightarrow AlO(OH) + 2\ ROH \quad (1.11)$$

$$Al\text{ -}OH + Al\text{ -}OX\text{-}\ Al \rightarrow Al\text{ -}O\text{-}\ Al + XOH\ (X{=}H \text{ or } R) \quad (1.12)$$

$$2\ AlO(OH) \rightarrow Al_2O_3 + H_2O \quad (1.13)$$

In the first period of the sol gel reaction, three small dimensional oligomers are formed with the group -Al-OH on an outer surface in reactions (1.10, 1.11). Linkage of -Al-OH

groups occurs via polycondensation and results in oxypolymer. When sufficient interconnected Al-O-Al bonds are formed, they respond cooperatively to form colloidal particles or a sol. These sol particles aggregate and increase in size with increasing time 1 h, 3 h or 4 h forming three dimensional network and randomly distributed spherical nanoparticles as shown by TEM. After 24 h the synthesis for all samples completed the hydrolysis of the precursors and the nano-sheets are shown to curl up forming the nanofibers [Zhu 2002, Teoh 2007, Wang 2007].

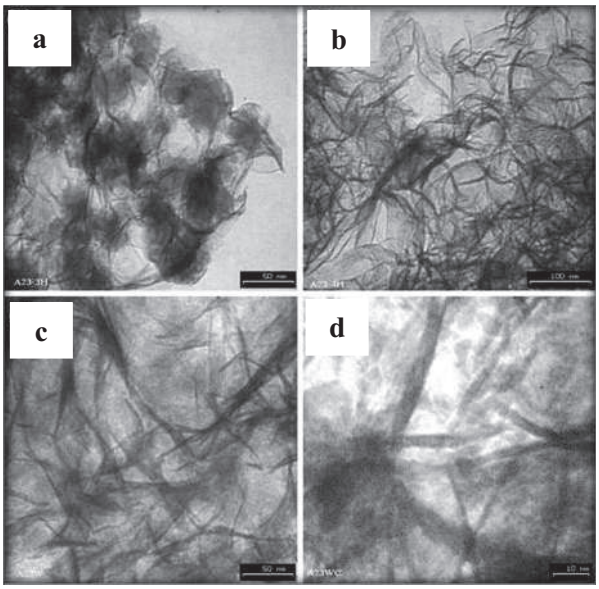

Figure 1.5: TEM micrographs of nanoscale alumina particles hydrolyzed for 3 h (a); 4 h (b); 24 h (c); and TEM micrograph at high magnification of the sample calcined at 540 °C after hydrolysis for 24 h (d) [Schubert 2000].

In the sol-gel process using aluminum iospropoxide as an original material [Okada 2000], the reaction had to be carried out at the range of the water to aluminum iospropoxide (H_2O/Al) molar ratio Rw = 60-65, at the different range fibrous material was not formed. Besides the condition of molar ratio, the sol gel reaction was affected by a pH of reacted environment [Lee 2003]. In this case under the acidic condition, the hydrolysis was enhanced, and the rate of polycondensation and aggregation to larger particles were increased too high for nanofibers formation. Additionally, the presence of organic solvent influences significantly on the reaction rate. The solvent is catalysis in the reaction mixture, especially at the beginning of the reaction [Schubert 2000, Teoh 2007]. With the presence of this

homogenizing agent, the hydrolysis is facilitated. In this work, the solvent isopropanol is suitable in the hydrolysis mixture leads to nanofibers formation [Teoh 2007].

1.3.2. Mercury mediated method

Other process for the nanofibrous alumina synthesis is a mercury mediated method. The nanofibers alumina were produced in high purity aluminum strips with a purity of 99.5 % and 99.99 % immersed in the $HgCl_2$ solution in 5 minutes at a room temperature and then aluminum strips were removed and exposed in the air. After some times, the white alumina powder was formed on the surface of aluminum strips [Pinnel 1972, Yang 2009].

During the process, following reactions took place [Pinnel 1972]:

$$2\ Al + 3\ HgCl_2 \rightarrow 3\ Hg + 2\ AlCl_3 \tag{1.15}$$

$$4\ Al + 3\ O_2 + 2n\ H_2O = 2\ Al_2O_3 \cdot nH_2O \tag{1.16}$$

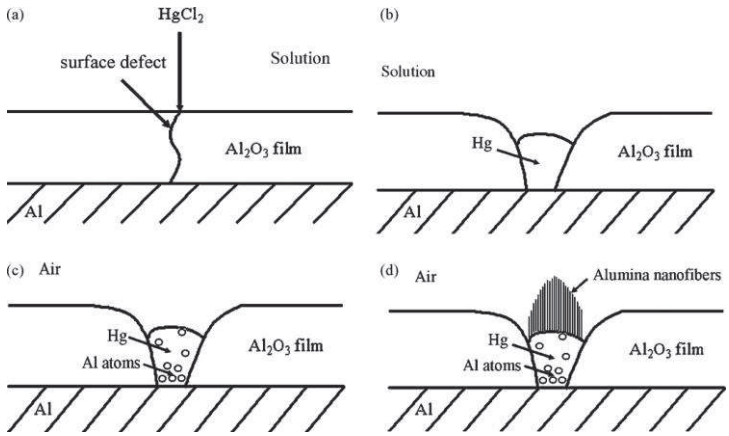

Figure 1.6: Schematic representation of the formation process of alumina nanofibers. (a) The penetration of $HgCl_2$ solution, (b) the formation of Hg, (c) the diffusion of Al atoms, and (d) the formation of alumina nanofibers [Yang 2009].

The Al reacted with a mercuric chloride forming Al amalgam and oxidized in air when removed from the solution. The dissolution of the Al into the Hg was a continuous process. The final product is the alumina nanofibres with diameters of 5-15 nm and length of several micro-meters. After heated at 850 °C for 2 h the alumina converted to γ-alumina [Yang 2009].

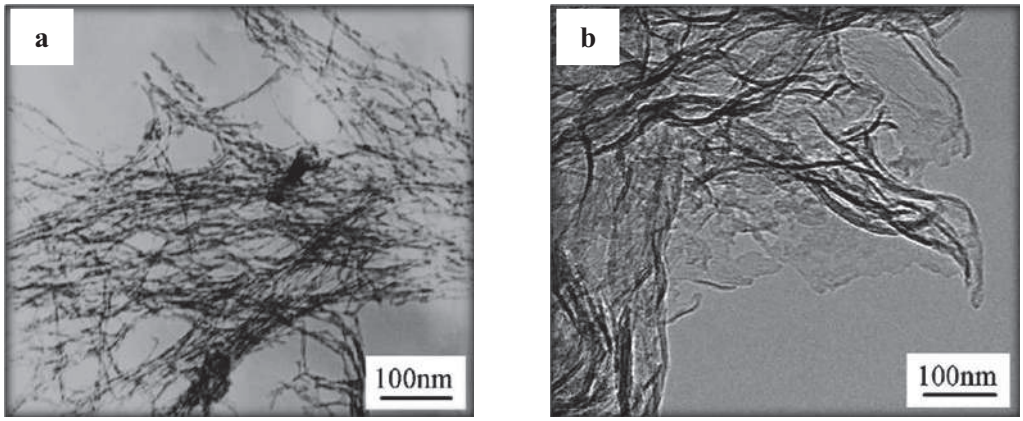

Figure 1.7: TEM images (a) of as-grown products and (b) γ-Al_2O_3 nanofibers [Yang 2009].

The alumina nanofibers were formed with the specific surface area about 164.9 m^2/g and 205.2 m^2/g. Both smaller diameter and larger specific surface area of the alumina nanofibers can be reached when the purity of Al increases.

1.3.3. Flame aerosol method

Flame aerosol technology is used for large-scale manufacture of ceramic commodities such as pigmentary titania, fumed silica and alumina [Peng 2002, Teoh 2007].

In this method using trimethylaluminum (TMA, chemical formula C_3H_9Al, 97 %) is a precursor. The fuel gas contained and bubbled through the TMA liquid at 25 °C. The fuel gas carrying the TMA vapor, then flowed through the burner and combusted in a coflow laminar diffusion flame under the pressure at approximately 0.015 atm. The TMA vapor reacted in the flame to form an alumina aerosol. Above the flame, a sampling tube was positioned about 200 mm above the burner, where a temperature was approximately 400 °C. The post-flame alumina aerosol was drawn into the sampling tube by a vacuum and alumina particles were captured on a filter. Both the TMA container and the burner were operated at an atmospheric pressure. The process of this method was shown in the Fig. 1.8.

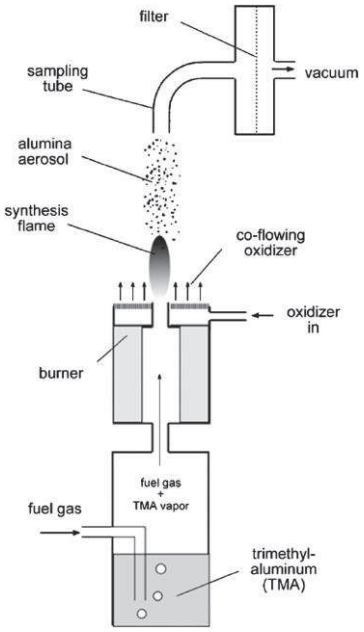

Figure 1.8: Schematic of the flame synthesis apparatus [Peng 2000].

Depending on these flame conditions: a flame temperature, molar $H_2/CO_2/O_2$ ratios or a location of nanofiber formation within a flame, the alumina nanofiber obtained differently shown in Fig. 1.9.

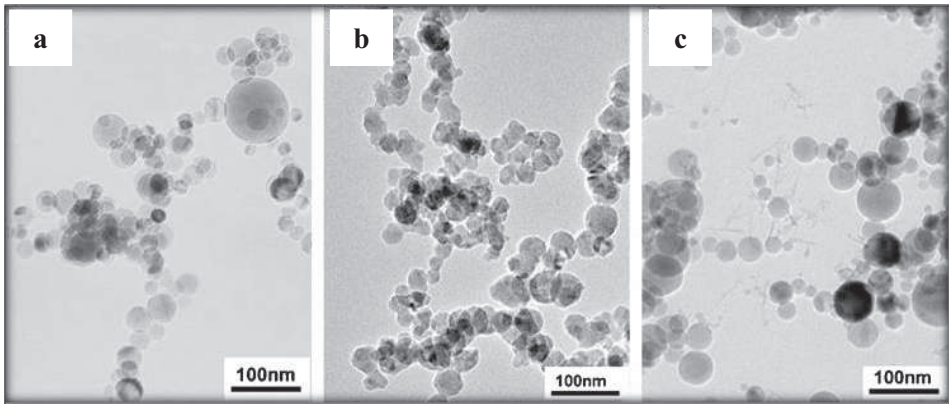

Figure 1.9: TEM images of (a) alumina nano spheres from a H_2/O_2 flame; (b) aggregated alumina nanoparticles from a H_2/air flame; and (c) alumina nano spheres and nanofibers from a $H_2/CO_2/O_2$ flame [Peng 2002].

The alumina nanofibers formed were non-crystalline, typically 2-10 nm in diameter and 20-210 nm in length. These fibers were mixed with spherical nanoparticles along with carbon nanotubes formed at the same time. In the air or in pure H_2 flames, no alumina nanofiber

formation was found. The alumina nanofibers were formed from gas-phase aluminum containing species in the flame such as CO or hydrocarbon. In other case the nanofibers were formed in the region past the maximum temperature zone of the flame. With sufficiently high temperature may be due to the higher concentration of aluminum in the gas phase, while the presence carbon nanotubes or nanofibers may serve as templates or mediating agent for the alumina nanofibers formation [Schubert 2000, Peng 2002].

1.3.4. Vapor-Liquid-Solid process

Crystalline alumina nanowires or nanorods were synthesized vapor-liquid-solid (VLS) process in high temperature with using Fe, SiO_2 or Co as catalyst [Wanger 1964, Tang 2001, Peng 2002].

J. Zhou et al [Zhou 2002] has been succeed in the nanotrees fabrication from the process involved mixing commercially an aluminum powder, an iron powder and a silicon carbide powder in an appropriate ratio and then sprinkled on tungsten (W) boat. The boat was then placed at the center of the vacuum bell jar and evacuated down to about $5.0 \cdot 10^{-2}$ Torr. The boat was gradually heated up by passing current through it, and kept at 1700 °C for 1 h under flowing argon. The treated powders contained in the W boat were taken out and cooled down to room temperature in flowing argon [Reneker 1996].

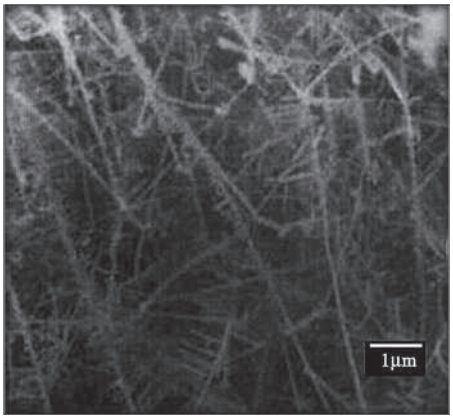

Figure 1.10: The SEM image of the alumina nanotrees [Peng 2002].

The typical nanowires achieved with diameter crystalline of size around 50 nm and the in length about 2 μm. And the tree trunks of the nanotrees are around 100 nm in diameter and around 10 μm in length (Figure 1.10).

Other group [Jin 2003] with using the VLS mechanism for a heating AlB_2 and Co in a quartz boat, which acts as the O source, under a N_2 flow has been produced generated micrometre-size coral-like structures, consisting of the aluminum oxide nano rods (Figure 1.11).

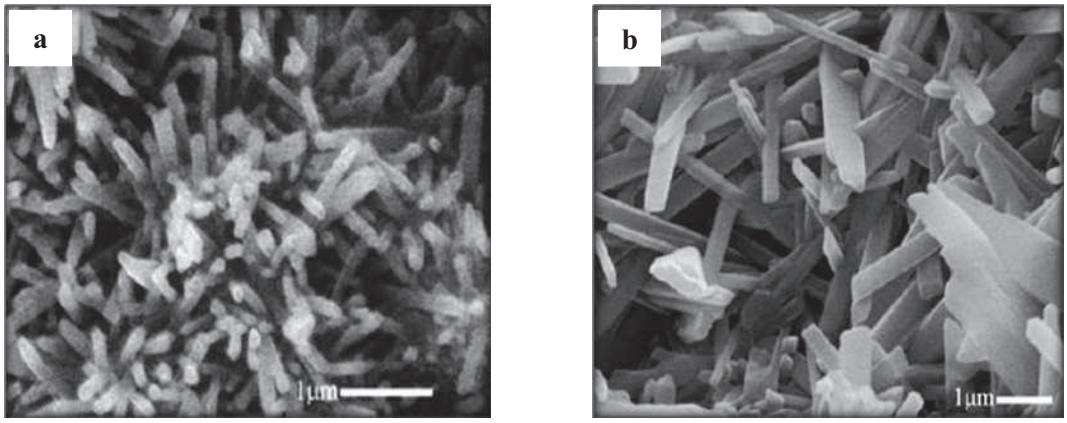

Figure 1.11: SEM images: (a) coral-like structures, prepared at 1050 °C, (b) microrods, generated at 1250 °C [Jin 2003].

Figure 1.11a shows that the product consists primarily of large coral-like structures with numerous tiny branches sprouting from the central cores. The in diameter of branch is about 20-200 nm and up to 4 μm in length. The branches are fairly straight and most exhibitions have a circular cross section however, some have a polyhedral cross section. The branch surfaces are clean and smooth. At higher temperatures 1250 °C, the branch diameters and lengths are significantly increased in Fig. 1.11b with a diameter nanorods 1 μm (some exceed 1.5 μm), and are several microns long. These rods appear to show various morphologies, for example prismatic and hexagonal.

1.3.5. Electrospinning

An electrospinning is a popular technique for the polymer fibers synthetization [Reneker 1996, Dan 2004, Tan 2005] and this process has been investigated for the preparation of alumina nanofibers in recently years. It was reported on many articles [Sawicka 2006, Azad 2006, Panda 2007, Tuttle 2008].

The principal of this process is the imposition of a strong electrostatic field to a capillary connected with a reservoir containing a polymer solution or melt [Formhals 1934, Larrondo 1981]. The effect electrostatic fields on appendant droplet of the polymer solution at the capillary tip make them deform to a conical shape known as Taylor cone. If the voltage

surpasses a threshold value, electrostatic forces overcome a surface tension and a fine charged jet is ejected [Fong 1999, Fong 1999]. The jet moves towards a ground plate, which acts as a counter electrode. The solvent begins to evaporate immediately after the jet is formed. The result is the deposition of nanofibers on a substrate located above the counter electrode. The nanofibers formed could be aligned when an insulated cylinder attached to the axel of a DC motor is used as the substrate [Sundaray 2004, Panda 2007].

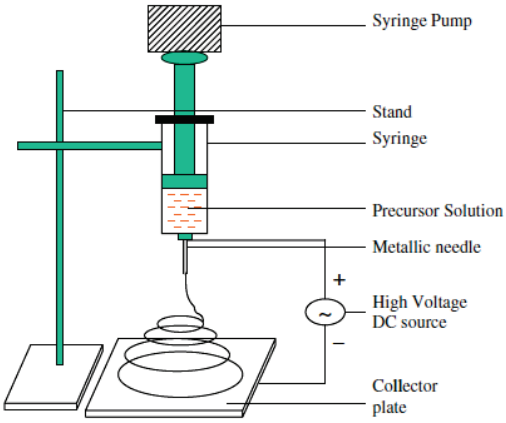

Figure 1.12: Schematic diagram of electrospinning set up [Panda 2007].

P.K. Panda and colleagues [Panda 2007], succeed with alumina nanofibers preparation by an electrospinning technique using the different polymer precursors as a combination of Polyvinyl alcohol (PVA) and Poly ethylene oxide (PEO), aluminum acetate and aluminum nitrate as alumina precursor.

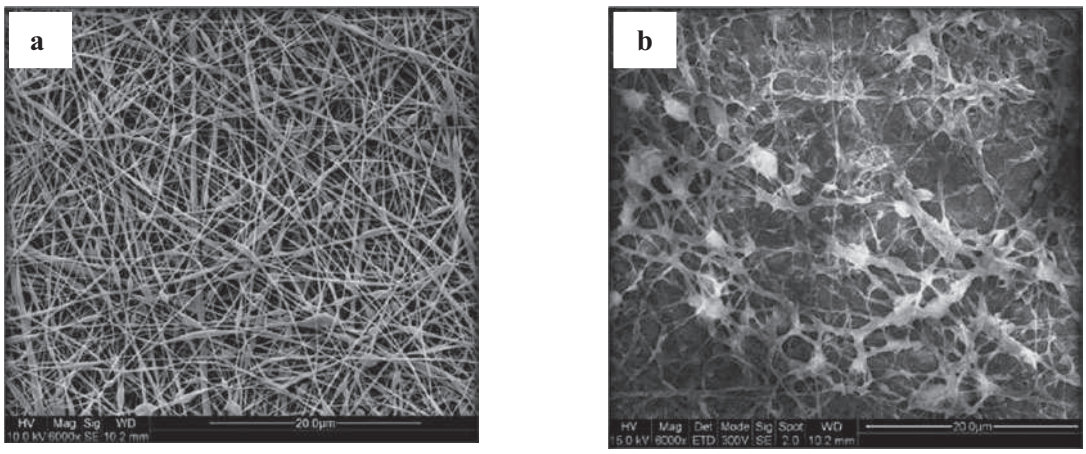

Figure 1.13: (a) SEM picture of PVA/aluminum acetate nanofibers (b) SEM picture of PEO/aluminum nitrate nanofibers [Tan 2005].

In the case of aluminum acetate is a precursor in the electrospinning of both PVA and PEO are possible and smooth (Fig. 1.13). Other case of aluminum nitrate precursor, the nanofibers are highly hygroscopic due to presence of nitrate anions and their collection was extreme difficult due to strong repulsion perhaps due to concentration of similar charges leading to the fibers either to remain in vertical position on the collector or were simply flying making it difficult for their collection. Therefore, the PVA/aluminum acetate solutions were ideal for an electrospinning.

Other polymer used as the Polyvinyl pyrrolidone (PVP), with the PVP/aluminum acetate solution was placed into a pipette and a copper wire was placed into the solution and connected to a power supply which was set to a potential in the range of 25-30 kV in experiment of R.W. Tuttle et al. [Tuttle 2008] has obtained as-spun nanofibers alumina shown in Fig. 1.14.

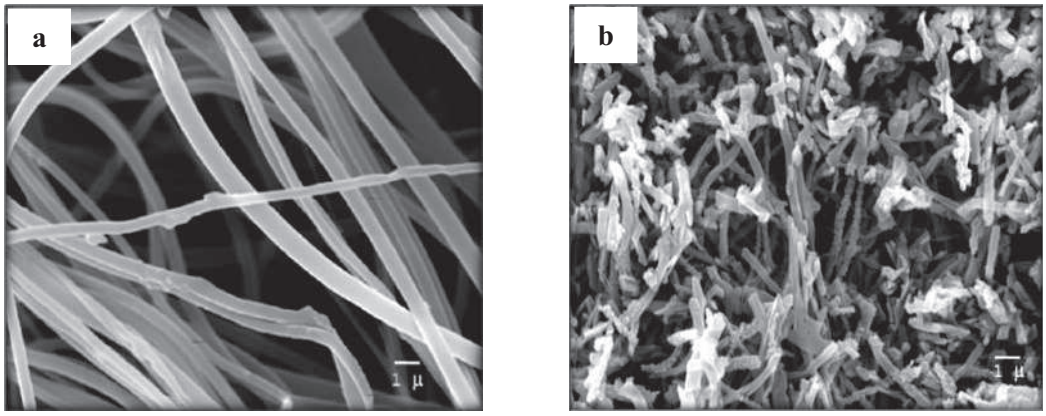

Figure 1.14: SEM images of (a) as-spun aluminum acetate/PVP fibers, and (b) electrospun fibers after 1200 °C annealing [Tuttle 2008*].*

The diameters of these fibers after annealing at 1200 °C (D=1µm) is larger than those prepared by electrospun method. In the same time, the aspect ratio of electrospun fibres was reduced significantly while the material becomes considerably more brittle than the as-spun materials. The decrease of the flexibility of the fibres may result from a high fraction of crystallinity.

1.4. Alumina monolith

1.4.1. Fibrous alumina

The concept of fibrous alumina was defined the first by Wislicenus [Wislicenus 1908, Wislicenus 1926, Wislicenus 1942] from a century ago. Fibrous alumina has been known by growing on the surface of aluminum amalgamated in contact with moist air.

The composition fibrous alumina of Wislicenus was studied in acids solution, birefringence, water content, aging in water. Addition, the structure of fibrous was discovered by the X-ray and electron diffraction which done by John H.L. Watson et al. [Watson 1957]

The samples were prepared by the original material aluminum foil (99.9 %) which was oxidation by sodium hydroxide solution and distilled water and mercury chloride (1 %) solution. The foil freely grows with white fibers of various lengths. Fibrous alumina was observed soon after and was collected 24 hours later (Fig. 1.15).

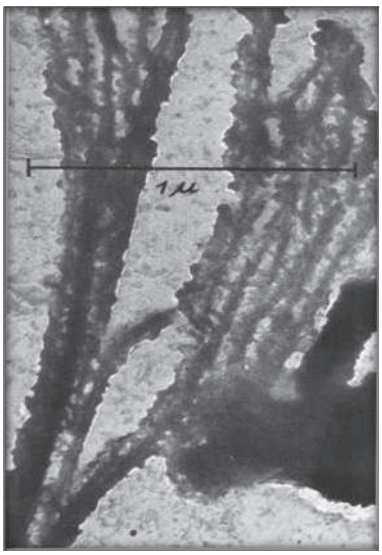

Figure 1.15: Fibrous alumina prepared by slight amalgamation of A1 foils and long fibers grown in moist air [Watson 1957].

The fibrous alumina consisted of an amorphous aluminum hydroxide, adsorbed water and aluminum oxide. The birefringence of the fibers was explained by non-crystalline fibrils of various lengths and about 70-80 nm in diameter. Furthermore, some non-fibrous particles of size smaller than 50 nm were observed.

The binding between particulates in a fibril and between fibrils was very weak. This fact may account for the low density of the material. It has been shown that the formation of fibrous alumina is dependent on the existence of a small amount of water and a small amalgamation on distinct spots on the aluminum surface. The mechanism of the formation of fibrous alumina is suggested as similar to that of anodic films on aluminum [Hart 1953]. It was observed that strongly amalgamated aluminum or aluminum amalgam itself did not produce fibrous alumina even in air, but formed a grey powder of which the main component was mercuric oxide and aluminum [Souza 1958].

1.4.2. Nanofibrous alumina monoliths

1.4.2.1. Synthesis and properties

The new method of elaboration of fibrous alumina monoliths has been developed by J-L. Vignes. The fibrous alumina were grown by oxidation of high purity aluminum though a mercury-sliver liquid in humid atmosphere as shown in Fig. 1.16 [Vignes 1997, Costanzo 2001, Vignes 2008].

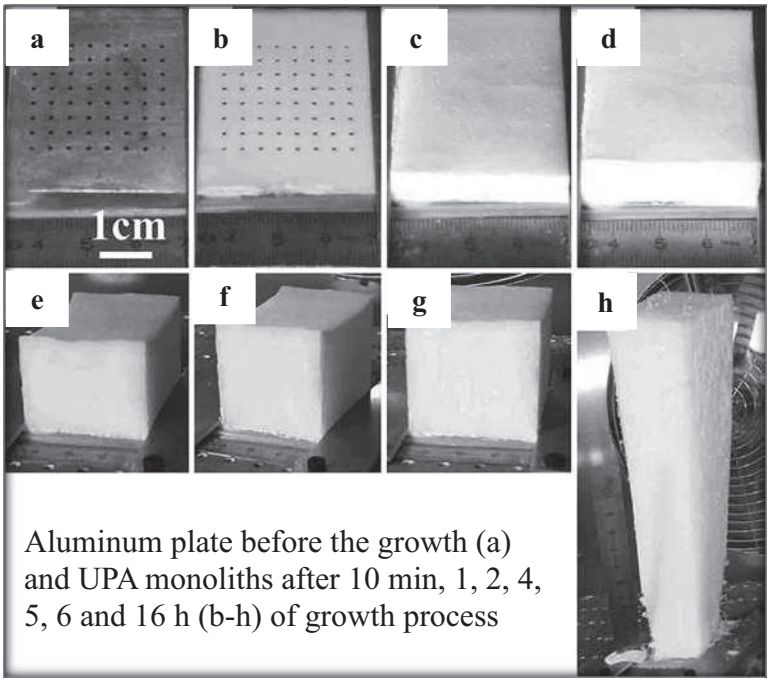

Figure 1.16: Process growth of UPA [Vignes 2008].

The ultra-porous alumina (UPA) monoliths have a mesoporous amorphous structure shown in Fig. 1.17. They have extreme purity and a high porosity (more than 99 %) and contain form 40 to 43 wt.% of water at room temperature. Moreover, UPA has a high surface area (300 m^2/g) after heating at 350 °C and an average size of 10 nm for the mesopores. The microstructure includes tangled hydrated alumina fibres with a diameter of about 5 nm.

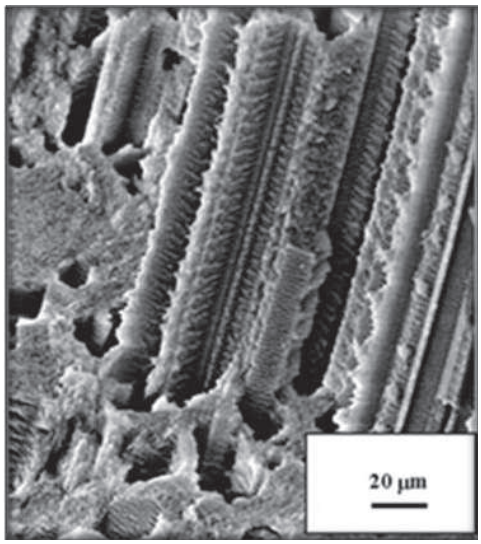

Figure 1.17: Microstructure of UPA [Vignes 2008].

The monoliths are very brittle and easy are dissolved by the permeation in an aqueous solution. Therefore, they need to be stabilized alumina by applying a thermal treatment. This leads to anhydrous alumina, which is amorphous up to the cubic γ-form at 870 °C . At higher temperatures alumina transform to θ and α-alumina (Fig. 1.18).

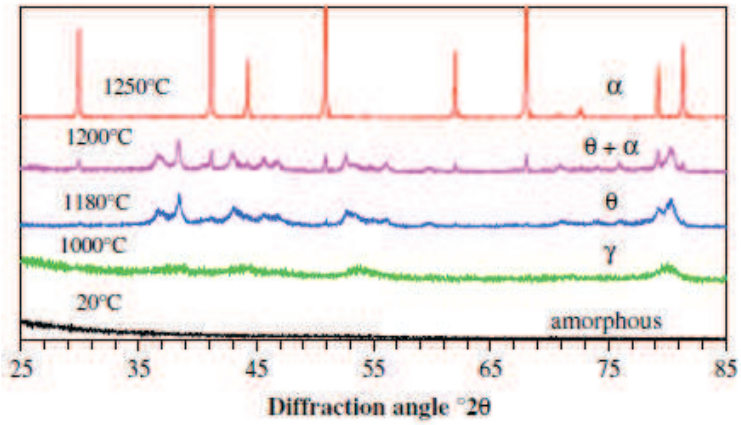

Figure 1.18: X-ray analysis on samples treated at different temperatures during 4 h [Vignes 2008].

1.4.2.2. Electronic band structure

The photoluminescence (PL) properties and optical electronic transitions in α, θ and γ UPA polymorphs were investigated firstly by L. Museur et al. [Museur 2013] with the using time and energy resolved spectroscopy method.

The photoluminescence excitation (PLE) spectra of the prepared UPA(γ), UPA(θ) and UPA(α), samples are shown in Fig. 1.19:

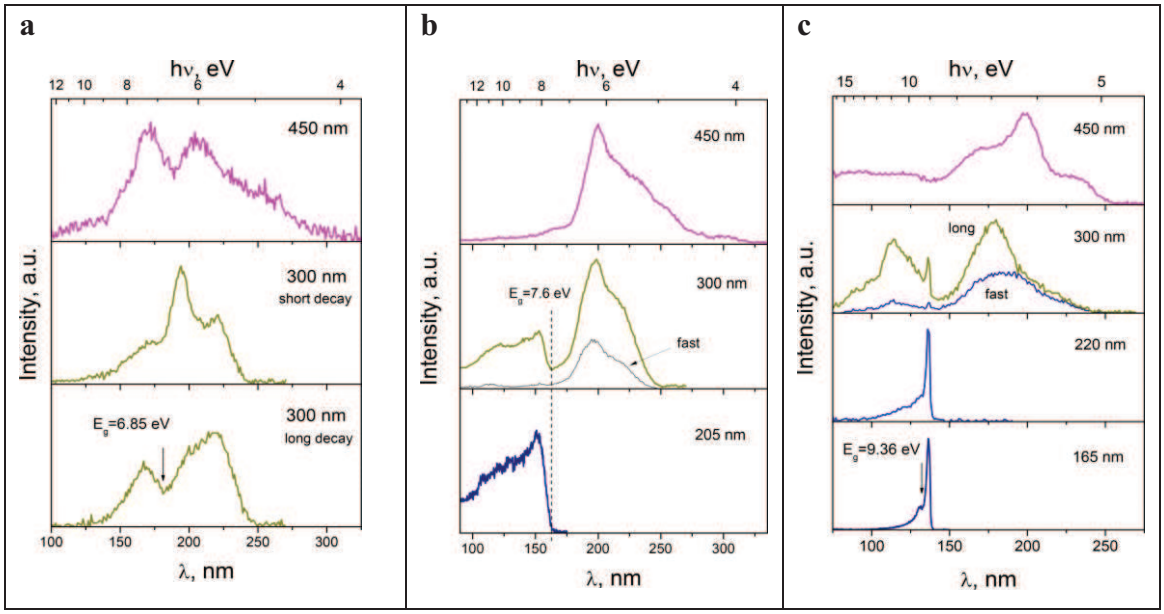

Figure 1.19: PLE spectra of principal PL bands (T = 7 K): (a) γ-alumina (b) θ-alumina (c) α-alumina [Museur 2013].

The PL properties of high-purity transition γ and θ and stable α ultraporous Al_2O_3 at cryogenic temperatures with excitation by synchrotron radiation have been analyzed based on correlations between the band positions and lifetimes. The PL of different self-trapped excitons associated with singlet free exciton excitation was observed. The red shift of the fundamental absorption onset is 9.36 eV with (α) UPA, 7.60 eV with (θ) UPA and 6.85 eV with (γ) UPA. These results are in agreement with predicting the bandgap narrowing in the order of α > θ > γ [Lee 2007]. The analysis of the F^+ band excitation spectra indicates a decrease of the density of structural defects on order γ > θ > α.

1.5. Mullite

1.5.1. The crystal structure of mullite

Mullite is a part of the orthorhombic aluminosilicate system sillimanite-ι-alumina with the general composition $Al_2(Al_{2+2x}Si_{2-2x})O_{10-x}$ [Bowen 1924, Shigeo 1962] . The SiO_2-rich end member of the system is sillimanite with x = 0. The popular stable compounds of mulitte are 3/2- mullite ($3Al_2O_3.2SiO_2$, x = 0.25) and 2/1-mullite ($2Al_2O_3.SiO_2$, x = 0.40) [Klug 1987, Epicier 1990, Aksay 1991]. These structures are formed by the removal of oxygens from the O(3) positions (tetrahedral linking oxygen) and by a readjustment of cations from the T to T* type in partially occupied columns formed by linking (Si, Al)O_4 tetrahedra (Fig. 1.20) [Aksay 1991]. The backbone of the crystal structures of the phases are chains of edge-connected AlO_6-octahedra crosslinked by tetrahedral di- and triclusters. Al and Si are randomly distributed over the tetrahedral diclusters, with most of the triclusters being occupied by Al. The crystal structure of mullite contains oxygen vacancies, with the number x corresponding to the general aluminosilicate formula. The tetrahedral di- and triclusters and the O vacancies of mullite are locally ordered but on the long-range they are strongly but not completely disordered in a modulated way. The structural arrangement of di- and triclusters and of O vacancies is thermally very stable and persists up to the melting point [Epicier 1990, Schneider 2015].

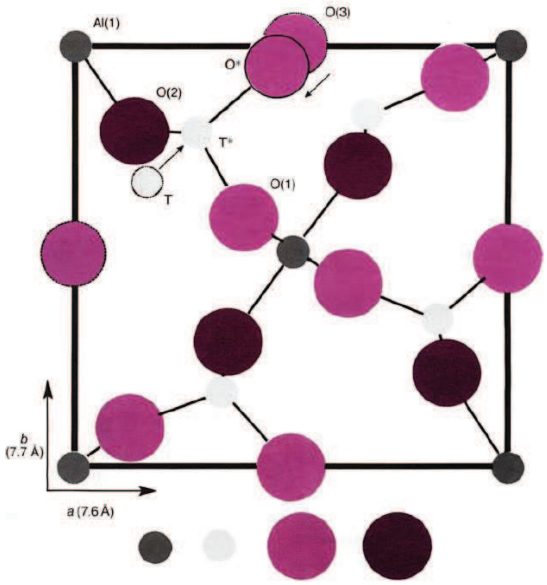

Figure 1.20: Projection of the ideal orthorhombic mullite unit cell along the [001] direction showing the cations transition (indicated by an arrow) associated with the formation of an oxygen vacancy and readjustment of oxygen in the O(3) positions [Aksay 1991].

1.5.2. Properties of mullite

1.5.2.1. Mechanical property

Mullite has never been considered suitable for high-strength applications at low temperatures. The fracture strength σ of polycrystalline mullite ceramics at room temperature depending on the chemical composition and microstructure of the material ranges between about 200 MPa and 400 MPa [Torrecillas 1999, Huang 2000]. Besides, the porosity has a distinct negative influence on the fracture strength [Shigeo 1962].

For a high temperature mullite ceramics with little impurities, a low amount of glass phase, and an equiaxed mullite microstructure shown a significant strength decrease above 1200 °C to 1300 °C, probably due to grain boundary gildings [Shigeo 1962, Mizuno 1991]. The initial increase in strength corresponds to a similar increase in fracture toughness caused by the blunting of the cracks with the viscous. The brittle character of mullite was demonstrated by the fracture toughness κ_{IC}, which is a measure for the ability to withstand plastic deformation, is relatively low (≈2.5 to ≈3.5 MPa.m$^{1/2}$) and does not change significantly up to 1400 °C. Selected data are given in Table 1.2.

Table 1.2: Data of Bending Strength (σ) and Fracture toughness (κ_{IC}) of 3/2-Mullite ceramics at different temperature T

Temperature (°C)	σ (MPa)	κ_{IC} (MPa.m$^{1/2}$)	References
RT		2.5	Huang 2000
1200	260	3.6	Torrecillas 1999
1300	200	3.5	Torrecillas 1999
1400	120	3.3	Torrecillas 1999

Moreover, mullite has been recognized for its excellent creep resistance at a high temperature. The significant differences creep between phase-pure polycrystalline mullite and mullite-matrix composites were observed. The first survey confirmed the high creep resistance of mullite at 1500 °C but not usually and indicated that mullite in a single crystalline form shows no plastic deformation at stress levels up to 900 MPa [Dokko 1977]. Other testing by R.D. Nixon et al, impressive results have been obtained with polycrystalline mullite without an amorphous boundary phase (Fig.1.21) [Nixon 1990].

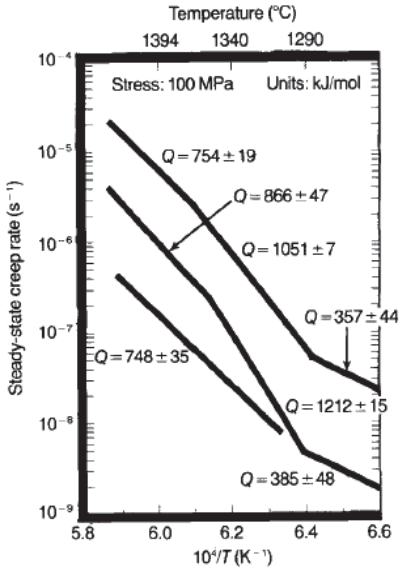

Figure 1.21: Steady-state creep rate of mullite and mullite-matrix composites in the temperature range of 1230 °C to 1430 °C at a constant stress of 100 MPa. Upper curve is for a mullite with glassy inclusions and the lower one is for a phase-pure mullite. Middle curve corresponds to a 20 vol.% silicon carbide whisker-reinforced mullite with the composite of mullite + glass of the upper curve used as the matrix [Nixon 1990].

In the case of mullite matrix composites and/or mullites that contain an amorphous boundary phase, the creep resistance decreases. This decreasing by 2 orders of magnitude when tested under constant stress in the temperature range of 1177 °C to 1427 °C and at stress levels of 5 to 220 MPa. Wherein, a 20 vol.% silicon carbide-whisker reinforced mullite composite also containing an amorphous phase shows similar behavior, but only 1 order of magnitude decrease in the creep resistance. The three different activation energy regimes also appear to be related to the change in the viscosity of the amorphous phase with a temperature [Nixon 1990]. In the middle-temperature regime, cavitation primarily at the grain boundaries appears to be responsible for the high activation- energy creep, whereas in the low- and high-temperature regimes, a cavitation is not observed.

1.5.2.2. Electronic property

Mullite is an electrical isolator at ambient and moderate temperatures, and therefore is suitable as a substrate material for electronic devices. However, in spite of its importance for high-temperature ceramics only few and contradicting experimental results exited on the electrical conductivity of mullite at high temperature [Shigeo 1962]. For instance, mullite and

mullite-based glass-ceramics have now emerged as candidates in high-performance packaging applications. Like that a substrate, mullite has a dielectric constant ε = 6.7 results in about 17 % lower signal transmission delay time than alumina (ε=9.85) [Shigeo 1962, Tummala 1991]. Moreover, mullite has a low-thermal-expansion coefficient (4.10^{-6} /°C in the 20 °C to 200 °C range) which is almost that of silicon. Thence, the mullite response these requirements of high-performance packaging for new-generation computer systems place a premium on the development of ceramic substrates with a low dielectric constant, a high wiring density and low sintering temperatures to achieve sintering with metals such as a copper and a thermal-expansion match to silicon.

1.5.2.3. Optical property

The optical properties of mullite had focused on its applicability as a window material within the mid-infrared portion of the spectrum from 3- to 5-μm wavelength [Musikant 1981, Gentilman 1986]. The infrared characteristics of mullite have been studied extensively since the 1950s [Roy 1953]. However, Prochazka and Kiug [Prochazka 1983] demonstrated successful by of mullite as an infrared transparent window. In Fig. 1.22 shown that the comparison transmissivity of mullite with various other ceramic materials in this mid-infrared range. The results presented two features of mullite: the peak of the 4.3-μm absorption band in the transmittance spectrum of mullite is quite deleterious to the overall properties of the mullite and the 5 μm cutoff of mullite windows is below the cutoff of other window materials. Conclusion that the 4.3 μm absorption appears to be associated with processing related defects and thus may be eliminated but the 5 μm cut-off is intrinsic to the structure of mullite.

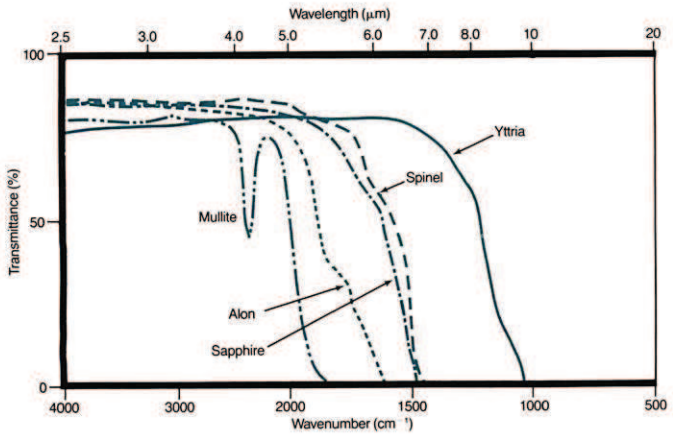

Figure 1.22: In-line transmission spectra for monolithic ceramic materials in the mid-infrared ($4000 \leq \vartheta \leq 400\ cm^{-1}$) [Aksay 1991].

Furthermore, the refractive indices of natural mullites are wide spread with n_α = 1.630-1.670, n_β = 1.636-1.675, and n_γ = 1.640-1.691, and the birefringence and the optical axes angle 2V range between 0.010 and 0.029 and between 45° and 61° [Aksay 1991].

1.6. Applications of ultraporous alumina

1.6.1. Removal of arsenic

The removal of metal ions in water has been investigated last decade. Different methods as oxidation/precipitation, coagulation/co-precipitation, adsorption, ion exchange, and membrane filtration have been applied [Mohan 2007].

Studies of alumina as adsorbent material for arsenic removal from water have been presented by Tchieda et al. [Tchieda 2016]. The adsorbents were characterized for their uptake capacity of As(V) in synthetic drinking water: commercial alumina powder (APS), granular alumina (AGS), synthesized alumina (AMESO) as well as alumina with impregnated TiO_2 nanoparticles heated at 250 and 450 °C (Fig. 1.23). The results have shown that the adsorption of As(V) onto AGS was slow and not very effective, with an adsorption capacity at equilibrium slightly above 1 mg/g. The equilibrium conditions with adsorption capacity <8 mg/g were attained more rapidly with synthesized alumina due to its lowest particle size.

For the maximum adsorption capacity at equilibrium, similar values of about 8 mg/g, were obtained by powder alumina, and TiO_2-coated alumina calcinated at 450 °C, under similar operating conditions. The best kinetic model was found to be the pseudo-second-order for all tested adsorbents, excluding the granular commercial alumina. The result was explained by different granular sizes of the materials, which plays a major role in the adsorption process by affecting transport kinetics inside the adsorbent material.

Addition, the APS removal capacity of As (V) from water by adsorption was influenced strongly by the pH value and the water composition. Therefore, to optimize the removal process, it is recommended to adjust the pH to slightly acidic values among the competitive anions, sulfate ions had moderate adverse effects while the most significant interference occurred in the presence of phosphate and silica solutes.

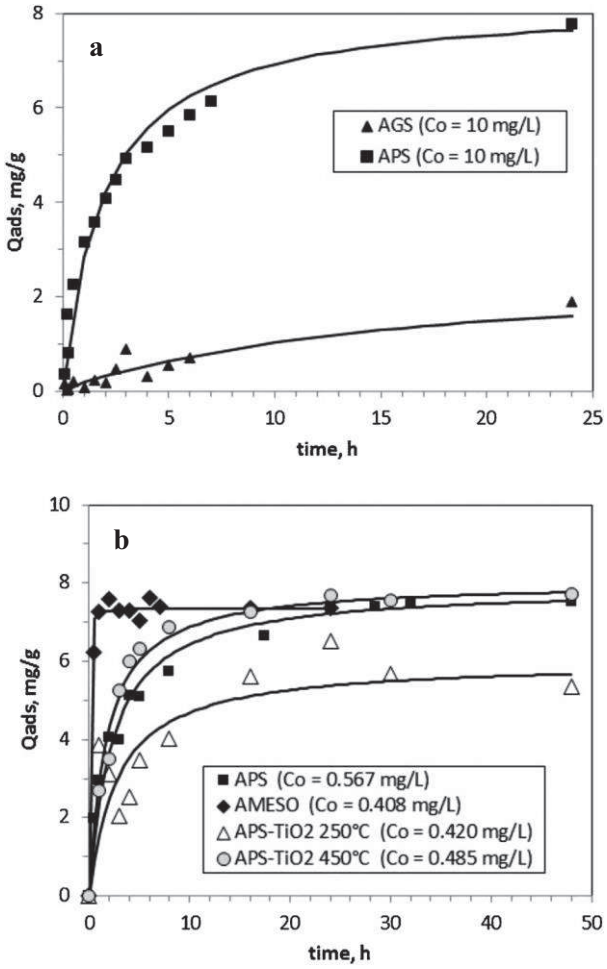

Figure 1.23: Adsorption kinetics of As (V) by the tested adsorbents: (a) C_o (As) =10 mg/L; (b) C_o (As) = 0.4–0.6 mg/L. Solid lines refer tomodeled data [Tchieda 2016].

Based on these results, it was concluded that among different tested adsorbents the synthesized alumina can be considered as most attractive due to its higher uptake capacity and faster adsorption process, low cost and no toxicity.

1.6.2. Photocatalytic media

These properties of monolithic alumina presented: the low density and high porosity, small size of the structural unit and evanescent intrinsic that make interestedly in supporting materials for photocatalyst nanoparticles applications [Bouslama 2011, Bouslama 2012]

The new nanoparticulate (NP) photocatalytic media were prepared by impregnation of size-selected TiO_2 nanoparticles into monolithic ultraporous alumina (UPA) by sol gel method that proposed by M. Bouslama et al. [Bouslama 2011, Bouslama 2012]. The thermal treatment at different temperatures allowed modification of the NP's size and crystalline

composition addition transformation γ, θ and α phase of UPA, covered with silica or not were used. The electronic coupling between titania and UPA support is found to affect the nanoparticle polymorph. In particular, a separation layer of silica increases the TiO_2anatase stability. The best samples were realized with ~30 wt.% of non-agglomerated titania nanoparticles immobilized in the ultraporous alumina structure of γ and θ polymorphs with the specific surface area respectively of 150 and 100 m^2/g. The titania nanoparticles conserve their anatase crystalline structure (most active in photocatalysis) at temperatures as high as 1000 °C, which was explained by the size effect (see Fig. 1.24 below). The rutile phase appears only at T≥1100 °C when particle size increases to ~17 nm due to the slow surface aggregation. The photocatalytic activity (ethylene decomposition) of the non-aggregated nanoparticles is conserved over a wide temperature range, and it decreases as soon as the aggregation takes place. In particularly, the activity of non-aggregated nanoparticles was twice higher compared to those aggregated (quasi-coating); this specific material activity was reported twice higher compared to the Degussa P25 industrial catalyst.

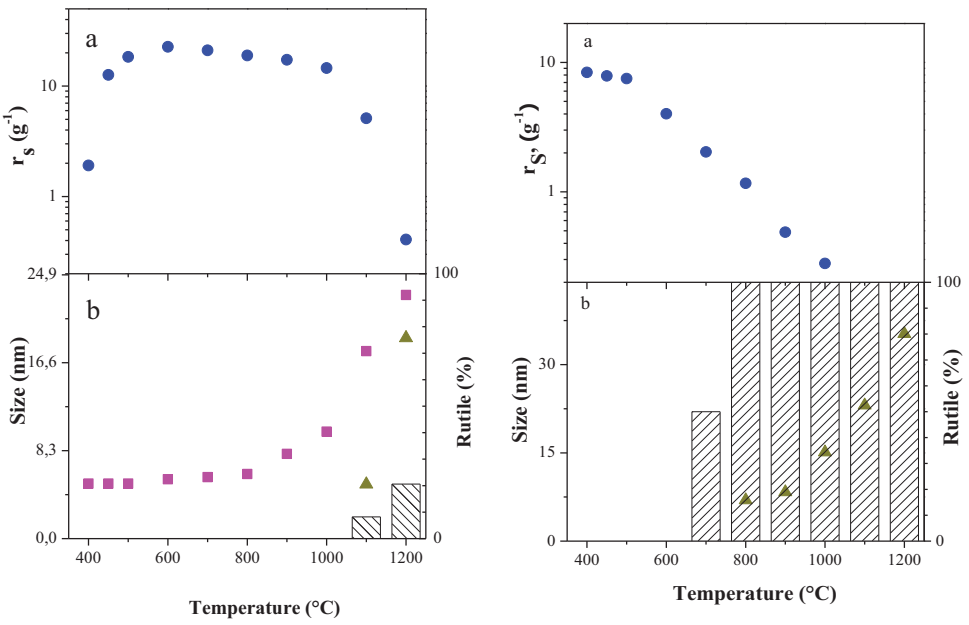

Figure 1.24: Specific reactivity (a) and anatase (■) and rutile (▲) particle size (b) of nanocomposite TiO_2-UPA-SiO_2 photocatalyst versus treatment temperature. TiO_2 nanoparticles are immobilized in UPA of θ (left) and α (right) crystalline phases [Bouslama 2011, Bouslama 2012].

The pure anatase nanoparticles exhibit the higher activity compared to rutile and composite anatase/rutile nanoparticles. Particularly, the photocatalytic activity dramatically decreased as soon as rutile phase is nucleated onto anatase. The activity of the mixed

populations of anatase and rutile nanoparticles depends on the anatase size whereas the activity of the composite nanoparticles containing anatase and rutile polymorphs was influenced by the rutile crystalline size. In pure rutile nanoparticles the activity strongly reduced with size $2R \geq 5$ nm whilst in pure anatase remains constant for sizes $2R \leq 10$ nm. A comparative study show significantly higher photocatalytic efficiency of the prepared materials compared to that of the reference P25 Degussa photocatalyst.

1.7. Conclusion

The alumina is a well-known and extensively studied material in fundamental science. In this Chapter general information about alumina and its phase transformations were introduced. The synthesis methods of alumina nanofiber and its chemical and thermal transformation process are described. The mechanisms and factors affecting the phase transitions between the different alumina polymorphs are investigated. Basic properties and some applications of ultraporous alumina have been discussed.

Recently, new ultraporous nanofibrous monoliths have been successfully synthesized and attracted much attention because of their unique morphology and electronic properties. Their synthesis, structural and electronic properties and morphological transformations were successful studied over the past decade. Several applications of the ultraporous nanofibrous alumina are mentioned.

This material permits an effective chemical modification by ease impregnation of liquids, vapors and even nanoparticles enabling novel functional nanostructured materials with unprecedented properties. Their commercialization is not yet attained and more work has to be done in field of technology of the fabrication process and elucidation and optimization of functional properties.

Chapter 2
Characterization methods

For the investigation characteristics of alumina in this work, we used several verticals techniques. The most useful methods which are X-ray diffraction, Electron microscopy, Brunauer-Emmett-Teller technique, Inductively Coupled Plasma/ Optical Emission Spectrometry, Thermogravimetric analysis and UV-visible luminescence spectra. The principle of these methods have been employed which will be presented in this chapter.

2.1. X-ray diffraction

X-ray diffraction is a useful tool for identifying the atomic and molecular structure of a crystal. A principle of this method is measuring angles and intensities of the diffracted beam and consequently producing a three-dimensional picture of the density of electrons within the crystal [Als-Nielsen 2000]. And then, the positions of the atoms in the crystal can be determined likewise their chemical bonds, their disorder and other information were analyzed from this electron density.

X-rays are electromagnetic radiation with typical photon energies in the range of 100 eV-100 keV. With the x-ray diffraction applications which employs the short wavelength in the range of 1 keV-12 keV. Because of the suitable is probing the structural arrangement of atoms and molecules in a wide range of materials. The energetic X-rays can penetrate deep into the materials and provide information about the bulk structure.

X-ray diffractometers consist of three basic elements: a cathode X-ray tube, a sample holder can be collimated X-ray beam at an angle θ, and an X-ray detector which is mounted on an arm to collect the diffracted X-rays and rotates at an angle of 2θ [Warren 1969, Cullity 1978].

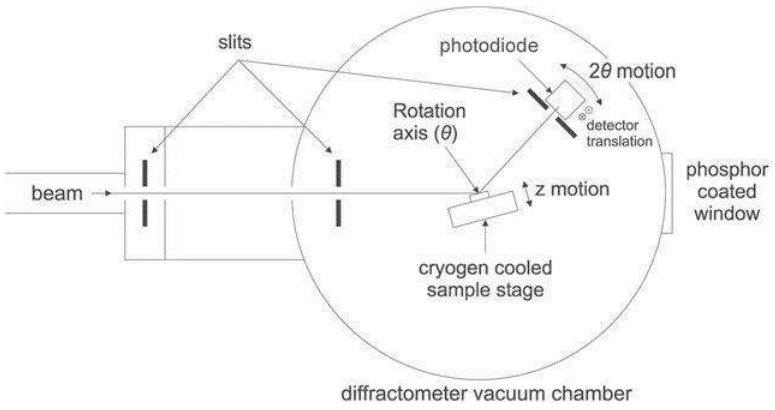

Figure 2.1: Schematic diagram of the diffractometer shown from the side. The X-ray beam enters from the left-hand side and is scattered from the sample in the centre of the chamber.

When electrons have sufficient energy to dislodge inner shell electrons of the target material, characteristic X-ray spectra are produced. These spectra include several components, the most common being K_α and K_β. K_α consists, in part, of $K_{\alpha 1}$ and $K_{\alpha 2}$. $K_{\alpha 1}$ has a slightly shorter wavelength and twice the intensity as $K_{\alpha 2}$. The specific wavelengths are characteristic of the target material such as Cu, Fe, Mo, Cr. Whereas, Copper is the most common target material for single-crystal diffraction, with Cu-K_α radiation = 1.5418 Å. These X-rays are collimated and directed onto the sample. As the sample and detector are rotated, the intensity of the reflected X-rays is recorded. The X-ray signal was converted to the signal to a count rate which is then output to a device such as a printer or a computer monitor, determined by Bragg's law: **$2d\sin\theta = n\lambda$**

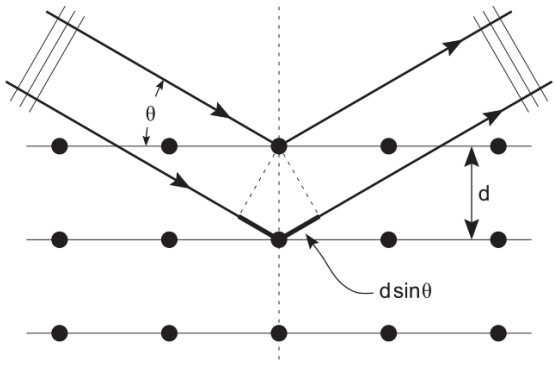

Figure 2.2: Bragg's law.

Here d is the spacing between diffracting planes, θ theta is the incident angle, n is any integer, and λ is the wavelength of the beam. These specific directions appear as spots on the diffraction pattern called reflections. Thus, X-ray diffraction results from an electromagnetic wave impinging on a regular array of a scattering.

After a measurement by INEL XRG 3000, the data obtained which need to match with reference data to find corresponding peaks and a crystal structure by the software. The important result is lattice parameters *hkl* (Miller index) of a crystal.

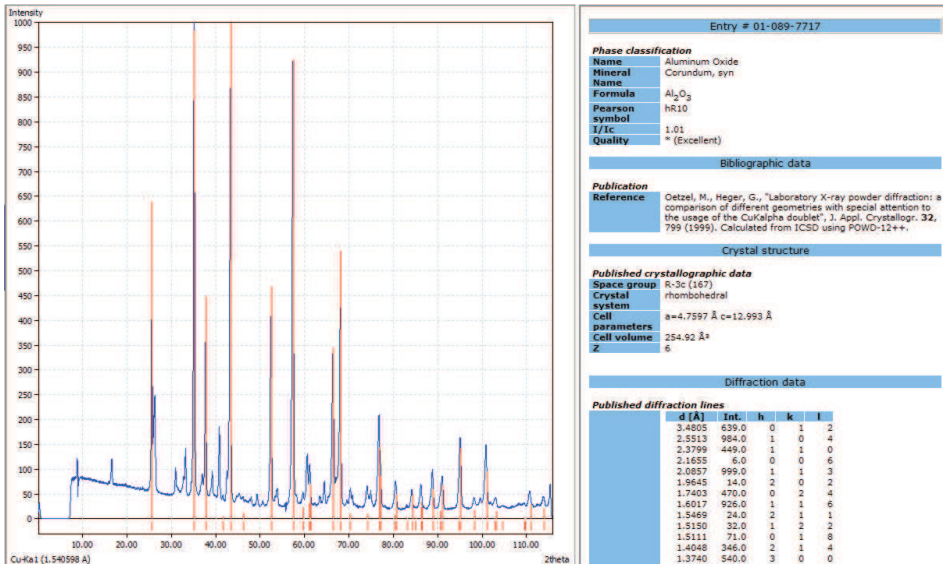

Figure 2.3: Crystal structure of sample was found by Match software.

2.2. Electron microscopy

2.2.1. Scanning electron microcopy

The Scanning electron microcopy (SEM) is one of the most popular techniques for the analysis microstructural morphology of materials.

The sample must be a suitable size to fit in the specimen chamber and are generally mounted rigidly on a specimen stub. However, SEM requires a conductive sample and must be carried out in a vacuum. For non-resistance sample as alumina which need to cover by the Carbon thin layer with some nanometers in a thickness.

The signals result obtained from interactions of the electron beam with atoms at various depths within the sample that contain information about the sample's surface topography and composition. In the most common, the type of signals produced by SEM is secondary electrons emission signals [Nixon 1971]. Due to their low energy, typically an average of around 3-5 keV, it can produces very high-resolution images of a sample surface they can only within a few nanometers of the material surface.

The electrons are detected subsequently by the detector. The electrical signal output by the photomultiplier is displayed as a two dimensional intensities distribution that can be viewed and photographed on an analogue video display or subjected to analog to digital conversion and displayed and saved as a digital image.

A Zeiss Supra 40 VP SEM-FEG was used for all the measurements. The SEM was formed in a high vacuum mode and a low acceleration voltage.

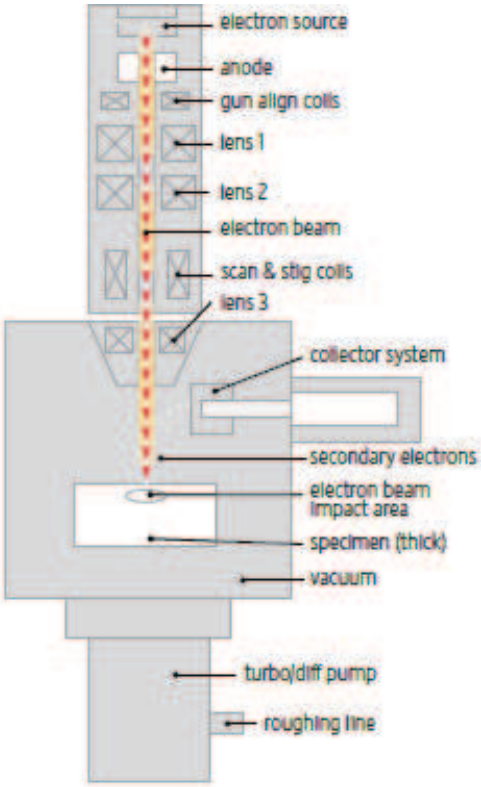

Figure 2.4: The structure of SEM.

2.2.2. Transmission electron microscopy

Transmission electron microscopy (TEM) is a micro technique (similar as a SEM) which the electron beam is transmitted through a very thin sample. The image is constituted by the interaction of electrons transmitted through a specimen. Herein, this image is magnified and focused onto an imaging device, such as a fluorescent screen, on a layer of photographic film, or to be detected by a sensor such as a CCD camera.

The most common mode of operation used into the TEM which is the bright field imaging mode. In this mode the contrast formation is formed directly by occlusion and absorption of electrons in the sample. In the bright field mode, an aperture in placed in the back focal plane of objective lens which allows only the direct beam to pass.

In this case, the image results from a weakening of the direct beam by its interaction with the sample. As the electron beam passes through the sample, it is affected by the structure and

composition of samples. Thicker regions of the samples or regions with a higher atomic number or crystalline areas will appear dark while regions with no sample will appear bright. The transmitted beam is then projected into a phosphor viewing screen or to be detected by a CCD camera. A TEM gives sub nanometer resolution but it requires extensive sample preparation for high resolution imaging.

The nanoscale morphology of the material was characterized by the JEOL2011 transmission electron microscopy operated at 200 keV with LAB6 filament as the electron beam source. Also a Gat an Imaging Filter 2000 system connects to the TEM offered us access to element maps, using energy transmission electron microscopy. The resolution of energy filter is 1 eV and the dimensional is 1 nm.

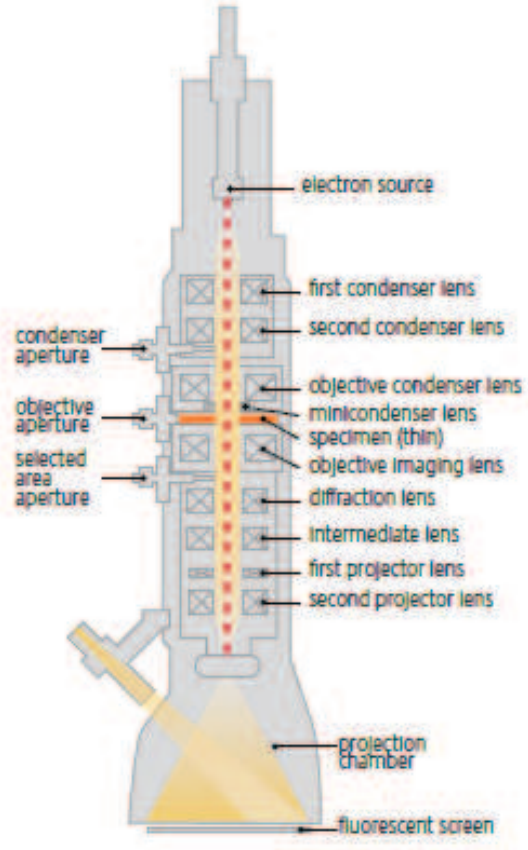

Figure 2.5: The schematic outline of a TEM.

2.3. Brunauer-Emmett-Teller method

Brunauer-Emmett-Teller (BET) is an important analysis technique for the measurement of the specific surface area of a material. The first article about the BET theory in the Journal

of the American Chemical Society in 1938 was published by Stephen Brunauer, Paul Hugh Emmett and Edward Teller [Brunauer 1938].

The BET method permits a calculation of a surface area of solids by a physical adsorption of gas molecules on the surface of the solid which relied on the concept of the theory developed to multilayer adsorption from the Langmuir's derivation using for monolayer molecular adsorption. The physical adsorption results from relatively weak forces (van der Waals forces) between the adsorbate gas molecules and the adsorbent surface area of the test material [Brunauer 1937].

The measurement process passes thought several steps; the first a sample must be degassed to remove water. The sample is contained in glass cell with glass rod within the cell to minimize a dead space in a cell. This cell is placed into heating mantles and connected to the outgas port of the machine. After, a sample is degassed in a vacuum at high temperature (in this case using 120 °C) which will not damage the structure of sample and the smallest degassing times. A minimum mass weight of sample is required for the BET to successfully determine the surface area which is 0.2 g.

And then, the cell is moved to the analysis port (Figure 2.6). The liquid nitrogen is used to keep cool the sample at a constant temperature. Because of the interaction between the gas molecules and the surface of the sample will be strong enough for measurable amounts of adsorption to occur in low temperature. The nitrogen gas in this case is injected into a sample cell with a calibrated piston. The volume in the sample cell must be calibrated before and after each measurement by using a helium gas for a blank run, because a helium gas does not adsorb onto the sample.

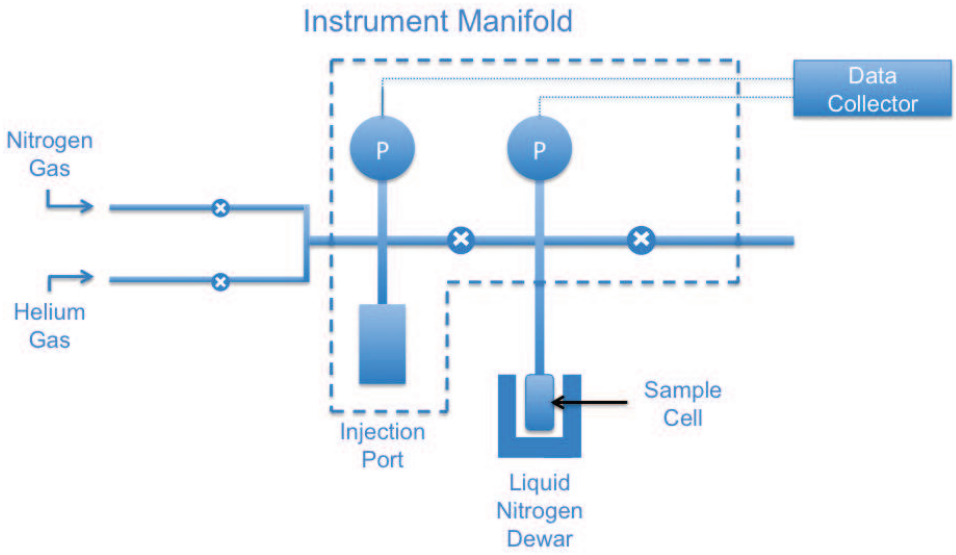

Figure 2.6: Schematic diagram of BET.

2.4. Inductively Coupled Plasma/ Optical Emission Spectrometry

Inductively Coupled Plasma/ Optical Emission Spectrometry (ICP/OES) is an analytical technique used for the detection identify and quality of elements in materials. The technique is based on the spontaneous emission of photons from atoms and ions that have been excited in a radio frequency discharge [Xiandeng 2000].

The ICP/OES system is relatively simple components: a sample introduction system (nebulizer), an ICP torch, a high frequency (HF) generator, transfer optics, a spectrometry and a computer interface. The sample employs into the ICP as liquid form, for solid sample which has to convert to liquid by dissolve it into proper solvent [Skoog 1998, Xiandeng 2000].

The sample solution is exchanged to an aerosol and passed through the central channel of the plasma. Herein, the aerosol is quickly vaporized under an effect of the very high temperature (10.000 K). These elements need to analyze which are liberated as free atoms in the gaseous situation. Moreover, they were excited by additional energy to the atoms of the collisional excitation within the plasma imparts. This energy is available to convert the atoms to ions and promote the ions to excited states. The atomic and ionic excited state species undergo the ground state via the emission of a photon. These photons have characteristic energies that are determined by the quantized energy level structure for the atoms or ions. Therefore, the original elements were identified by the wavelength of the photons and the

concentration of the originating element in the sample is directly proportional to the total number of photons [Francis 2007].

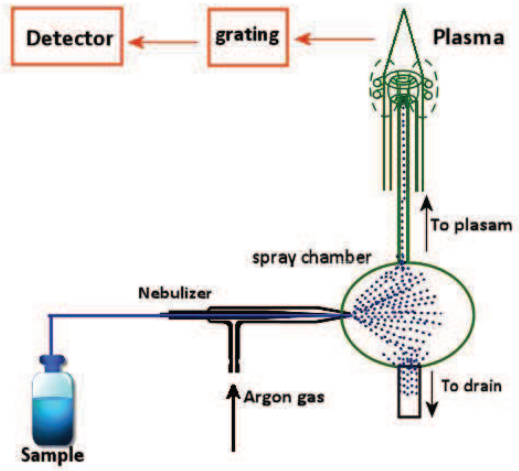

Figure 2.7: Schematic diagram of ICP.

2.5. Thermogravimetric analysis

Thermogravimetric analysis (TGA) is a technique measurement the different weight of a substance when a sample in a furnace with temperature increasing and the unit remains outside of the furnace. The sample's weight is function of a temperature or a time [Redrern 1963]. In the TGA, the mass loss is observed by a thermal event involves loss with volatiles components such as solvent and plasticizers in polymers, water of hydration in inorganic materials.

Thermogravimetric analysis (TGA) based on a high quality in three measurements: a mass change, a temperature and a temperature change. Thus, the main requirements for TGA are an absolute balance with the specimen and a reference sample and a programmable furnace. The furnace must keep a constant heating rate due to the mass loss constant following the time.

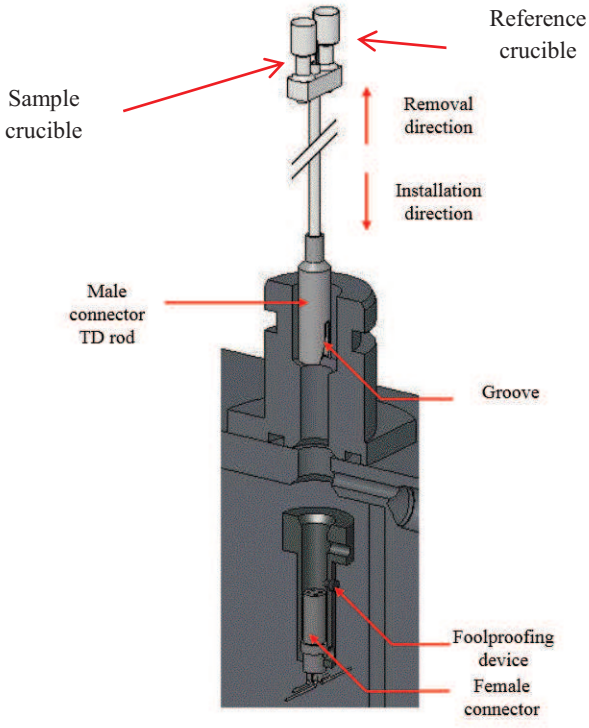

Figure 2.8: Schematic diagram of TGA.

The TGA continuously weighs a sample while the temperatures up to 1200 °C (or more than depending on the goal) which lead to various components of sample which are decomposed and the weight percentage of each resulting mass change can be measured. The rate of increment between 0.1 and 50 °C/min in argon flow 50 mL/min and a sample mass is 20 mg. The result is presented by the plot of temperature on the horizontal-axis and mass loss on the vertical-axis.

2.6. UV-visible luminescence spectra

Fluorescence spectroscopy is a type of electromagnetic spectroscopy techniques for analyzes fluorescence of a sample. This technique usually uses an ultraviolet light as a source of light for excitations of the electrons in the molecule.

Basically, this method is primarily concerned with electronic and vibrational states. Normally, the molecule exists at a ground electronic state with a low energy state and a molecule should be excited by absorbing a photon. Due to, the molecule jumps to higher

energy and survives at an excited electronic state. Within each of these electronic states are various vibrational states. In the same time, a molecule can lose some part of vibrational energy until it reaches the lowest vibrational state. Finally, the excited molecule emits a photon to change its state for a ground state. The frequency of the emitted photon varies enormously, because the ground state of the molecule also possesses several vibrational states. Thus, analyzing the different frequencies of the emitted light and their relative intensity allows determining the variety of electronic states of the molecules involved in the study.

The fluorescence spectroscopy technique includes the study two types of spectra: the different wavelength values of light emitted by the sample, while the excitation wavelength remains a constant value, make an emission spectrum. An excitation spectrum is the opposite, while the emission light is held at the constant wavelength, the variety of an excited wavelength make the excitation spectrum.

The luminescence properties of the samples were studied by the using VUV synchrotron-radiation (SR) source of DORIS storage ring at HASYLAB (DESY, Hamburg). The fundamental satiation of the SUPERLUMI used in the experiments which is described in details reference [Zimmerer 1991]. The opportunities for time- and energy-resolved vacuum fluorescence spectroscopy are provided by the use of ultraviolet light, generated by the DORIS-III storage ring. Energy range of the photons, used in the experiment, is located from, 1.2 eV to 25 eV. The experiment chamber is evacuated to ultra-high vacuum conditions to avoid absorption losses in the VUV spectral region. The schematic presentation of the SUPERLUMI set-up is shown on the Fig. 2.9.

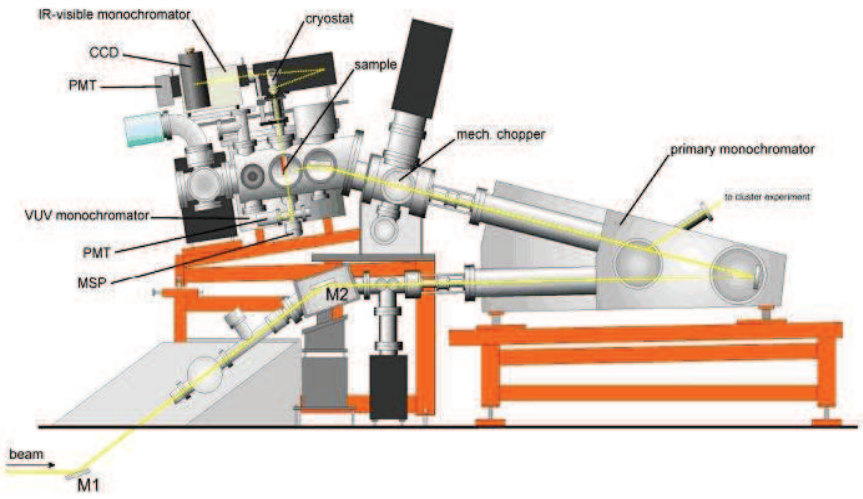

Figure 2.9: Schematic presentation of the basic components of a SUPERLUMI fluorescence spectrometer.

The sample was cooled down to 8 K and irradiated by monochromatized SR($\Delta\lambda = 3.3\,\mathring{A}$) under high vacuum (~10^{-9} mbar). The measurements of luminescence spectra were carried out using a visible 0.275 m ARC Spectra Pro-300i monochromator equipped with a CCD detector cooled with liquid nitrogen or R6358P photomultiplier (Hamamatsu) operating in the photon-counting mode. The pulse structure of SR (130 ps, 10 MHz repetition rate) enables time-resolved luminescence analysis at time-scale of 100 ns with sub-nanosecond temporal resolution. Spectra were recorded within a time gate $\Delta\tau$ delayed after the SR excitation pulse. Typically two time gates have been used simultaneously: a fast one of $\Delta\tau_1$=1-4 ns and a slow one of $\Delta\tau_2$=25-100 ns. Complementary, luminescence decay curves were measured at fixed excitation and luminescence photon energies. The recorded excitation spectra were corrected for the primary monochromator reflectivity (using sodium salicylate phosphor) and SR current.

Chapter 3
Elaboration of nanofibrous alumina

In this chapter, we discuss elaboration of the UPA monoliths and their morphological and structural transformation during the subsequent thermal treatment. The phase transformations with an increase of temperature correlate with changes of density, composition and structural fibril length and diameter. After the work by Frappart [Frappart 2000], who has analysed the the effect of Al metal precursor and its purity on the growth kinetics and purity of the final monolithic oxidized material, we have precised the possible role of amalgam filtering on the UPA growth kinetics and purity.

3.1. Metallic precursors

3.1.1. Materials

The laminated technical aluminum (Al-Tech, 11069-2001 Ukraine, purity indicated in Annex 1), laminated high purity aluminum (Al-HP, Goodfellow, purity indicated in Annex 1) and high purity mono-crystalline aluminum (Al-Mono HP, PhTI Kharkov - Ukraine, purity indicated in Annex 1) were used in this investigation with the different elemental compositions. The thicknesses of metallic Al plates are: Al-Tech - 4.9 mm, Al-HP - 1 mm and Al-Mono HP - 1.3 mm.

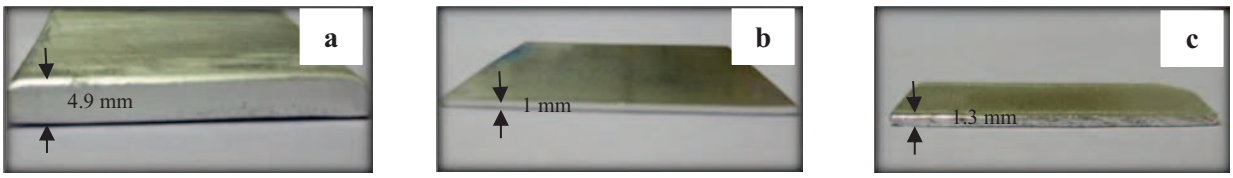

Figure 3.1: Aluminum plates used for UPA growth (a) Al-Tech, (b) Al-HP, (c) Al-Mono HP.

3.1.2. Purity measurements of aluminum precursors

These impurities were analyzed by Inductive Coupled Plasma / Optical Emission Spectrometry (ICP/OES) method. The mass 0.20 g (±10 %) of each aluminum sample was added to 20 mL of 10 % NaOH solution and kept at 60 °C under ultrasound overnight until a complete dissolution. The elemental content was obtained with the random error analysis characterized by the relative standard deviation of 0.4 % and expressed in ppm units.

Because of using NaOH solution to dissolve metals in the experiment, little amount of some elements which supplied from this solution. Furthermore, the amalgam used for the

UPA growth might also be a source of the UPA contamination. The elemental content in aluminum plates data obtained from these experiments are presented in Tables 3.1, 3.2, 3.3, 3.4 and 3.5 below.

Table 3.1: NaOH solvent

Element	ppm
Hg	0.2120
Al	0.7321
Mg	0.0116
Zn	0.0132
Cu	0.0003
Fe	0.0380

Table 3.2: Amalgam

Element	$Hg(NO_3)_2$	$AgNO_3$
Ga (ppm)	0.0161	0.0063

Table 3.3: Al-Tech

Al-Tech	real mass (mg)	mass of each element / total mass	Atomic concentration (ppm)
Al	80.067	0.9979	998600
Si	0.05832	0.0007268	688
Fe	0.04205	0.0005240	250
Cu	0.03851	0.0004800	201
Mn	0.008409	0.0001048	50.7
Mg	0.009096	0.0001134	124
Zn	0	0	0
Ga	0.002183	0.0000272	10.4
Ti	0.003021	0.0003765	20.9
Hg	0.003014	0.0000376	4.98
Ag	0.0002568	0.0000032	0.434

Table 3.4: Mass of each element in Al-HP

Al- HP	real mass (mg)	mass of each element / total mass	Atomic concentration (ppm)
Al	172.892	0.9997	999700
Si	0.05123	0.0002962	280.4
Fe	0	0	0
Cu	0.0002111	0.0000012	0.5128
Mn	0.0002297	0.0000013	0.6239
Mg	0	0	0
Zn	0	0	0
Ga	0.0001142	0.0000007	0.2535
Ti	0.0005043	0.0000023	1.621
Hg	0.003014	0.0000174	2.310
Ag	0.0000852	0.0000005	0.0665

Table 3.5: Mass of each element in Al-Mono HP

Al- Mono HP	real mass (mg)	mass of each element / total mass	Atomic ratio of each element per Al (ppm)
Al	169.299	0.9995	999600
Si	0.0786	0.000464	439.2
Fe	0	0	0
Cu	0.0000967	0.0000006	0.2388
Mn	0.0002385	0.0000014	0.6799
Mg	0	0	0
Zn	0	0	0
Ga	0.0001054	0.0000007	0.2363
Ti	0.0003415	0.0000020	1.118
Hg	0.0030140	0.0000178	2.358
Ag	0.0000808	0.0000005	0.0647

We notice that Al-Tech has the percentage of each impurity higher than Al-HP and Al-Mono HP. The Zn element has no appearance in all plates and Fe, Mg do not exist in Al-HP and Al-Mono HP. However, other quantity of elements: Si, Fe, Hg, Ag of the Al-Mono HP is the lowest. We also notice that although Si content in Al-Tech plate (Table 3.3) corresponds to that indicated by the supplier (seer Annex 1), that in Al-HP and Al-Mono HP plates was found significantly higher (compare between Tables 3.4 / 3.5 and Annex 1). Although the reason of this unusual contamination remains unknown, one may suggest that it comes during the sample preparation stage. The obtained results, schematically summarized in Figure 3.2, permit concluding about highest purity of Al-Mono HP between the three precursors.

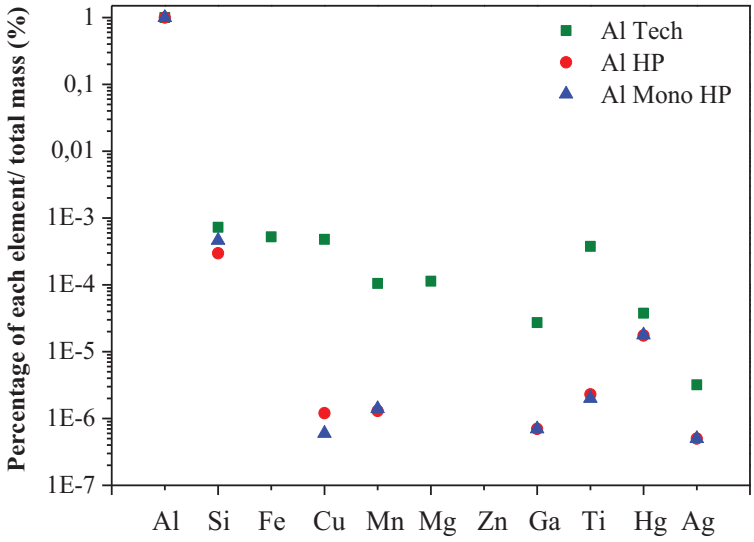

Figure 3.2: Percentage of each element/ total mass of Al-Tech, Al-HP and Al-Mono HP.

3.2. Synthesis of ultra-porous alumina (UPA)

3.2.1. Materials and conditions

3.2.1.1. Materials

The oxidation process was conducted on aluminum plates of 1 mm thickness cut in squares of size of 5x5 cm.

3.2.1.2. Conditions

The growth of alumina monoliths was carried out in a climate chamber allowed to control the humidity and temperature or ambient air. The aluminum substrate was tightly mounted on

the surface of a radiator Duralumin (25x25 cm) that was cooled by a thermostatically controlled water flow at 20 °C. The aluminum was grown until its length attains about 13 to 16 cm, typically during a time shorter than 20 hours.

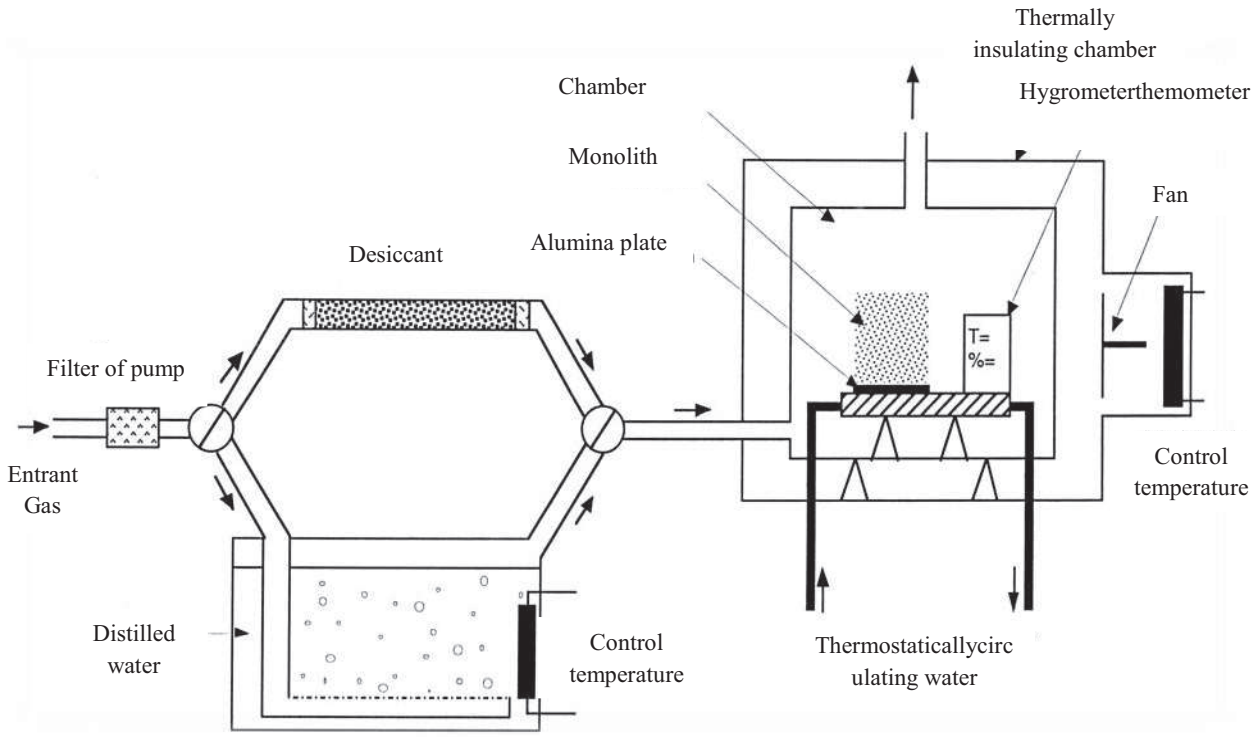

Figure 3.3: Diagram of the climatic chamber for the growth of the monolith [Frappart 2000].

- Pressure

In the experiment, the gas air brings oxygen and water vapor by through a water tank where temperature can set up according to the desired moisture. The flow gas is controlled by a valve connected to the compressed air system of the laboratory (in our case we used the flow gas: 2 $m^3 .h^{-1}$).

- Humidity

The moisture is the ratio of the partial pressure of water vapor on the saturated vapor pressure of water at the temperature. It is measured directly by the hygrometer inside the climatic chamber and the value is between 70 and 80 %.

- Temperature

The climate chamber is heated by a resistor, a fan for homogenizing the temperature. The latter is measured by a thermometer placed near the sample. Its value is 22 to 25 °C.

3.2.2. Process

3.2.2.1. Depassivation

One side of the aluminum plate is soaked in a 10 % sodium hydroxide solution (2.5 mol/L) to remove the passive alumina layer that covers it after was cleaned by acetone. We observe when the aluminum was moved, the air bubbles appeared that is hydrogen corresponding to the oxidation reactions of aluminum. They we reported by equations below:

$$Al_2O_{3\,(s)} + 2\,OH^- \rightarrow 2\,AlO_2^- + H_2O$$

$$2\,Al_{\,(s)} + 2\,OH^- + 2\,H_2O \rightarrow 2\,AlO_2^- + 3\,H_{2\,(g)}$$

When gas evolution is homogeneous over the entire surface of the plate after 2 minutes contacting, we can assert that it is de-passivate.

Rinsing the de-passivated surface by distilled water will happen reaction between aluminum with water that in agent to prevent developing of a non-passivating aluminum layer:

$$Al_{(s)} + 3\,H_2O \rightarrow Al(OH)_{3\,(s)} + 3/2\,H_{2\,(g)}$$

The most important note in experiment, we avoided the directly contact of the de-passivated surface with atmospheric air by the way continue to keep water on the surface of plate before contact with mercury solution.

3.2.2.2. Amalgamation

The passivated surface of the aluminum was treated by solution mixing between a solution of silver nitrate 0.02 mol/L and a mercury (II) nitrate solution 0.1 mol/L in solution of nitric acid 2 mol/L in 5 minutes.

Mercury has an essential role in the oxidation of aluminum. Mercury is a catalytic which prevents the aluminum surface to be in contact with the oxygen in the air, thus preventing the formation of a passive oxide film. The metal part of aluminum was dissolved by mercury, it allows the aluminum atoms rapidly disseminate to the surface at room temperature according

Pinnel and Bennet [Pinnel 1972]. Mercury is deposited on the aluminum plate at the same time flowing to the redox reactions:

$$2\ Al_{(s)} + 3\ Hg^{2+} \rightarrow 2\ Al^{3+} + 3\ Hg_{(l)}$$

$$Al_{(s)} + 3\ Ag^{+} \rightarrow Al^{3+} + 3\ Ag_{(s)}$$

These steps and standard conditions of synthesis process alumina were presented in Table 3.6 and Figure 3.4.

Table 3.6: Standard conditions of synthesis process alumina

Aluminum plate	Goodfellow, high purity (>99.999 %)
Temperature inside the climatic chamber	22-25 °C
Temperature of radiator cooling water	20 °C
Humidity	70-80 %
The flow air in the climatic chamber	2 $m^3.h^{-1}$
Duration of the depassivation	2 min
Duration of the amalgamation	5 min

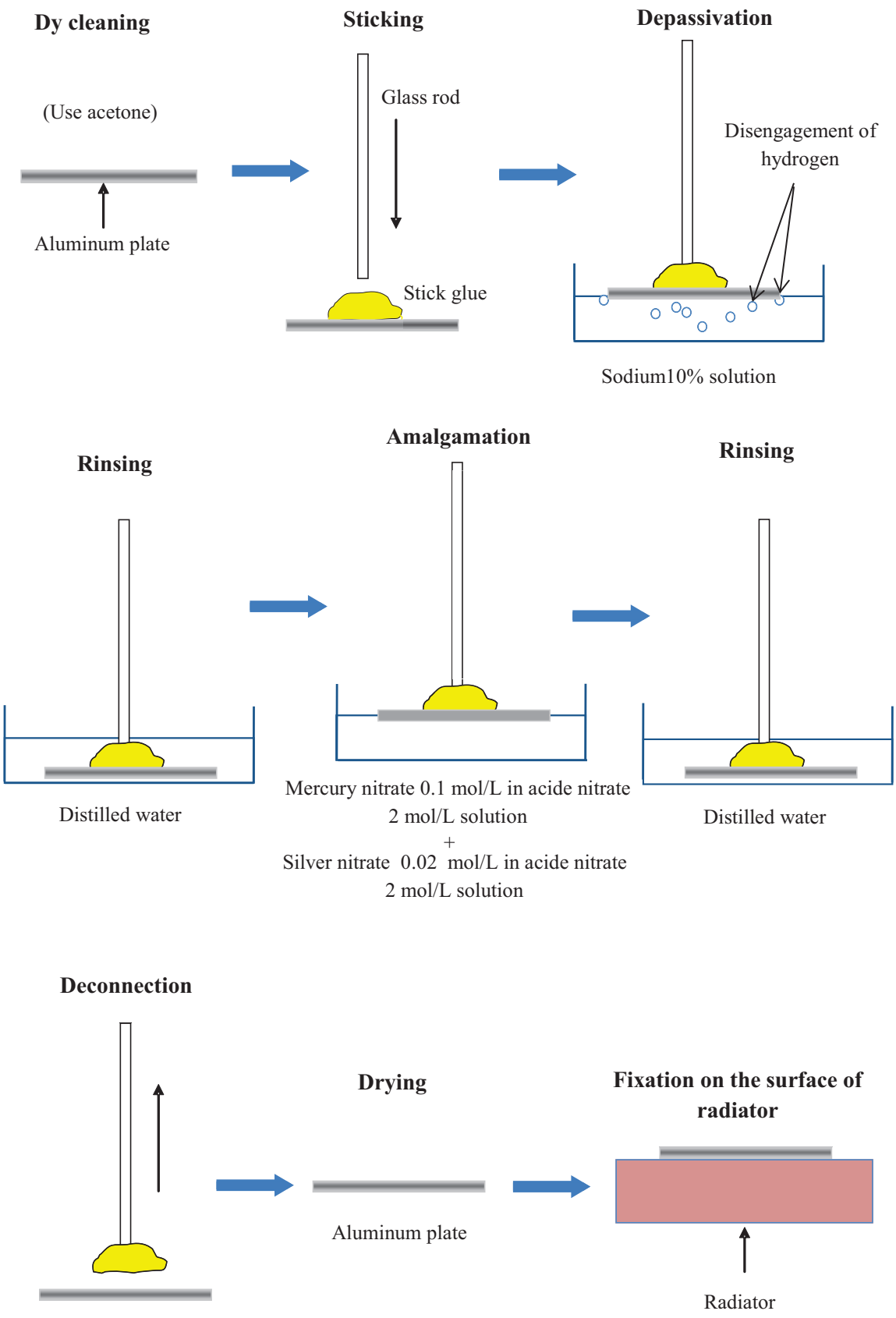

Figure 3.4: Protocol of an alumina synthesis (inspired from [Frappart 2000]).

3.2.3. The growth speed

The growth of UPA monoliths starting with Al-Tech, Al-HP and Al-Mono HP metallic precursor plates were performed the same procedure in standard conditions listen in Table 3.6. A micro web-camera was used to monitor the growth kinetics.

The images of the three materials after 1, 3 and 8 hours growth are shown in Fig. 3.5.

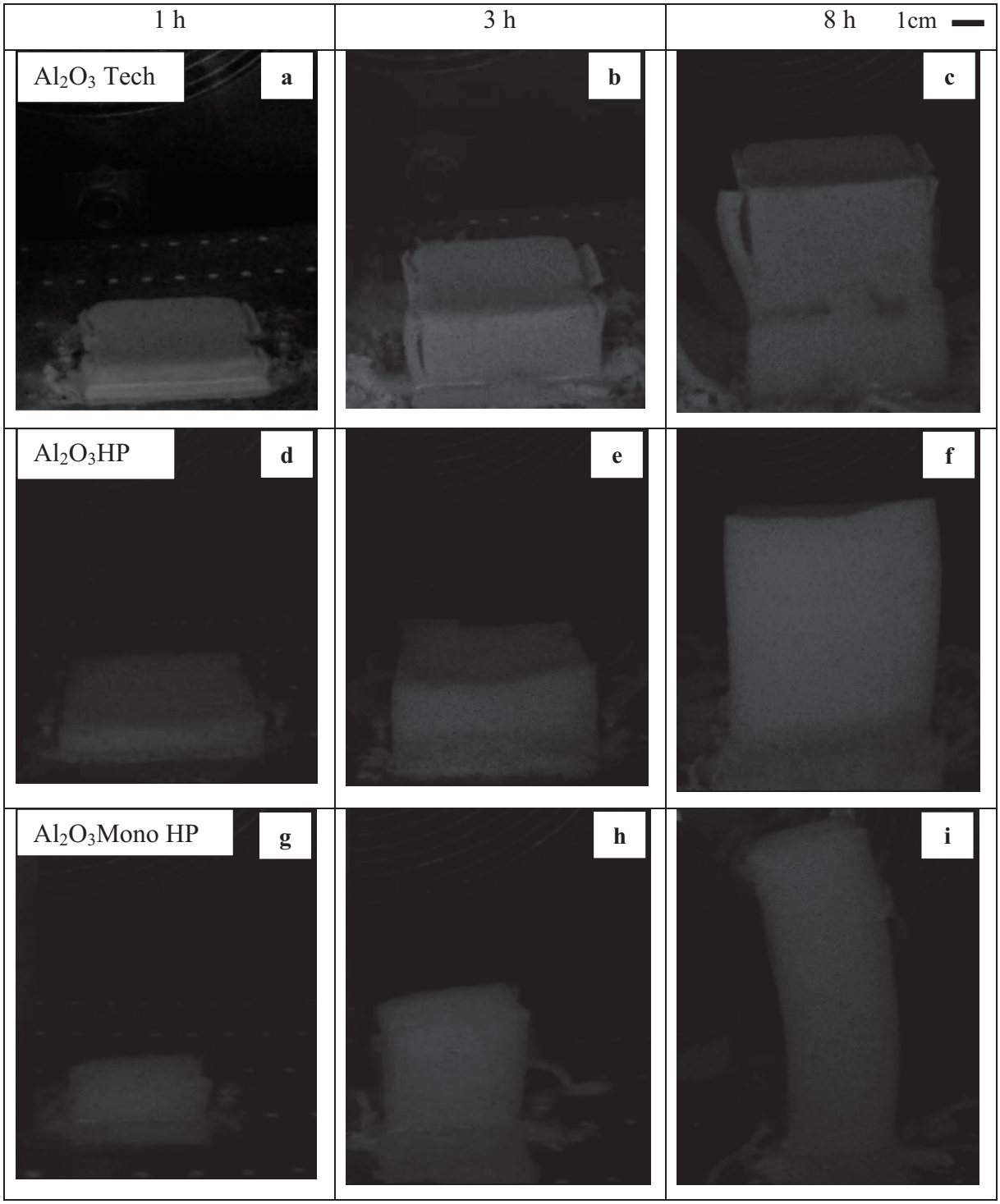

Figure 3.5: Images of growth of Al_2O_3-Tech, Al_2O_3-HP and Al_2O_3-Mono HP (a, d, g), (b, e, h), (c, f, i) corresponding with 1 h, 3 h, 8 h coarsening.

The normal appearance of the monoliths columns after continuous process during 16 hours using Al_2O_3-Tech and Al_2O_3-HP, during 9 hours using Al_2O_3-Mono HP are shown in Figure 3.6. We remark a light gray color of UPA monoliths produces with Al_2O_3-Tech precursor, which is seemingly explained by impurities originating from the most contaminated Al_2O_3-Tech precursor; in contrast, monoliths produced with Al_2O_3-Mono HP and Al_2O_3-HP precursors were of white color. We would like to notice that the perimeter parts of UPA monoliths grow in a different from the central one due to the boarder effect. They detach from the central part forming rolled bands, representing little mass that does not appreciably affect the overall monolith grow kinetics.

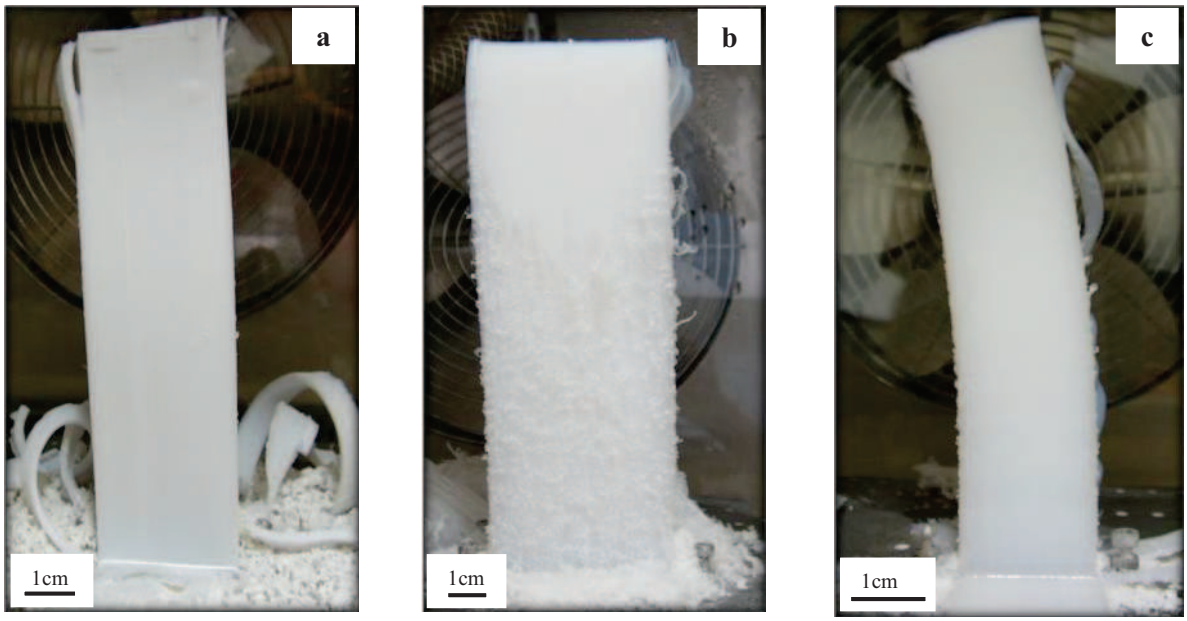

Figure 3.6 Aluminas (a) Al_2O_3-Tech, (b) Al_2O_3-HP, (c) Al_2O_3-Mono HP.

The growth rates of UPA monoliths starting with three metallic precursors are shown in Figure 3.7. The growth speed of alumina is the function of time with the average speed of each alumina as follows the Al_2O_3-Tech: 0.77 cm/h and mass density 0.018 g/cm^3, the Al_2O_3-HP: 0.99 cm/h and mass density 0.025 g/cm^3, and Al_2O_3-Mono HP: 1.1 cm/h and 0.027 g/cm^3 in mass density.

Evidently, the growth kinetics starting with the polycrystalline metals (Al_2O_3-Tech and Al_2O_3-HP) is significantly slower compared to those starting with the monocrystalline one (Al_2O_3-Mono HP). We also assume that with the highest purity alumina Mono HP has the highest speed growth. According to Frappart [Frappart 2000], this phenomenon is related to

the face orientation of the crystalline aluminum. This is true for the initial growth (t≈0); however not for the late stage (t>>0), at which the contamination of the amalgam may interfere by the slowing down the Al atoms diffusion flow through the amalgam. We expected to see this effect in Fig. 3.7 by the growth saturation. In contract, the growth seems to accelerate at the late times of the elaboration process. This could be attributed to the amalgam thinning due to weak evaporation of Hg and/or Ag depletion since Ag decreases the Al growth rate (see Table III.7 and Fig. 3.9 in [Frappart 2000]). However, losses of Ag seem unlikely to be a source of the growth increase observed in this work, since the initial concentration of Ag in the amalgam (0.02 mol/L) is much higher than that critical one ~$5 \cdot 10^{-4}$ mol/L, below which the acceleration effect becomes significant [Frappart 2000]. We may suppose therefore that the amalgam thinning corresponds to the observed growth kinetics in Fig. 3.7. More elemental analyses at different heights of UPA monoliths (correspondent to different growth times) will clarify this point.

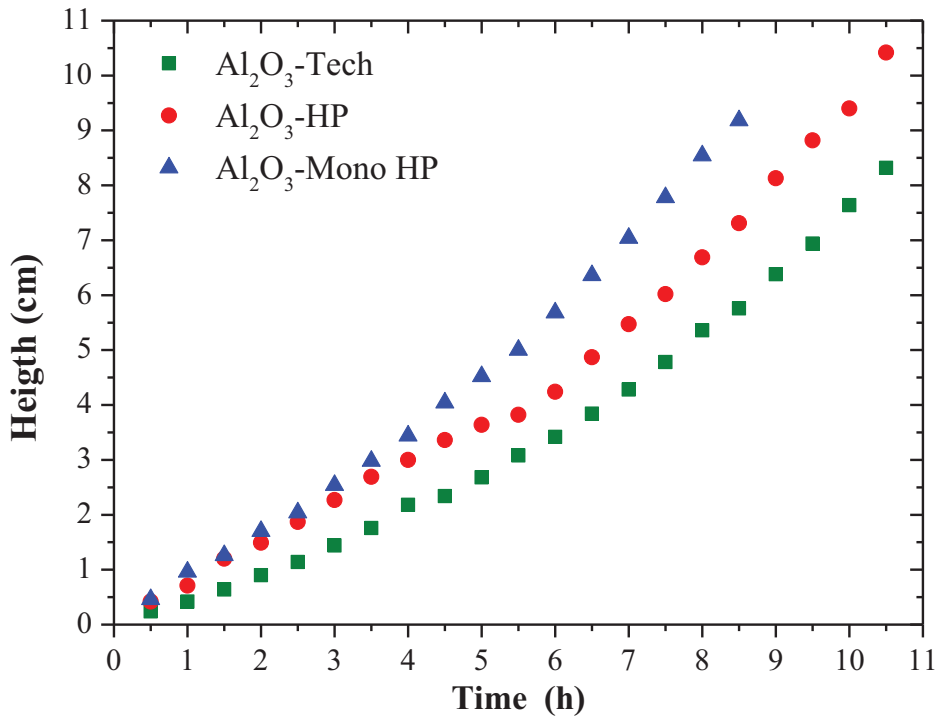

Figure 3.7: Growth rate of UPA monoliths starting with different indicated metallic precursors.

3.2.4. Impurities of alumina monoliths

The impurities in the metallic precursors affect the growth process but also, by passing through the amalgam, may contaminate the UPA monoliths. On could expect that because the elemental solubility differs, the amalgam can serve a filter reducing the impurity content in the final material. However for low impurity content, such filtration cannot be efficient. To address this point, we have carried out the elemental ICP/OES analysis of the grown UPA materials starting with three metallic precursors: Al_2O_3-Tech, Al_2O_3-HP and Al_2O_3-Mono HP. The analytic sample preparation is described in Chapter 3.1.2. Complementary, the UPA materials before dissolution in NaOH were pretreated at 400 °C during 4 hours in order to eliminate a considerable amount of the structural and adsorbed water (see Chapter 3.3 below). The results of these measurements in UPA grown with Al_2O_3-Tech, Al_2O_3-HP and Al_2O_3-Mono HP precursors are summarized respectively in Tables 3.7, 3.8 and 3.9.

The result achieved thought the calculation data from experiments with the same way like aluminum plates which were presented in these Tables 3.7, 3.8, 3.9:

Table 3.7: Al_2O_3-Tech

Al_2O_3- Tech	real mass (mg)	mass of each element / total mass	Atomic concentration (ppm)
Al	75.271	0.9972	999600
Si	0.00526	0.0000698	66.17
Fe	0	0	0
Cu	0	0	0
Mn	0.0000045	0.00000006	0.02912
Mg	0	0	0
Zn	0	0	0
Ga	0.00131	0.00001735	6.630
Ti	0.0002711	0.00000359	1.999
Hg	0.2054	0.002721	361.5
Ag	0.0002744	0.00000364	0.4927

Table 3.8: Al_2O_3 -HP

Al_2O_3 -HP	real mass (mg)	mass of each element / total mass	Atomic concentration (ppm)
Al	88.009	0.9987	999800
Si	0.00526	0.00005964	56.51
Fe	0	0	0
Cu	0	0	0
Mn	0.00000088	0.00000001	0.0048
Mg	0	0	0
Zn	0	0	0
Ga	0.0001098	0.00000125	0.4754
Ti	0.00002908	0.00000033	0.043
Hg	0.1130	0.001282	170.1
Ag	0.0001072	0.00000122	0.1647

Table 3.9: Al_2O_3 -Mono HP

Al_2O_3 -Mono HP	real mass (mg)	mass of each element / total mass	Atomic concentration (ppm)
Al	88.05	0.9987	999700
Si	0.01045	0.0001185	112.3
Fe	0	0	0
Cu	0	0	0
Mn	0.0000009	0.000000001	0.0048
Mg	0	0	0
Zn	0	0	0
Ga	0.0000966	0.000001095	0.4181
Ti	0.0001083	0.000001228	0.6825
Hg	0.10641	0.001207	160.1
Ag	0.0000764	0.000000866	0.1173

The impurity gain in UPA compared to the three precursors is shown in Figure 3.8. According to this figure, we consider the purity of UPA increases or decreases when the gain is respectively below or above 1; in case of values close to 1 the amalgam effect was considered as neutral.

Based on these measurements, we can conclude about only partial elemental filtering by the Hg-Ag amalgam during the growth process. Indeed, three groups of elements can be distinguished:

- Si, Fe, Cu, Mn, Ti and Mg content in alumina decreases in UPA compared to the metallic precursors.

- The purification does not or little affects Ga and Ag elements.

- The content of Hg element considerably increases in raw UPA.

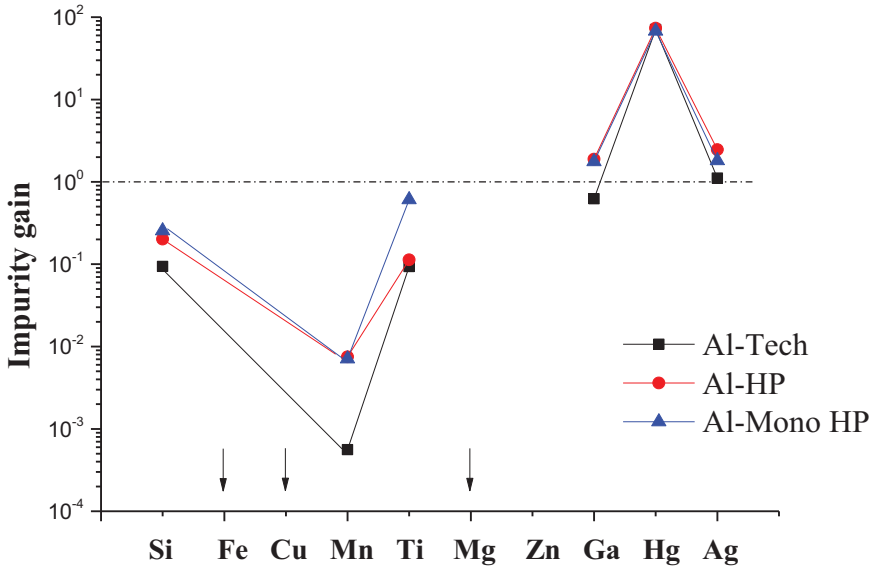

Figure 3.8: Impurity gain in UPA grown on Al-Tech, Al-HP and Al-Mono HP metallic precursors. Arrows indicate elements which were present in Al-Tech plate and not found in Al_2O_3-Tech monolith.

The results concerning the first group of elements (Si, Fe, Cu, Mn, Ti and Mg) are in a general agreement with conclusions by Frappart [Frappart 2000], who has provided a detailed analysis of the UPA contamination with Si, Cu, Mg and Fe elements. In particularly, this has been explained by a poor solubility of Si and Fe elements in the amalgam. Concerning Cu, it forms solid species Cu_7Hg_6 with Hg in the amalgam, which are weakly entrained in the grown monolith. Mg is more soluble in Hg than Al and less oxidized therefore accumulating in the

amalgam; its concentration little or not changed. Consequently, the contamination of the monolith by this element may depend on the growth time and consequently on the monolith section used for the analysis (upper or lower). Such analysis could be suitable to perform in future studies in order to verify this hypothesis.

Compared to the first group of elements discussed above, the solubility of Ga in the amalgam is high [Frappart 2000]. One can expect therefore much smaller filtering effect of this element by Hg-Ag amalgam. Indeed, Ga impurities were almost not influenced by the UPA growth process. One can see however, that Al_2O_3 -Mono HP and Al_2O_3 -Mono HP monoliths are much smaller contaminated by Ga compared to Al_2O_3 -Tech one. One can therefore suppose that Ga impurity is advantageously dragged through the amalgam to UPA monolith when the most contaminated Al-Tech metallic plates were used.

Concerning Hg element, its presence in the precursor is negligibly small and appearance in UPA does almost not depend on the metallic precursor purity. The source of this impurity, as evidences Table 3.2, is amalgam and the UPA contamination may be decreased by optimization of the growth process. According to recent studies [Odanović 2004], thermal post-treatment above 800 °C will completely remove Hg from the monoliths.

Since Ag contamination of the metallic plates is small, this element may be additionally entrained into the monolith structure from amalgam during the growth stage. However, properly designed process (in terms of amalgam preparation, temperature and humidity) permits almost to avoid the contamination, which remain on ~0.1 ppm level.

3.2.5. The micro-structure of aluminas

The X-ray diffraction measurements shown in Figure 3.9 evidence that Al_2O_3-Tech, Al_2O_3-HP and Al_2O_3-Mono HP have similarity crystalline structures. These after heating at 1150 °C during 4 hours show mixed θ and α polymorphs with the most narrow α-phase peaks. The α-phase is more present in Al_2O_3-Tech, which apparently is a catalyzing effect of impurities more present in this sample, as evidenced by our ICP analysis.

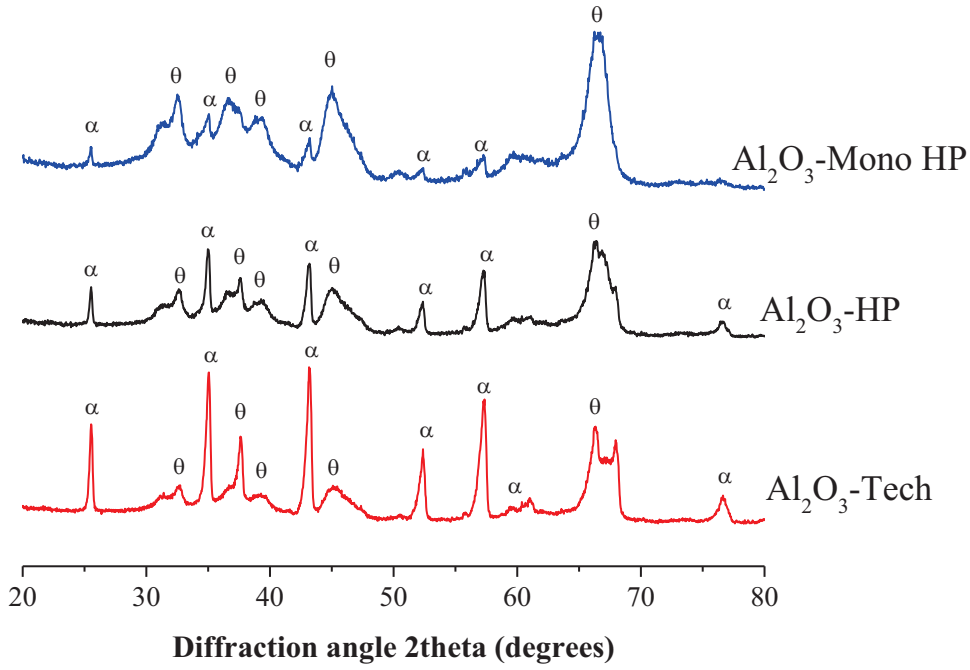

Figure 3.9: XRD of different UPA after thermal treatment at 1150 °C during 4 hours.

The microstructural of three samples at room temperature was shown by SEM analysis [Fig. 3.10] with similar entangled fibrils and 5-7 nm in the average diameter. The result confirms that the structure and diameter of fibril has no the significant difference between Al_2O_3-Tech, Al_2O_3-HP or Al_2O_3 -Mono HP.

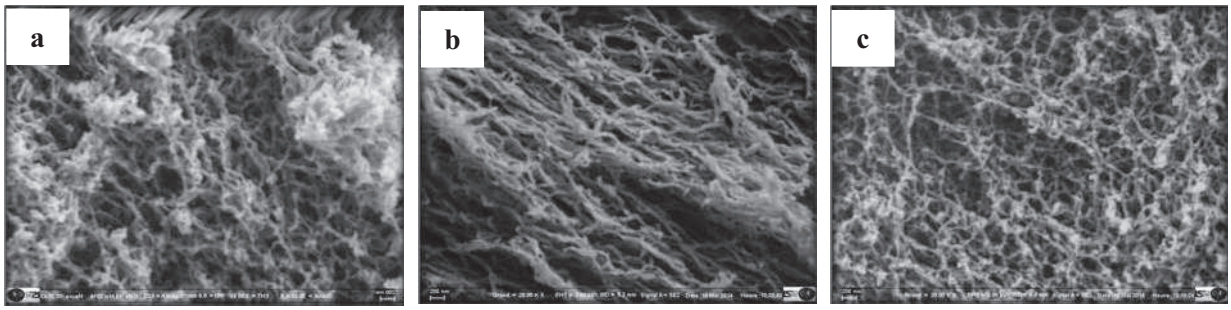

Figure 3.10: SEM images (a) Al_2O_3-Tech, (b) Al_2O_3-HP, (c) Al_2O_3-Mono HP (scale 200 nm).

3.3. Structural, chemical and phase transformations of alumina

In this PhD work, we have chosen the Al_2O_3-HP as the main object for investigation of the temperature annealing factors effect on the transformation phase of alumina.

3.3.1. Effect of annealing on structure composition

In the original condition the diameter of nanofibrils is about 5 nm [Vignes 1997] (see Fig. 1.17 in Chapter 1) and the UPA annealed at 400 °C (4 h) shown in Fig. 3.11a [Vignes 2008] evidence almost negligible thickening of the observed fibrils having the average diameter of 5-7 nm and length 120-140 nm. The electron diffraction patterns confirm their amorphous nature. Along with the increase of temperature, it leads to thicken and shorter of the nanofibrils as shown in SEM image (Fig. 3.11b) [Costanzo 2001] of well-crystallized α-Al_2O_3 particles formed from UPA fibrils at 1300 °C. The respective diameter of particles varies from 150 to 250 nm with the average value of ~200 nm.

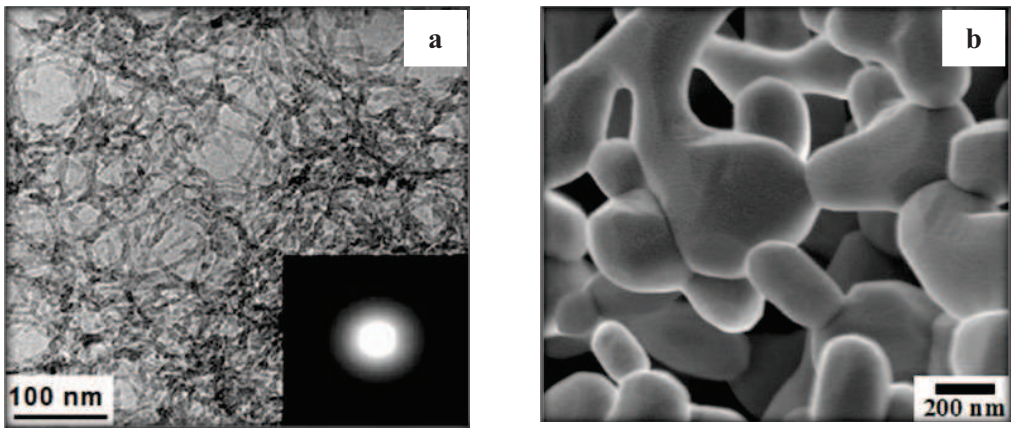

Figure 3.11: (a) TEM image of UPA sample annealed at 400℃ [Vignes 2008] and (b) SEM image of UPA sample annealed at 1300 °C [Costanzo 2001] (annealing time 4 hours).

The diameter fibrils of UPA have been raised following the heating UPA from room temperature to 1650 °C. The data from experiment was collected and presented under:

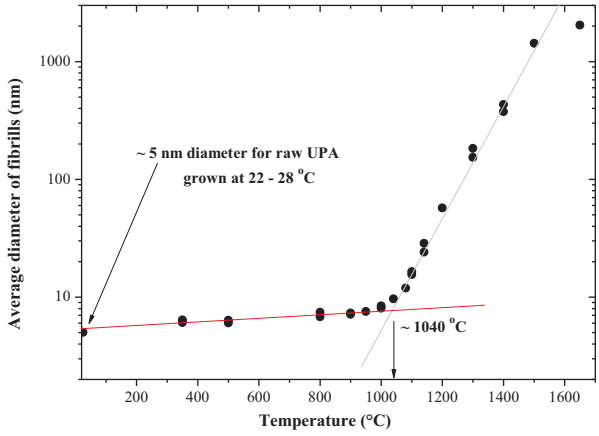

Figure 3.12: Mean diameter of fibrils versus treatment temperatures annealing during 4 hours.

3.3.2. Chemical and structural transformations

The XRD patterns of UPA heated at different temperatures are shown in Fig. 3.13. Up to temperatures ~600 °C they do not reveal any significant modification of the amorphous structure until 870 °C had been started modification. The experimental data and previous studies [Vignes 1997, Vignes 2008, Costanzo 2001] shown that UPA material at isochronous annealing of in the range of temperatures between 20 and 1600 °C passes series structural transitions from native supramolecular amorphous, γ phase, θ phase to stable α-crystalline state as summarised in Table 3.10. For a comparison, aluminum oxyhydroxydes obtained by chemical precipitation are also included in this table.

Table 3.10: Structural and phase transitions of UPA temperature during annealing in 4h

Phase transition		Temperature, ºC		
		UPA[(1)]	Oxyhydroxides [(2)] (chemical precipitation)	
			onset	completed
I-II	Mixed state: hydrated amorphous alumina with water	≤100	–	–
II	Amorphous structure, partially dehydrated	~450	–	–
II-III	Amorphous → γ-Al_2O_3	870	320-450	600 - 700
III-IV	γ-Al_2O_3 → θ-Al_2O_3	1000	830 - 950	1050
IV-V	θ-Al_2O_3 → α-Al_2O_3	1200	1050	1100

(1) Isochronous annealing during 4 hours (see Ref. [Stepanenko 2015])

(2) Ref. [Alwitt 1976, Poezd 1978, McHale 1997, Carim 1997, Vinogradov 2008]

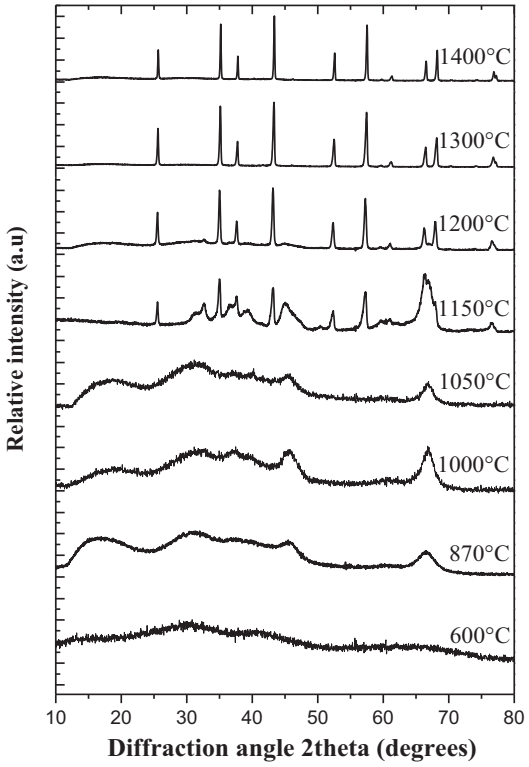

Figure 3.13: XRD patterns obtained from UPA samples after isochronous 4 hours annealing in air at different temperatures.

The very beginning of γ-phase crystallization from the amorphous alumina obtained by chemical precipitation can be detected at temperatures as low as ~400 °C (see Table 3.10), which follows from the detailed analysis of TEM electron diffraction patterns [Vignes 2008]. The crystallization is kinetically limited process and its rate is extremely slow in this range of temperatures. Moreover, crystallization of single (non-aggregated) nanofibrils can be delayed to higher temperatures due to a contribution of surface energy, in agreement with previous observations in oxide nanoparticles [Zhang 1998]. In particularly, the formation enthalpy of γ-Al_2O_3 was predicted to become lower compared to that of α-Al_2O_3 for materials with the surface area above ~125 m^2/g [McHale 1997, Navrotsky 2003] This effect also concerns crystallization from the amorphous phase [Khatim 2013] . We have found the crystallization of amorphous UPA fibrils at 870 °C in agreement with earlier published results [Frappart 2000, Vignes 2008].

The basic modifications of the chemical composition of UPA under annealing are related to losses of the adsorbed and structural water. The mass losses and related water content in

raw and thermally treated UPA samples in the temperature range 25-950 °C obtained from TG measurements are presented in Fig. 3.14.

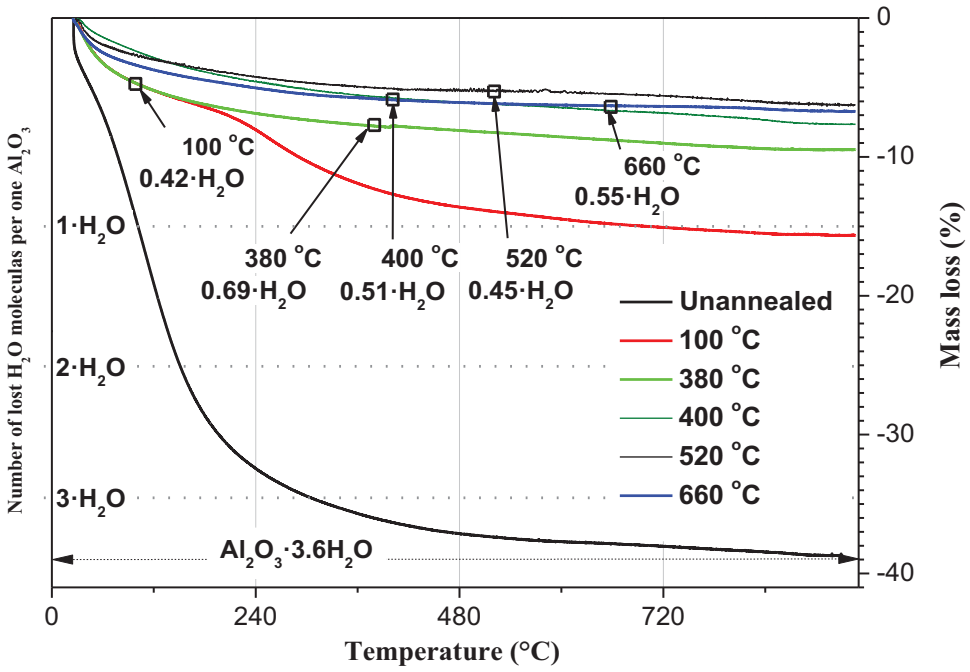

Figure 3.14: Total mass loss and number of lost water molecules per Al_2O_3 of UPA samples after annealing in air at different temperatures.

The UPA were in thermodynamic equilibrium with moisture of 80 % at 25 °C in the grow chamber before these measurements. The total number of water molecules n_x per Al_2O_3 in UPA samples annealed at temperature x °C and cooled in ambient air at room temperature, were obtained from the relative mass loss $\Delta_{x/950}$ of TG curves at T=950 °C according to:

$$n_x = \frac{M_{Al_2O_3} \cdot \Delta_{x/950}}{M_{H_2O} \cdot (1 - \Delta_{x/950})} \tag{3.1}$$

Where $M_{Al_2O_3}$ and M_{H_2O} are molar masses of aluminum oxide and water. Additionally and assuming that the desorption is completed at $x \geq 100$ °C, the number of reversibly adsorbed water molecules of UPA samples annealed at x °C can be obtained from TG curves at T=x °C according to:

$$n_{x\,ads} = \frac{M_{Al_2O_3} \cdot \Delta_{x/x}}{M_{H_2O} \cdot (1 - \Delta_{x/950})} \tag{3.2}$$

The x points and respective n_{ads} of the annealed samples are depicted in Fig. 3.14 by small open squares. Consequently, the number of structural water molecules n_{xstr} can be therefore calculated from $n_x = n_{xads} + n_{xstr}$. The obtained n, n_{ads} and n_{str} values for different annealing temperatures are summarized in Table 3.11. We notice that n_{ads} does not change significantly and small difference between these data fits confidence range of measurements.

Table 3.11: Analysis of water content in UPA samples: $Al_2O_3 \cdot nH_2O$ ($n = n_{str} + n_{ads}$)

molar ratio H_2O/Al_2O_3	annealing temperature °C					
	25	100	380	400	520	660
total water, n	3.57	1.45	0.88	0.71	0.58	0.62
adsorbed water, n_{ads}	0.38	0.42	0.69	0.51	0.45	0.55
structural water, n_{str}	3.19	1.03	0.19	0.2	0.13	0.07

As it follows from our experimental data, the raw UPA contains on average about 3.6 water molecules per Al_2O_3, which exceeds the water content in the stoichiometric hydroxide. This confirms that the raw UPA fibrils are composed of the aluminum oxyhydrates with excessive molecular water. The structural water removal takes place in the temperature range below 400 °C and is accompanied by a decomposition of raw UPA structure with partial dehydration of the amorphous oxyhydroxide. We notice that the stable compositions $Al_2O_3 \cdot 1.5H_2O$ and $Al_2O_3 \cdot 0.9H_2O$ are realized at respectively 100 and 380 °C. The last composition can be interpreted as amorphous phase of partially dehydrated boehmite ($Al_2O_3 \cdot H_2O$) in agreement with literature data about the beginning of γ-Al_2O_3 crystallisation (see Table 3.10). The further increase of temperature up to 700 °C moderately modifies the $Al_2O_3 \cdot xH_2O$ composition with x decreasing down to 0.4, which completes the formation of γ-phase at 870 °C in agreement with Vignes et al. [Vignes 2008].

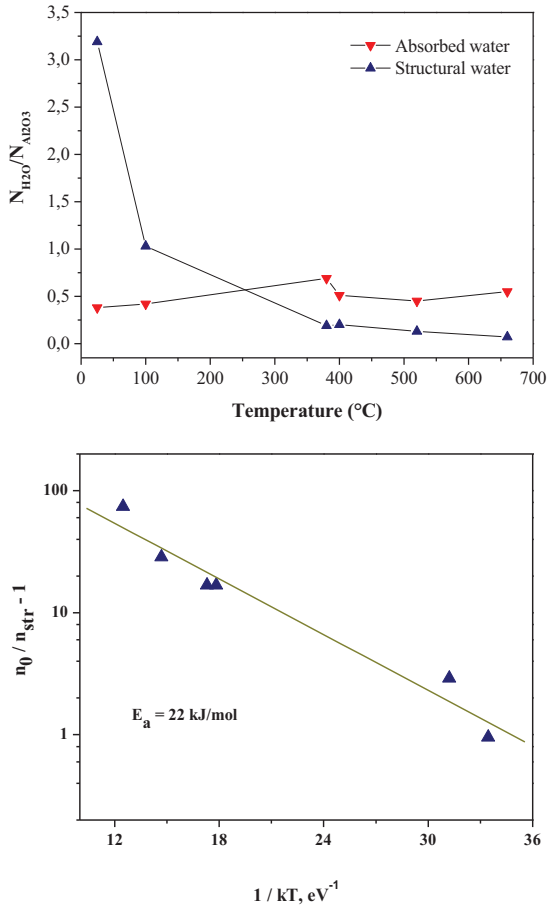

Figure 3.15: Number of structural and adsorbed water molecules per Al in the UPA structure versus annealing temperature from Table 3.11(a) and activation energy of the structural water removal (b).

The values n_{str} and n_{ads} are plotted in Fig. 3.15a versus annealing temperature. While the adsorbed fraction n_{ads} does not depend on temperature and shows reversibility at the heating/cooling cycles, the structural fraction n_{str} evidences a quasi-reversible process (on the experiment timescale) and decreases with temperature. This behaviour can be treated in framework of the equilibrium process (attainable during 4 hours annealing at constant temperature), which kinetics equation can be presented as:

$$\frac{dn_{str}}{dt} = -k_1 n_{str} + k_2 (n_0 - n_{str}) \tag{3.3}$$

Where $k_1 = k_0 \cdot \exp(-E_a / k_B T)$ and k_2 are the water removal and restructuring constants, k_B is Boltzmann constant, E_a activation energy of water removal and $n_0 - n_{str}$ is the empty sites capable receiving water molecules. The solution of (3.3) can be presented as

$\ln\left(\frac{n_0}{n_{str}}-1\right)=const-E_a/kT$, which permits to obtain activation energy E_a=22±5 kJ/mol from experimental data in Fig. 3.15b.

An increase of the annealing temperature activates the diffusive mass transport in UPA, which leads to the material densification due to morphological changes in nanofibrils and beginning of nucleation of new crystalline phases inside and at the surface of the amorphous structures. The isochronous annealing during 4 hours with temperatures from 100 to 1650 °C does not destroy the structural rigidity of UPA samples while their macroscopic size decreases and mass density increases, as confirmed by the experimental data in Fig. 3.16.

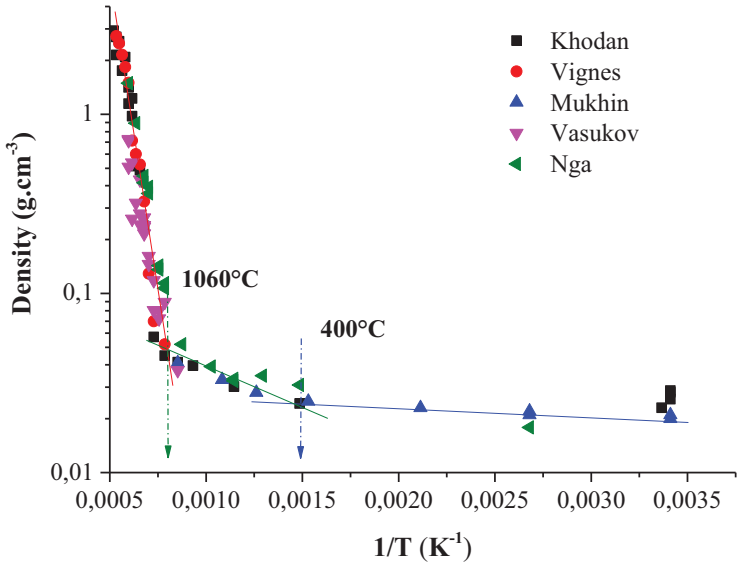

Figure 3.16: Density of UPA as a function of the annealing temperature (isochronous annealing time 4 hours). The different series of measurements are indicated with different markers ●, ■, ▼ and ▲ (Ref. [Mukhin 2012]).

3.3.3. Intermediate metastable phases and structural and chemical state

The relatively stable phase structures can be identified in UPA during annealing in the temperature range between 20 and 1650 ºC:

(I) The UPA structure synthesised in ambient air with relative humidity ~ 80 % at 25 ºC has the chemical composition $Al_2O_3 \cdot nH_2O$ with $n \geq 3$. The nuclear magnetic resonance (NMR) studies have shown that Al^{+3} cations have anionic surroundings including octahedral (83 %), pentahedral (16 %) and tetrahedral (1 %) [Frappart 2000]. Consequently the supramolecular

structure consists of polynuclear aqua-hydroxide complexes of aluminum cation and molecular water connected with hydrogen bonds in different spatial alignments.

(II) The native supramolecular structure of UPA losses water and decompose being heated to moderate temperatures of ~ 100 °C. It progressively becomes an amorphous oxide with composition $Al_2O_3 \cdot nH_2O$ with $n \leq 1.5$. An increase of temperature beyond 100 °C does not introduce significant changes of the amorphous structure, while the structural water content continuously reduces until $n \approx 0.1$ at 450-500 °C.

(III) At temperatures ~ 450 °C the crystallization of an amorphous Al_2O_3 into γ phase can begin, which remains a small amount of structural water $n < 0.1$. This small amount of water may be necessary for the transition phase stabilization [McHale 1997, Mukhin 2012] However, in nanofibrous alumina the crystallization is delayed to 870 °C [Vignes 1997]. The nanofibrous alumina remains in the amorphous state in the extended temperature range between 100 and 800 °C and convert to γ-Al_2O_3 at 870 °C.

(IV) After 4 hours annealing at temperatures $T \geq 1000$ °C, γ-Al_2O_3 converts to θ-Al_2O_3, which is accompanied by a further reduction of the structural water content to $n < 0.04$.

(V) The temperature increase to 1200 °C leads to the formation of well-crystallized stable α-Al_2O_3 polymorph, which does not contain any appreciable amount of structural water. This phase transition is completed at 1250 °C with the annealing time of 4 hours.

The main changes of the nanofibrous UPA materials microstructure during annealing related to the chemical composition and structural and phase can be described in the framework of the structural model described in the next part.

3.4. Conclusion

In this Chapter 3, an analysis of principal impurities and their influence on the growth kinetics using technical, high-purity and monocrystalline aluminum was performed. The growth of alumina monolith was found to depend on impurities in the original metals, which higher purity provided faster growth and bigger monoliths at the end. Based on these measurements, we can conclude about partial elements filtering by the Hg-Ag amalgam during the growth process for Si, Fe, Cu, Mn, Ti and Mg, while almost no or little filtering affects Ga and Ag elements. Hg may be entrained into UPA from the amalgam during the growth process, however can be easily removed at the thermal post-treatment stage.

We studied chemical, structural and phase transformations of pure UPA during thermal treatment in the temperature range between 20 and 1650 °C. The annealing results in

appreciable structural modifications of UPA materials. The size of elementary structural fibril, specific surface area, mass density and content of structural, adsorbed water and crystalline phase were measured as a function of the annealing temperature. Two kinds of adsorbed and structural water were distinguished and quantified. While the content of adsorbed water (~0.6 molecules per Al atom) in pure UPA depends on the specific surface area and does not appreciably vary below 1000 °C, the content of the structural water strongly decreases from ~3 molecules per Al atom at room temperature to 0.04 at the crystallisation onset temperature of 870 °C (γ-Al_2O_3). The activation energy 22±5 kJ/mol was obtained from experimental data.

Chapter 4
Silica modified alumina

In this Chapter, we study morphological and phase transformations of modified UPA by impregnation of trimethylethoxysilane (TMES) and tetraethoxysilane (TEOS). This assumes that the coverage of the heat-treated UPA nanofibrils with a thin layer of silica results in a substantial change in the surface energy that shifts the γ, θ and α phase transitions to higher temperatures. The silica layer can additionally preserve structural water from escaping that slows down the UPA phase transformation kinetics. The characterization of the silica-treated UPA composites is summarised. Besides of that, the treated-thermal UPA composites at high temperature above 1400 °C become mullite, which appearance and correlated structural and optical properties will be reported.

4.1. Synthesis

4.1.1. Chemical treatment

The UPA monoliths were grown by the method described in Chapter 3. The silica insertion into UPA monoliths was achieved by the vapor impregnation of a silica precursor compounds, trimethylethoxysilane (TMES: $(CH_3)_3$-Si-C_2H_5O) or tetraethoxysilane (TEOS: $Si(OC_2H_5)_4$), which both are volatile at room temperature. The difference between these two compounds is that TMES possesses one condensable hydroxyl thus forming the monolayer coverage of the UPA nanofibrils surface, while TEOS possesses four hydroxyl groups permitted the multilayer coverage. After heating at modetate temperatures ~200 °C, these adsorbed molecules convert into silica that covers the nanofibrils surface. TMES and TEOS under the impregnation saturation permit to introduce about 6 mol.% and 25 mol.% of silica into UPA.

The impregnation was performed in a way depicted in Figure 4.1. The raw alumina was inset into a vacuum vessel together with 5 mL TMES (or TEOS) liquid of 98 % purity, which was contained in a glass disk. In a short time, the steam of TMES (or TEOS) was saturated in the vase (Fig. 4.1). The porosity of the monolith (> 99 %) enables the vapor molecules to enter the structure. Then the molecules react with surface hydroxyls (alcoxolation reaction) of the alumina nanofibrils. In particular, the C_2H_5O group reacted with OH or water molecules leaving ethanol molecule; alternately, the $(CH_3)_3$-Si- group links with the fibers of alumina monolith.

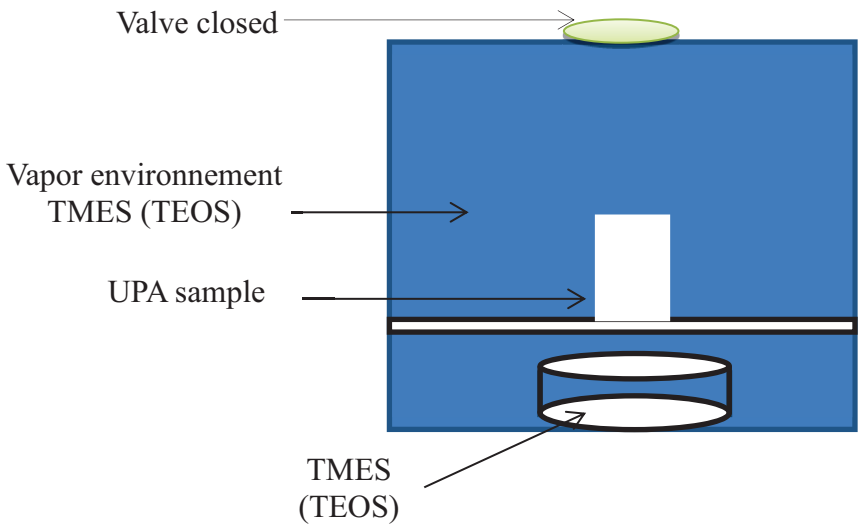

Figure 4.1: The process impregnation TMES (or TEOS).

This treatment with TMES extends overnight. In case of TEOS, the process occurred more slowly and the impregnation typically lasts more than a day. The treated UPA monoliths were then placed in an oven exposed to different temperatures in order to produce the material for further characterization.

4.1.2. Thermal treatment

The morphology, chemical composition and crystalline structure of the modified UPA monolith changed depending on temperature. The monoliths are dehydrated, passed to an amorphous structure and then crystallized to transition γ and θ phases and finally, to the stable α phase.

The heat treatments are performed in an electric furnace and are divided into three stages schematically depicted below. A first stage, the temperature rises with a speed of 200 °C/hour until the desired annealing temperature. And a second step is holding temperature during annealing time (chosen typically 4 hours). Finally, it is a cool-down step which corresponds to the cooling of the sample to room temperature.

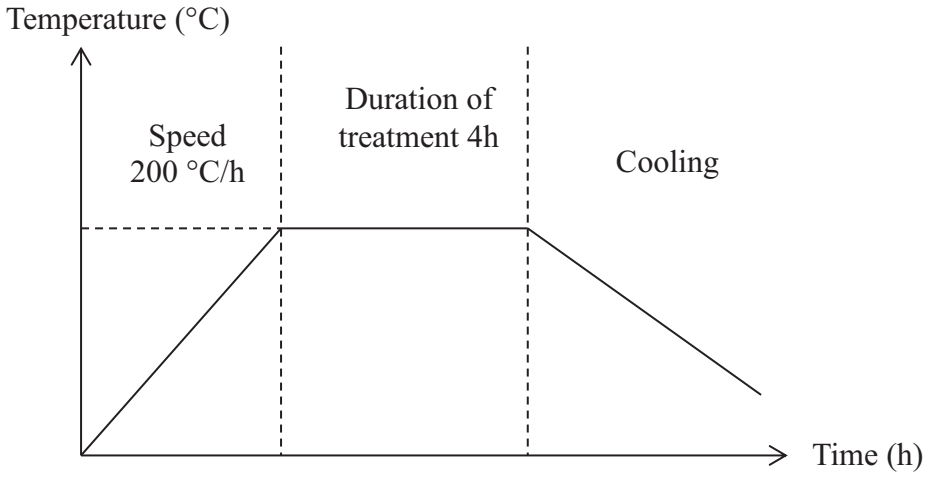

Figure 4.2: The thermal treatment process.

4.2. Structural, chemical and phase modification of UPA treated TMES

4.2.1. Effect of annealing on the structure composite

The mass modification of alumina (UPA+TMES) increased about 6 wt.% after the impregnation of trimethylethoxysilane (TMES). After annealing, the organic groups of TMES decompose carrying out ~50 % of mass. Consequently the final silica-modified UPA composite contains 5-6 mol.% of SiO_2 forming a monolayer on the raw material surface with high specific area ~300 m²/g. In heat-treated materials the specific area decreases, especially stronger above 1000 °C. In these conditions, the silica layer thickens and/or diffuses into the bulk of alumina fibers for mins mixed phases (ultimately, mullite).

These two images in Figure 4.3 show the SEM microstructure of UPA annealed at 1400 °C in 4 hours without (a) and after (b) TMES impregnation.

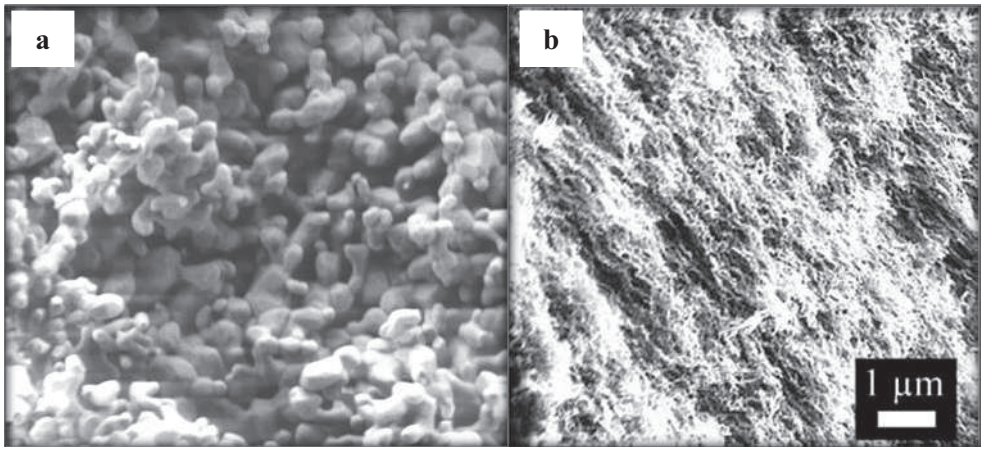

Figure 4.3: SEM images: (a) UPA, (b) UPA+TMES.

The effect of TMES treatment on the structure of UPA is clearly seen in these images. The presence of thin SiO_2 layer, covering homogeneously the surface of nanofibrils evidently slows down their morphological modifications by preserves thickening. This is apparently related to the surface mass transport (as will be shown in theoretical model presented in Chapter 5). The presence of amorphous SiO_2 layer limits the loss of structural water from alumina and limits diffusional mobility of alumina across the fiber surface. The measured changes of the fibril diameter after annealing with temperatures varying from 300 to 1600 °C during 4 hours are shown in Fig. 4.4.

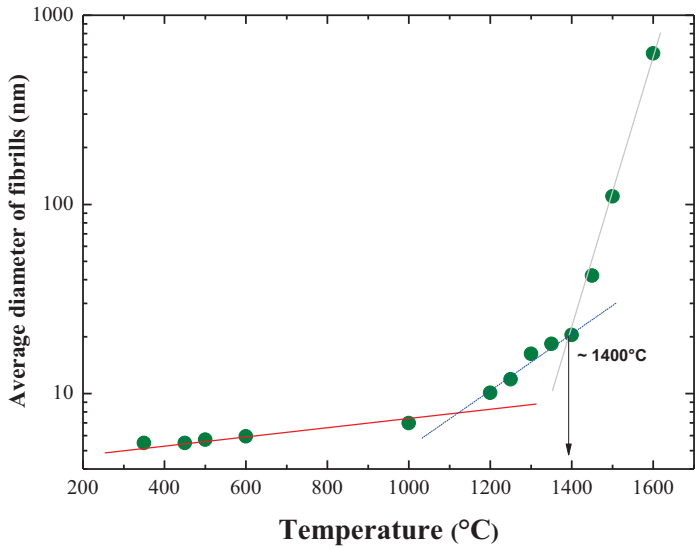

Figure 4.4: Mean diameter of fibrils versus treatment temperatures annealing during 4 hours.

4.2.2. Effect of annealing on chemical and structural transformations

Along with the morphological modifications, the phase transformation of UPA+TMES following annealing temperature from 100 to 1600 °C (4 hours) was characterized by X-ray diffraction as shown in Figure 4.5 and the results are summarized in Table 4.1.

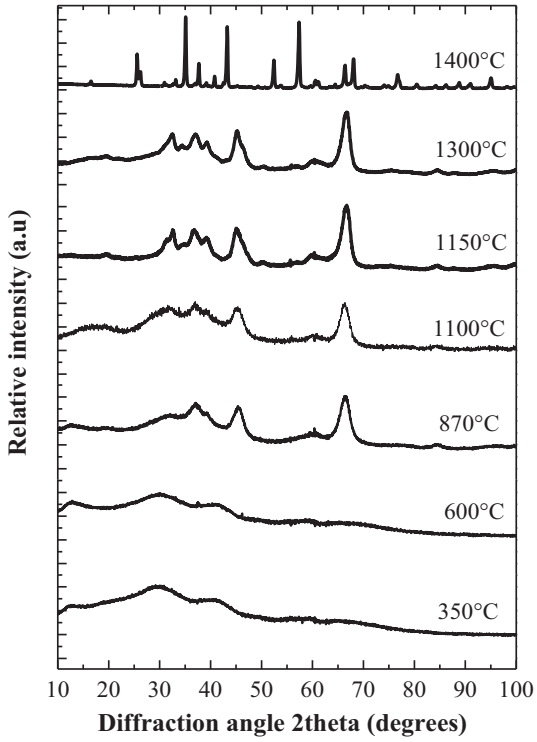

Figure 4.5: XRD of UPA+TMES at different temperature in 4h.

Table 4.1: Phase transition of UPA+TMES

Phase transition		Temperature, ºC	
		UPA	UPA+TMES
I-II	Supramolecular → amorphous	<100	<100
II-III	Amorphous → γ-Al_2O_3	870	870
III-IV	γ-Al_2O_3 → θ-Al_2O_3	~1000	~1150
IV-V	θ-Al_2O_3 → α-Al_2O_3	~1200	1400

The crystallization of UPA+TMES occurred at ~870 °C with the γ phase appearance, which is similar to that of pure UPA. However, at 1150 °C UPA+TMES transforms in θ phase and maintains it up to quite large temperatures of 1400 °C, when alpha phase becomes to appear. In contrast, the γ-Al_2O_3 → θ-Al_2O_3 and θ-Al_2O_3 → α-Al_2O_3 transition temperatures are considerably lower in pure UPA.

The effect of SiO_2 on the phase transitions can be seen though a comparison between X-ray diffraction patterns of pure UPA and UPA+TMES. Below in Figure 4.6, two such patterns are shown for the materials annealed at 1400 °C during 4 hours. The silica-treated samples show larger width of peaks, which evidences the smaller size of just nucleated α-phase crystallites.

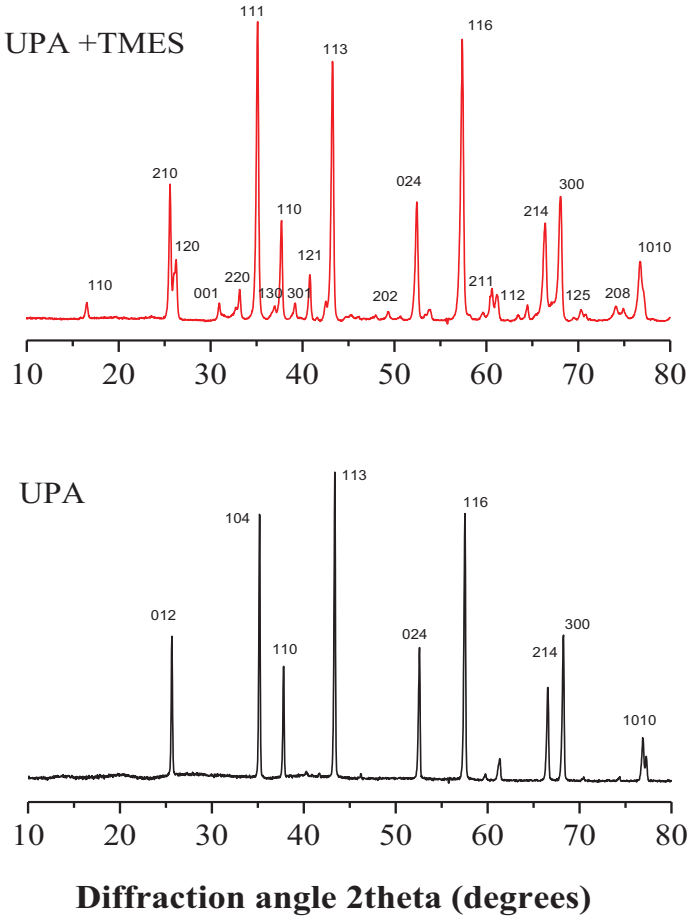

Figure 4.6: XRD patterns of UPA and UPA+TMES samples treated at 1400 °C for 4 hours.

Similar to the pure UPA, the modification of the chemical composition involves a mass loss of the adsorbed and structural water. The mass losses in raw and thermally treated UPA samples in the temperature range 25-950 °C obtained from TG measurements are presented in Fig. 4.7.

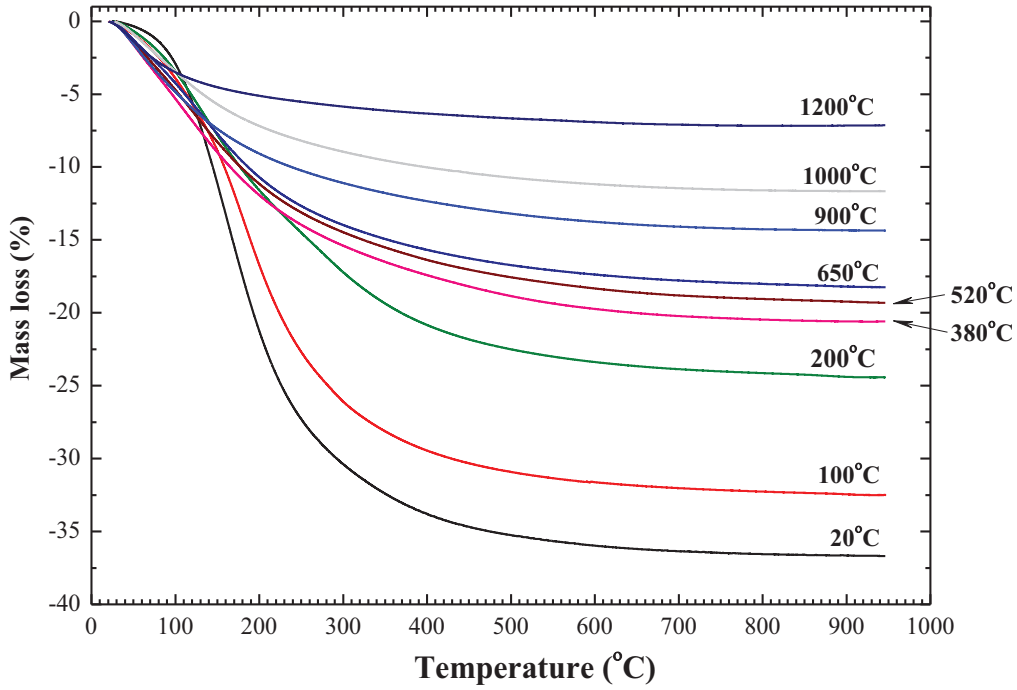

Figure 4.7: Thermal mass loss after annealing in air in raw (20 °C) and pre-treated (100-1200 °C) UPA+TMES samples.

Because of a low amount of silica in UPA (5-6 mol.%) and only ~50 % mass loss at the TMES to SiO_2 molecular transformation, we can neglect it in the total mass loss of the composite material. Therefore, the total mass loss can be attributed to the adsorbed and structural water, as in the pure UPA (see Chapter 3). From the measured mass loss in Fig. 4.7 and using formulas (3.1) and (3.2) of Chapter 3, we can obtain the relative numbers H_2O per Al of both adsorbed and structural water in UPA+TMES. These values are presented in Table 4.2.

Table 4.2: Relative water content in UPA+TMES samples: $Al_2O_3 \cdot nH_2O$ ($n = n_{str} + n_{ads}$)

molar ratio H_2O/Al_2O_3	annealing temperature °C				
	100	200	380	520	650
total water, n	3.24	2.43	2.06	1.92	1.81
adsorbed water, n_{ads}	0.05	1.12	1.51	1.58	1.55
structural water, n_{str}	3.19	1.31	0.55	0.34	0.26

The results in Table 4.2 show that while the adsorbed water content does almost not change with temperature below 650 °C that of the structural water decreases. However, this decrease is substantially slower compared to that in pure UPA (see Table 3.11 of Chapter 3): e.g. at it is almost 3 times lower at temperatures 300-650 °C. We conclude that the silica layer effectively protects the structural water molecules from leaving the structure.

The isochronous annealing during 4 hours with temperatures in the range from 100 to 1600 °C does not destroy the structural rigidity of UPA+TMES samples like that of pure UPA whilst mass density increases as confirmed by the experimental data in Figure 4.8.

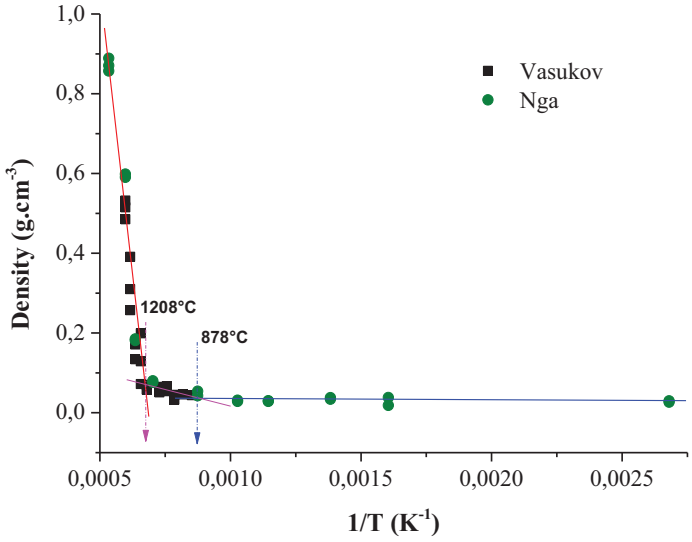

Figure 4.8: Mass density of UPA+TMES after annealing (for 4 hours) at different temperatures.

As correlating with mass density, the specific area of UPA+TMES is the function of the annealing temperature and decreases with its increase. The measured BET data in UPA+TMES together with those of pure UPA (for a comparison) are shown in Figure 4.9. One can see that the specific surface of UPA+TMES is significantly higher. The effect of silica is especially strong at temperatures between 1000 and 1500 °C. For example, the specific area at 1000 °C is 204 m^2/g in UPA+TMES and 170 m^2/g in UPA while this difference increases to more than 11 times between 1300 °C and 1500 °C and disappears above 1600 °C when both materials behave quite similarly.

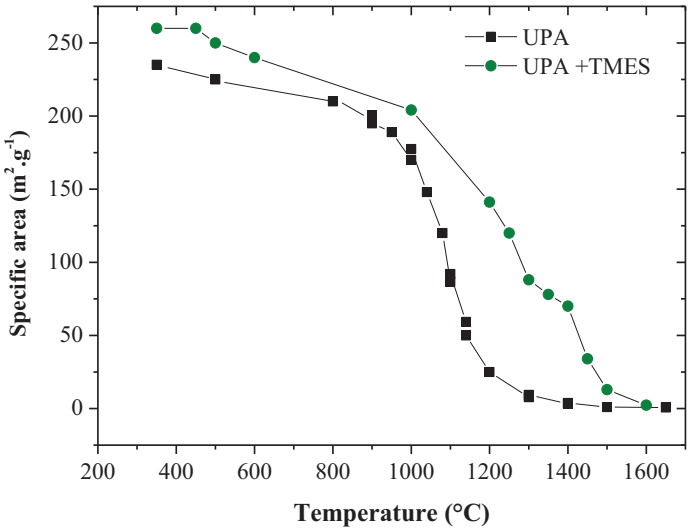

Figure 4.9: Specific area of pure UPA and UPA+TMES at different temperature annealing in 4 h.

4.2.3. Intermediate metastable phases and structural and chemical state

Below we summarise changes of chemical composition, morphology and phase of UPA+TMES at isochronous annealing for 4 hours:

(I) Material has an ultraporous structure with chemical composition $Al_2O_3.nH_2O$ (n≈3.6). After TMES treatment, the composition is changed to $Al_2O_3.nH_2O + SiO_2$ at low temperature with almost the same n.

(II) The water losses appear at temperatures ~100 °C when the material becomes amorphous with composition $Al_2O_3.nH_2O + SiO_2$ with n=2.4. The increasing of temperature beyond 100 °C does not change dramatically the material structure but the structural water decreases to n<0.3 at 650 °C.

(III) At higher temperatures above 870 °C, the material crystallises into γ phase.

(IV) After annealing at temperature 1150 °C the material transfers to θ phase.

(V) The temperature as high as 1400 °C, the material becomes stable α phase (corundum).

4.3. Structural, chemical and phase modification of UPA treated TEOS

4.3.1. Effect of treated silica and annealing temperature on the structural

Different compared to using TMES, TEOS permits a high amount of silica to be introduced in ultraporous alumina. The impregnation elemental kinetics expressed in Si mol.% into raw UPA matrixes by using TEOS vapor at room temperature is shown in Fig. 4.10. The deposition process runs effectively at early times below 12 hours saturates after 50 hours resulting in the molar ration Si/Al≈25 %. This grafted TEOS molecule disposes four hydroxyl groups permitting condensation of many molecular layers. However, the process terminates and its saturation may be related to the condensation between two hydroxyls of grafted TEOS molecules.

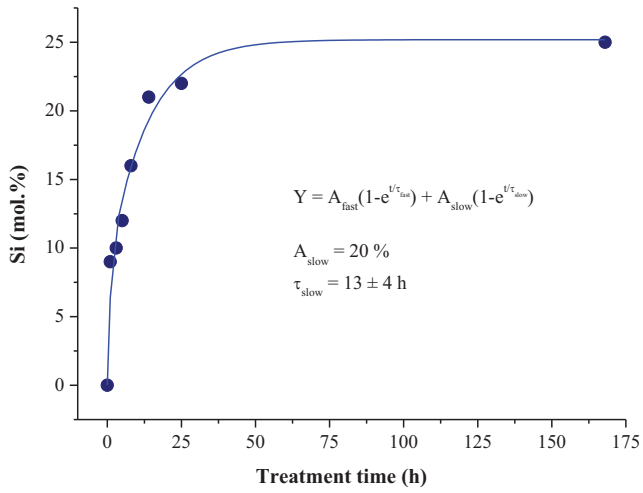

Figure 4.10: Si molar content at TEOS vapor impregnation at 20 °C into pure UPA versus time.

In general case, the fitting of surface sites can be represented by the expression:

$$N = \sum_{i=0,1,2,...} A_i e^{-t/\tau_i} \tag{4.1}$$

Where A_i and τ_i are number densities and deposition time constant of the *i*-th site. Since the fit of the experimental points by Equation (4.1) with *i*=1 was not satisfactory, we concluded that at least two different sites receive the TEOS molecules. The fits of the experimental data with *i*=2 is presented in Fig. 4.10 by solid line. It shows that the short-lived exponents with t<1 h (not resolved) accounts for Si/Al≈5 % and the dominant long-lived exponent has characteristic deposition time of τ≈13 h. We tentatively attribute the fast component to the TEOS condensation with surface hydroxyls of raw UPA and the slow one to the condensation between grafted and free TEOS molecules.

The TEM images in Figure 4.11 show the local microstructure and its electron diffraction pattern of heat-treated (1400 °C for 4 hours) UPA monoliths after TEOS impregnation, which confirm crystallization.

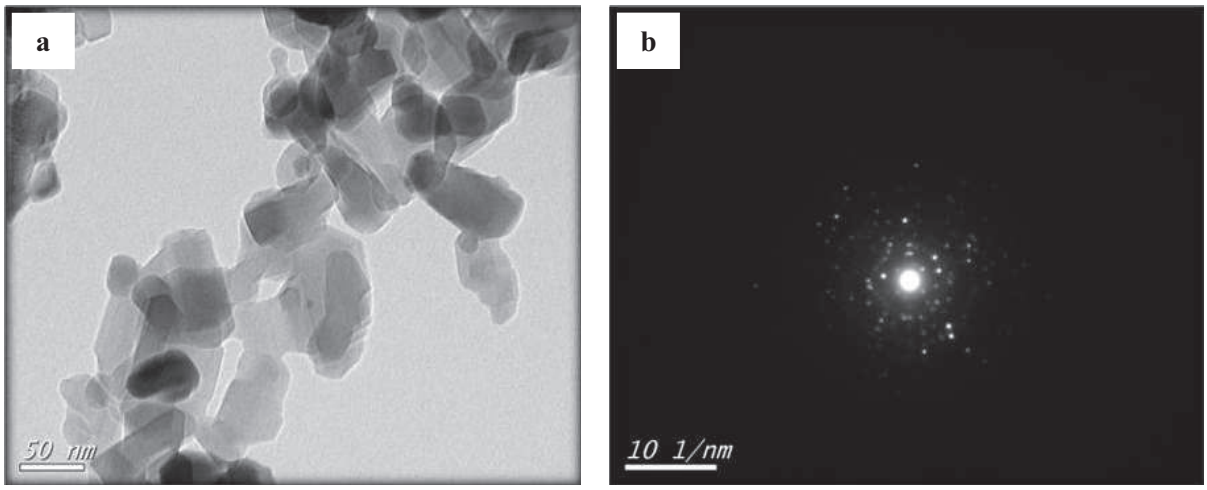

Figure 4.11: TEM and electron diffraction images of UPA+TEOS (25 mol.%) annealed at 1400 °C for 4 hours.

The comparison of two X-ray diffraction patterns of pure and TEOS treated UPA and annealed at 1400 °C for 4 hours are shown in Figure 4.12. In absence of silica, to pure α-phase alumina has been observed, which progressively transforms to mullite phase at the silica content and temperature increase, as it will be discussed in the following chapters.

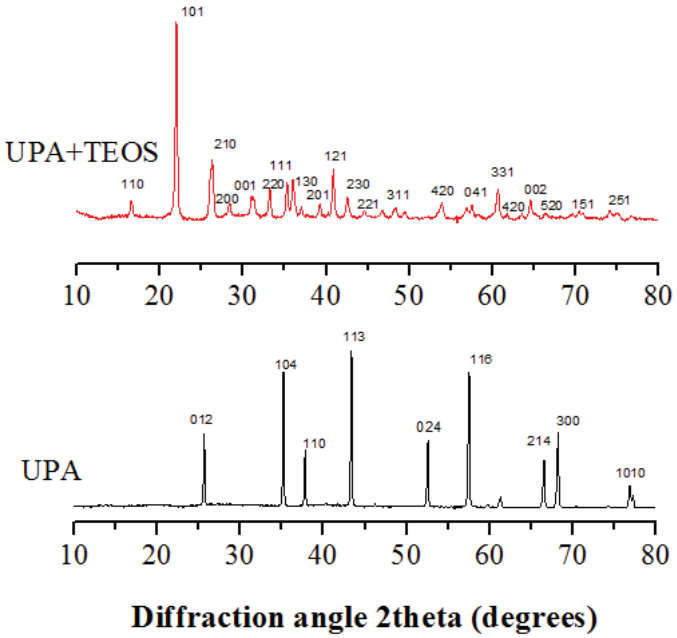

Figure 4.12: XRD of UPA and UPA+TEOS annealed at 1400 °C for 4 hours.

The average diameter of UPA fibrils after TEOS impregnation is shown in Figure 4.13 versus annealing temperature. While the diameter evolution below 1000 °C is comparable with that of pure UPA (Figure 3.12 of Chapter 3) and UPA+TMES (Figure 4.4 of this Chapter 4), the difference with these two materials at higher temperature is significant. A thick silica layer strongly limits the fiber coarsening kinetics: as a consequence of that, the mean diameter at 1400 °C attains ~30 nm versus ~200-300 nm of pure UPA and UPA+TMES.

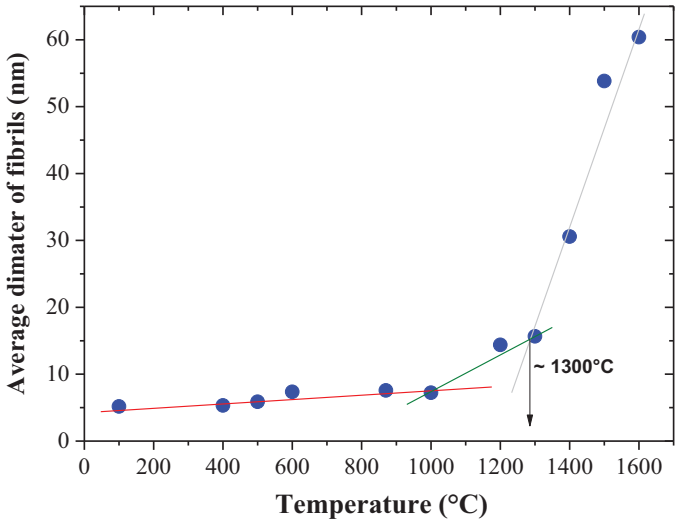

Figure 4.13: Mean diameter of fibrils estimate versus treatment temperature annealing during 4 hours.

4.3.2. Effect of annealing on chemical and structural transformations

These phase transformations of UPA+TEOS during annealing at temperatures between 100 and 1400 °C for 4 hours are presented in Table 4.3 and X-ray diffraction patterns in Figure 4.14.

Table 4.3: Phase transformations of UPA and UPA+TEOS after 4h annealing

Phase transition		Temperature, ºC	
		UPA	UPA+TEOS
I-II	Supramolecular → amorphous	<100	100
II-III	Amorphous → γ-Al_2O_3	<870	1000
III-IV	γ-Al_2O_3 → θ-Al_2O_3	~1000	1200
IV-V	θ-Al_2O_3 → α-Al_2O_3 / mullite	~1200	1300

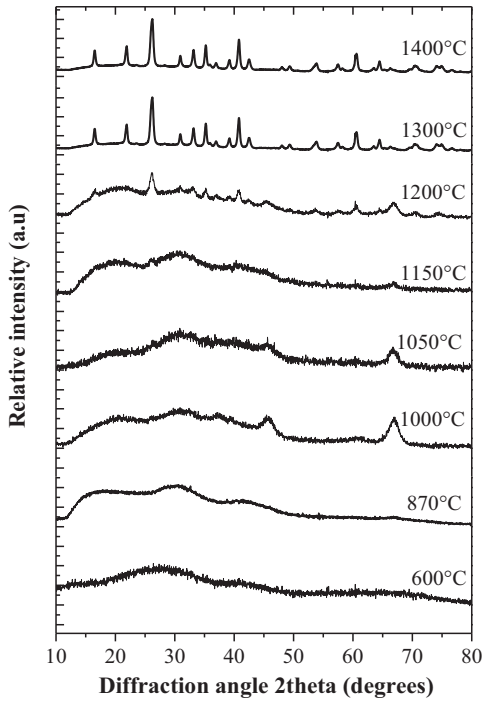

Figure 4.14: X-ray diffraction patterns of UPA+TEOS after isochronous annealing during 4 hours.

Like that pure UPA and UPA+TMES materials, at low annealing temperature the composite UPA+TEOS still exist at an amorphous state. Above 1000 °C γ phase nucleates, which is ~230 °C higher than the crystallization onset of UPA and UPA+TMES. The θ phase and mullite appear after 4 h annealing respectively at 1200 and 1300 °C.

To compare the pure mass loss of the silica precursor compounds, we performed mass loss measurements of γ-phase UPA (in which, according to our previous measurements, the structural water content is below 0.1 mol.% and reversible ware losses are known) after the impregnation with 7 mol.% of TMES or TEOS vapor. Thus, the mass loss of this composite can be related to the TMES and TEOS transformations to silica. The results of TG measurements are shown in Figure 4.15.

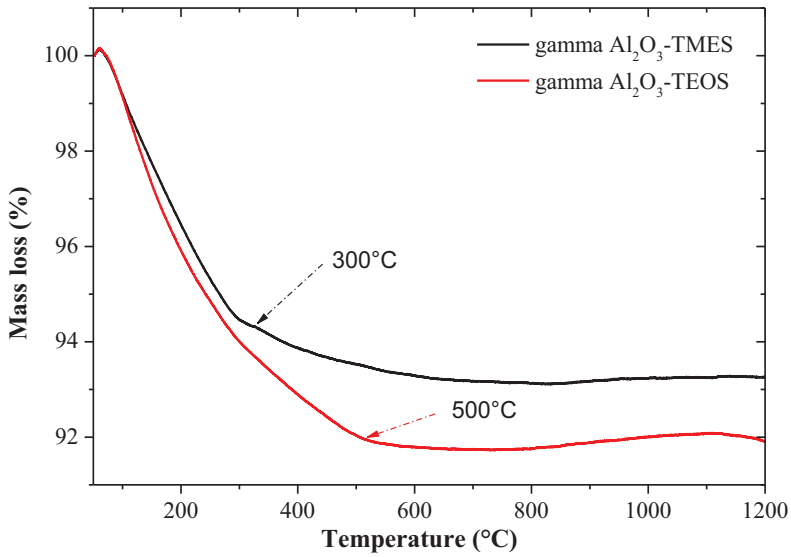

Figure 4.15: The mass loss of γ-UPA treated with 7 mol.% TMES or TEOS vapor.

These results show that γ-Al_2O_3 impregnated with TMES loses 5.5 % of total mass and this process is almost terminates at 300 °C while γ-Al_2O_3 impregnated with TEOS loses 8 % of total mass and this process terminates at 500 °C.

The experimental data of the mass density increase in the temperature range between 100 and 1400 °C for UPA+TEOS samples are shown in Figure 4.16.

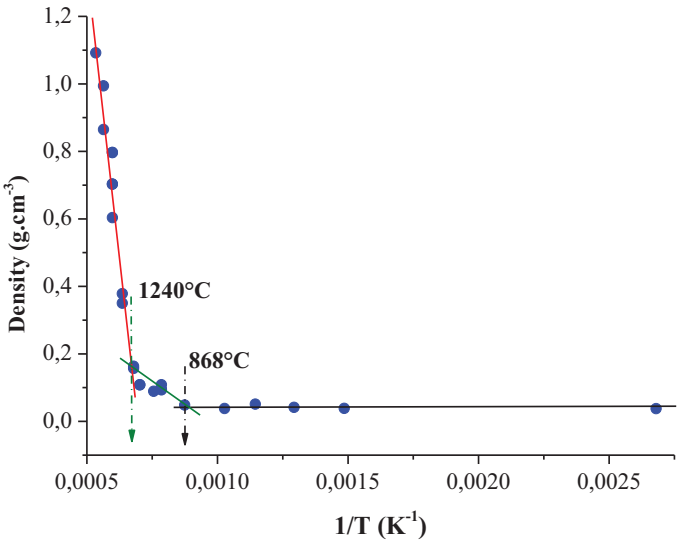

Figure 4.16: Mass density of UPA+TEOS after isochronous annealing during 4 hours.

The UPA+TEOS mass density variation with temperature shows two inflection points at ~870 and ~1240 °C, which respectively corresponds to the γ and α phase appearance, similar to that observed in UPA+TMES.

The specific area of UPA+TEOS material decreases when the annealing temperature increases. These results as well as those obtained with pure UPA and UPA+TMES are shown in Figure 4.17.

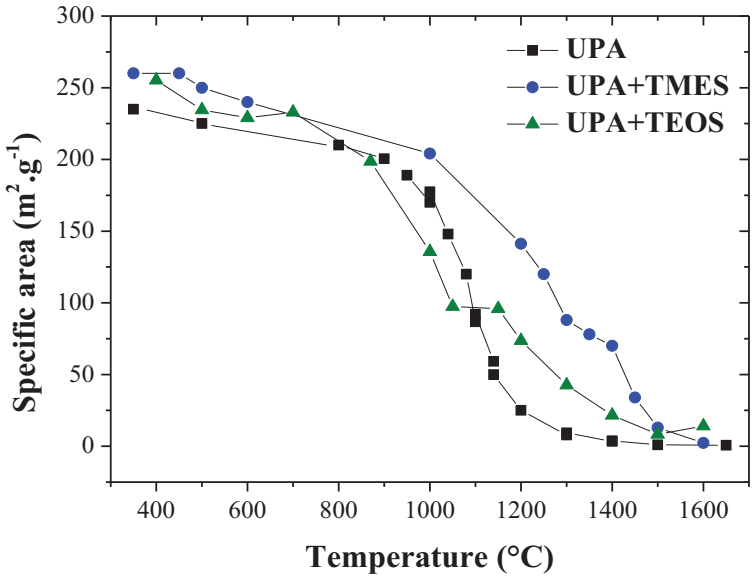

Figure 4.17: Specific area of UPA, UPA+TMES and UPA+ TEOS versus annealing temperature.

The specific surface area variation with temperature for all three materials is quite similar at temperatures below 1000 °C and above 1500 °C. In between these two points, the specific surface area of UPA+TEOS is higher than UPA but smaller than UPA+TMES.

4.3.3. Mullite

The structure of mullite is formed with the annealing temperatures of 1400 °C and higher of UPA+TEOS samples, although traces of mullite under this annealing have being also observed in UPA+TMES. To investigate the effect of the annealing duration on the mullite formation, we carried out a series of the material preparation at 1400 °C and different durations of 4 h, 10 h, 18 h, 24 h, 36 h, 48 h and 72 h. The morphological modifications and electron diffraction patterns proving the appearance of mullite are shown in some selected pictures of Figure 4.18.

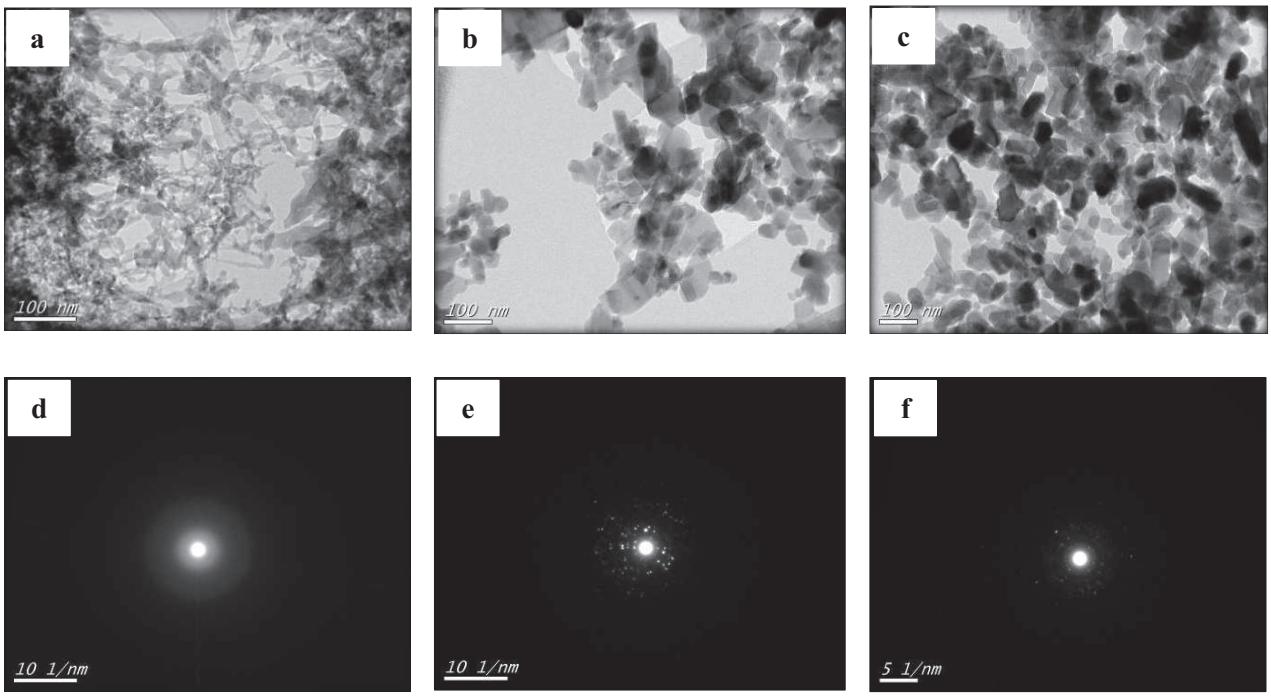

Figure 4.18: (a, d) UPA+TEOS (25 mol.%) at room temperature, (b, e) Mullite annealed at 1400 °C in 10 h, (c, f) Mullite annealed at 1400 °C in 72 h.

At room temperature, the TEOS treated UPA exists in the amorphous state similar to pure UPA and the diameter and the density of nanofibrils does not significantly increase by the SiO_2 impregnation. In the material heat-treated at 1400 °C, the mullite crystalline structure is

formed accompanied by an increase of the fibrils diameter and mass density. These results are presented in Figure 4.19.

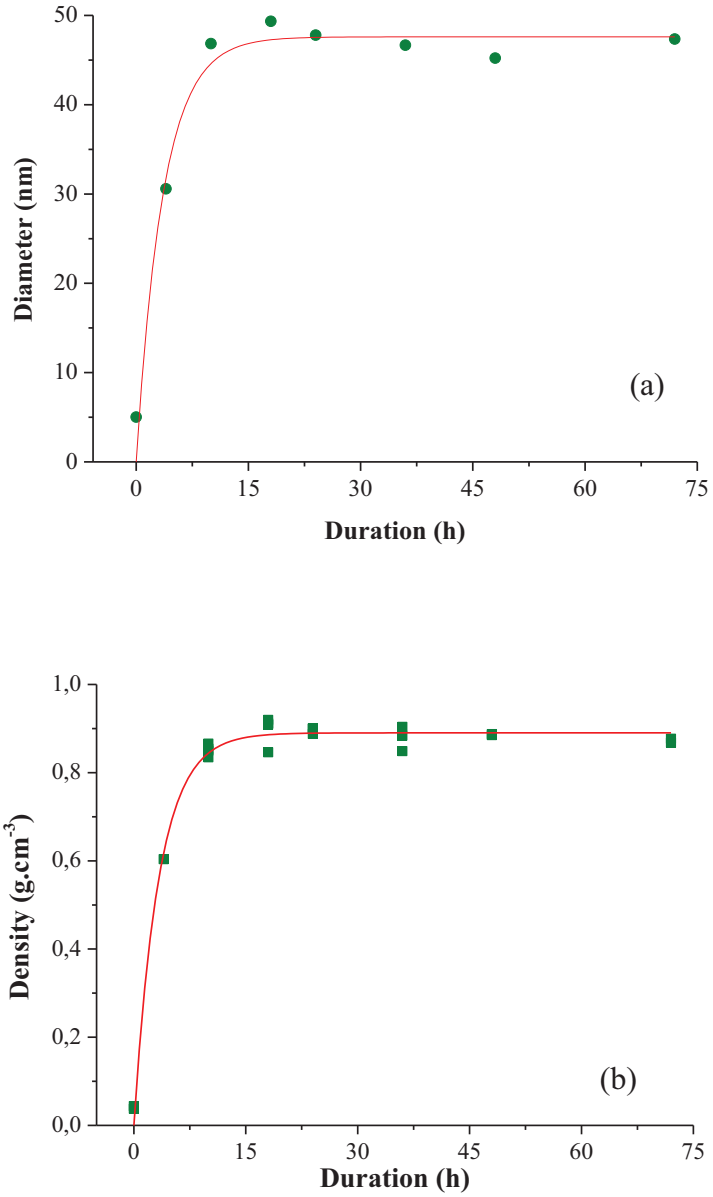

Figure 4.19: Diameter (a) and mass density (b) of mullite at 1400 °C with different durations annealing.

The diameter and density of mullite are function of time durations, they were fitted by function: $y = a(1\text{-}e^{-b\tau})$, where, a is the scaling factor and b is slope factor. After 18 h annealing the mean fibril diameter is 48 nm and the material mass density 0.89 $g.cm^{-3}$ with the quite similar slope parameters of 0.29±0.01.

The temperature of the mullite appears respectively α phase Al_2O_3 and the transformed mullite content is expected to depend on Si loading. In order to investigate this effect, we have performed a series of X-ray diffraction measurements of samples prepared with different quantity of Si shown in Figure 4.20. The relative intensities of the mullite (120) and (210) and α-Al_2O_3 (012) peaks were analyzed. As the results show, the mullite peaks intensity raises sharply when Si content increases above 12.5 mol.%. The main conclusion is that the both α-Al_2O_3 and mullite phases coexist at the Si content below 20 mol.%. Above this point, the material is of the pure mullite phase. We tentatively assign the synthesized mullite to the alumina-rich 2:1 ($2Al_2O_3 \cdot SiO_2$) phase.

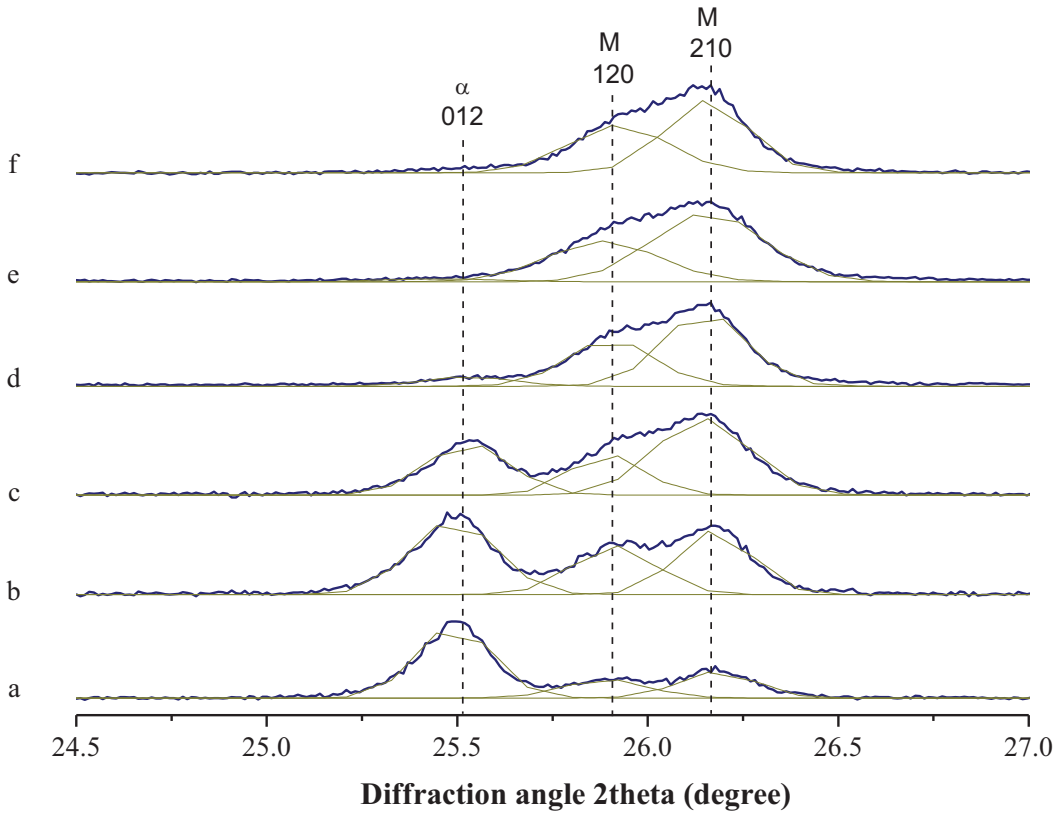

Figure 4.20: Evolution of 012 (α) and 120 / 210 (mullite) crystallographic peak intensities ($\lambda_{CuK\alpha}$=1.5418 Å) as a function of TEOS impregnation time 1 h (a), 5 h (b), 7 h (c), 8 h (d), 14 h (e) and 168 h (f). Thermal treatment was conducted at 1400 °C during 18 h.

4.4. Optical properties

4.4.1. TMES treated alumina

After 4 hours annealing at 1400 °C, UPA+TMES sample is composed of two kinds of nanoparticles with the mean diameter about 15 and 50 nm as shown in SEM images of Figure 4.21 (a, c). The thick circles in the diffraction image confirm arbitrary mutual orientations of the small nanoparticles. After the prolonged annealing during 18 hours, the particles coarsen up to 100 nm size while the thin nanoparticles disappear.

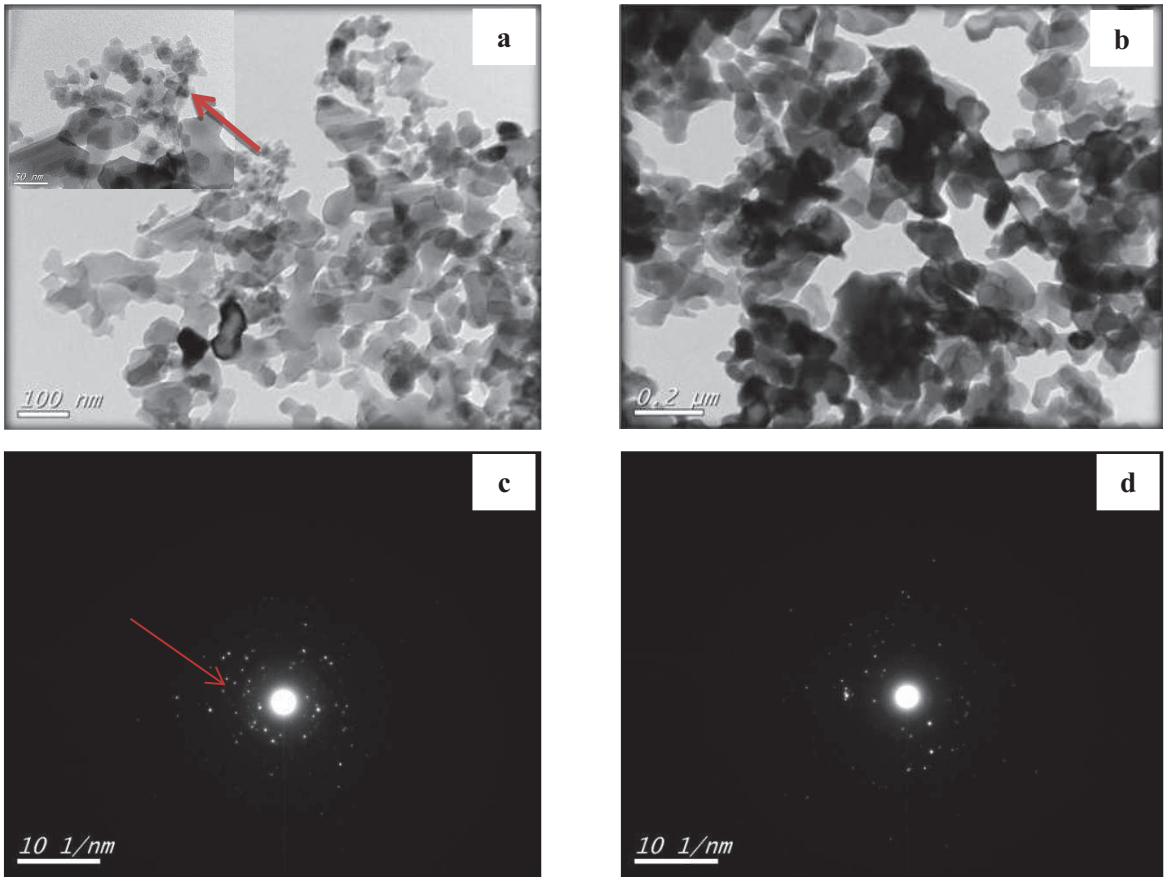

Figure 4.21: TEM images of UPA+TMES (5 mol.%) annealed at 1400 °C temperature in 4 h (a, c) and 18 h (b, d).

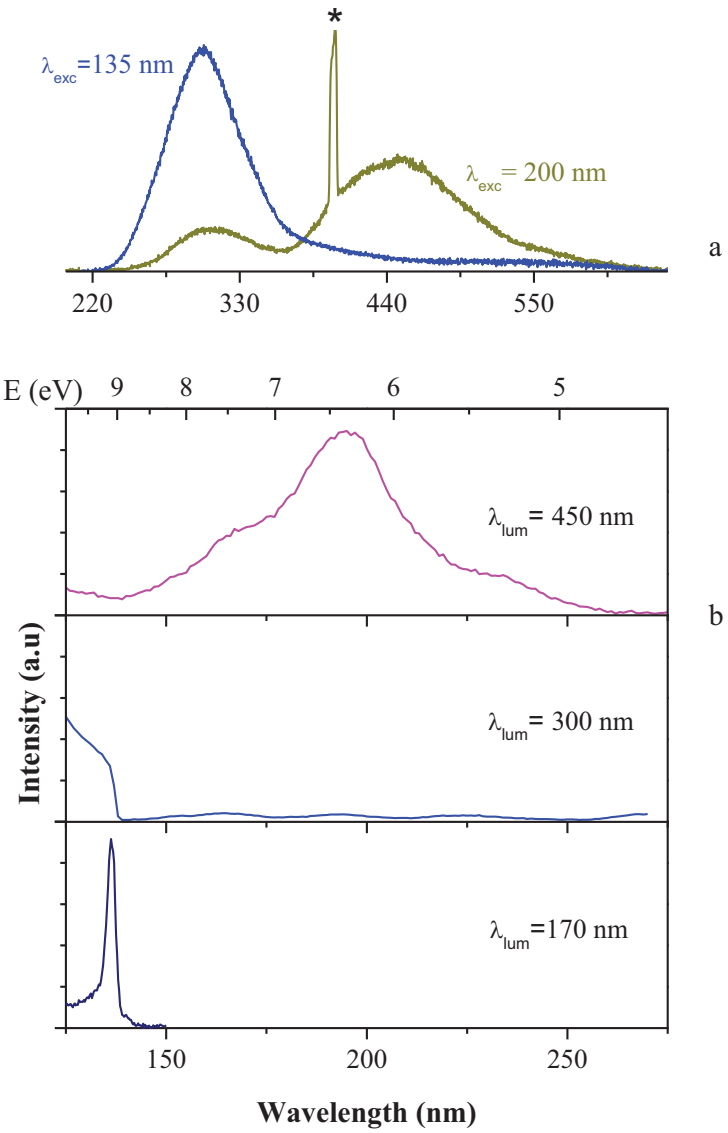

Figure 4.22: UV-visible luminescence spectra (a) and luminescence excitation spectra of different luminescence bands (b) of UPA+TMES. (*) denotes the second order of SR scattering (a).

The luminescence spectra of UPA impregnated with TMES until 5 mol.% Si and thermally treated at 1400 °C during 18 hours are shown in Figure 4.22 (a). Although little mullite is formed in these conditions (this formation also confirmed by TEM and diffraction images in Fig. 4.21 (a, c)), these spectra serve to be a reference point for the mullite formation series. The observed UV-visible band at 300 nm has been previously assigned to partially compensated anion vacancies, F^+ centres while the visible emission band at 450 nm has been assigned in nanosized alumina respectively to F centre formed by oxygen vacancies trapping one (F^+) and two (F) electrons [Valbis 1991]. Moreover, self-trapped excitons produced indirectly, e.g. by recombination of free and trapped charges, contribute to the UV emission. Besides the UV-visible bands shown in Figure 4.22 (a), a VUV band at 170 nm appears in the

luminescence spectra, which belongs to self-trapped excitons in α-Al_2O_3 [Kirm 1999]. The luminescence excitation spectra of the VUV, UV and visible emission bands are shown in Figure 4.22 (b). The first two clearly show a signature of the integrand transitions in the energy range above the fundamental absorption onset at 132.47 nm (E_g=9.36 eV), which is in agreement with literature data [Kirm 1999]. In contrast, the visible band excitation does not show up the interband transitions and is related to the defect structure of the material.

We remark that the VUV band (170 nm) strongly weakens compared to pure UPA(α), while the UV (300 nm) intensifies. The intensified component of the UV band has long decay time (≥1 μs). In the same time, the short-lived (nanosecond) component of the UV band weakens. In agreement with [Valbis 1991] and our recent analysis of pure UPA samples [Museur 2013] this short-lived component can be assigned to F^+ centres. It contributes to luminescence excitation spectrum with several symmetry-split absorption bands between 4 and 6 eV. Our measurements (Figure 4.22) show no appreciable excitation of the UV band at ~200 nm, which permits to assign the observed symmetrical shape UV emission exclusively to a self-trapped exciton. Because both VUV and UV bands belong to self-trapped excitons, one can suppose that the first one belongs to surface defect sites, which "healing" by silica promotes the exciton trapping at defect bulk sites emitting in UV spectral range.

4.4.2. TEOS treated alumina

The luminescence spectra of the annealed UPA+TEOS materials with different silica loadings controlled by the impregnated process duration are shown in Figure 4.23.

In these conditions, the both α-Al_2O_3 and mullite phases coexist. At excitation above the fundamental absorption onset of α-Al_2O_3, the VUV band (170 nm) disappears, while the UV (300 nm) weakens progressively with the Si addition. This emission disappears at the critical Si concentration C^*_{Si}≥16 mol.%. In agreement with our X-ray diffraction analysis, we relate this effect to the complete transformation of α-Al_2O_3 to mullite. The inspection of the near-IR spectral range shows another emission, which appears non-regularly in our UPA solids.

This near-IR luminescence also strongly intensifies after TMES impregnation, which suggest a similar mechanism to that leading of the UV band intensification. Accordingly, this luminescence comes from bulk sites, which are preferentially excited after silica deposition on the UPA surface. With more addition of Si (after TEOS impregnation) the near-IR band weakens however not disappears like the UV one. Moreover, its band shape modifies at Si impregnation during t≥8 h (see for a comparison Figure 4.23 (c) and (d)).

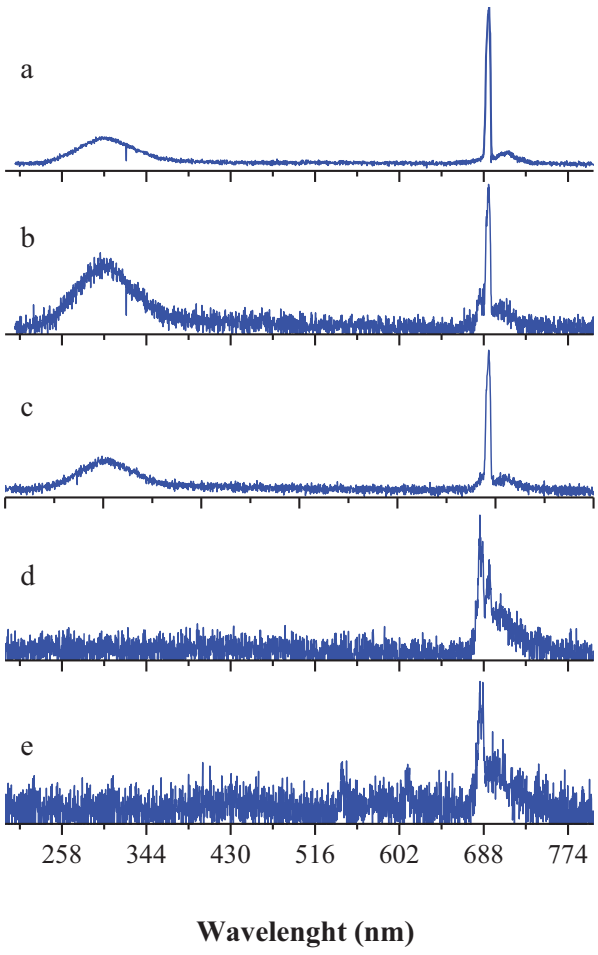

Figure 4.23: UV-visible luminescence spectra (λ_{exc}=130 nm) of TEOS-treated UPA during 1 h (a), 3 h (b), 5 h (c), 8 h (d) and 14 h (e). Thermal treatment was conducted at 1400 °C during 18 h.

Optical properties of oxide solids are influenced by metal ions, which can appear in quantities below 0.1 wt.%. Ions with an incomplete 3*d* shell (Ti^{3+}, Cr^{3+}, V^{3+}, Mn^{4+}, Fe^{3+}, Ni^{3+}) substitute for Al^{3+} ions in the α-Al_2O_3 lattice providing a strong absorption between 6 and 7 eV [Tippins 1970]. Because of a high sensitivity, the luminescence method is capable observing traces of metal ions [Gaft 2011]. The main impurities of our crystalline alumina are Si, S, K, Na, Fe, P and Ca, which all together amount for ~10^{-3} wt.%; the contamination by other impurities is below 10^{-4} wt.% [Scherban 2014]. In particularly, Cr is present at a very low level of below 10^{-5} wt.%. Despite of this low content, fluorescence methods permit to observe near-IR luminescence of Cr^{3+} ions at concentrations as low as 10^{-7} wt.% [Snytnikov 2005].

The transitional-metal ions Cr^{3+} preferentially occupy substitutional sites of octahedrally coordinated Al^{3+} (which is a case of both α-Al_2O_3 and mullite structures) and their luminescence spectra in this configuration depend on local crystalline field strength. The

radiative transitions originated from the same $^4A_2$ excited state terminate on the energetically lowest $^4T_2$ or ^2E states respectively in weak or strong field environments. The weak-field emission band due to the $^4T_2$-$^4A_2$ transition typically centres between 700 and 800 nm with a half-width-full maximum about 100 nm, while strong-field emission spectra show sharp R lines due to the ^2E-$^4A_2$ transition [Snytnikov 2005, Gaft 2012]. The spectral position of these lines sensitively depends on the environment. In particularly, when Al_2O_3 crystalline structure changes the doublet exhibits a shift [Wen 1998, Snytnikov 2005, Patra 2005, Pan 2008]. The lines vanish when crystalline structure is damaged [Pan 2008]. Their spectral position depends on Cr^{3+} concentration and red shifts with its increase [Patra 2005].

Our recorded IR luminescence spectra of both α-Al_2O_3 and mullite phases correspond to the strong-field environment of chromium ions. The high resolution spectra of UPA samples impregnated with TEOS during 1 and 8 hours, which according to Fig. 4.10 correspond to Si content of 6 and 16 mol.%, are shown in Fig.4.24.

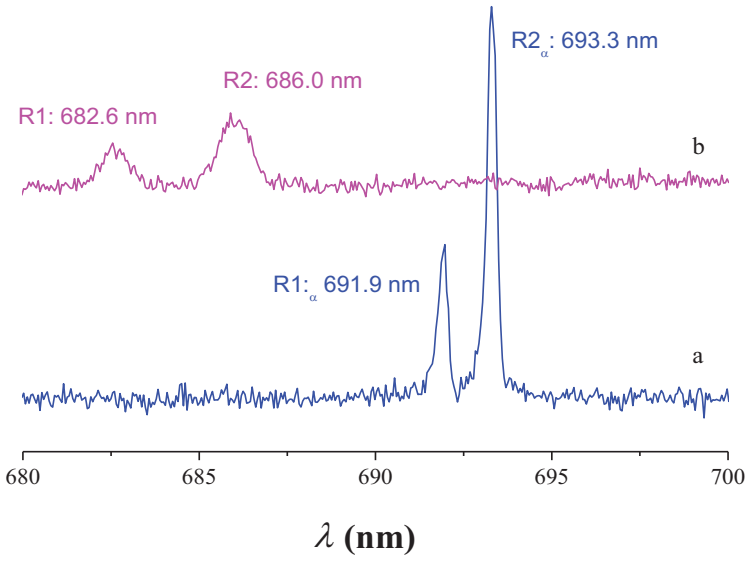

Figure 4.24: High-resolution near-IR luminescence spectra of TOES-treated ultraporous Al_2O_3 during 1 h (a) and 8 h (b). Thermal treatment was conducted at 1400 °C during 8 h.

At the lower Si content, the near-IR luminescence consists of two narrow peaks at 691.9 and 693.3 nm (a), while at the higher content, these lines disappear and other lines appear at 682.6 and 686.0 nm (b). According to previous studies [Wen 1998], these doublets can be assigned to zero-phonon lines (R lines) of ^2E_g-$^4A_{2g}$ transitions of Cr^{3+} in a strong crystal field. The doublet lines at 691.9 (R2) and 693.3 nm (R1) (Fig. 4.24 (a)) in samples with low Si content <16 mol.% are in an excellent agreements with Cr^{3+} transitions in α-Al_2O_3 reported

by Snytnikov et al. [Snytnikov 2005]. The appearance of mullite phase modifies the Cr^{3+} environment, which may result in a spectral shift of the doublet. Indeed at Si concentration above C^{*}_{Si}=16 mol.%, the doublet undergoes a blue shift to 682.6 and 686.0 nm, which corresponds to θ-Al_2O_3 environment. It is known that silica treatment shifts the nucleation of α-Al_2O_3 to temperatures considerably higher than 1250 °C necessary for α phase appearance in pure UPA [Costanzo 2004]. Indeed, we have found pure θ polymorph after the thermal treatment of TMES treated UPA at 1400 °C during relatively short time of 4 hours. It seems therefore assumable that inclusions of θ phase exist into mullite in small quantities, which cannot be observed by XRD method. At the same time, it seems unlikely that the Cr^{3+} emission originates from traces of θ phase rather than from still significantly present (~10 wt.%) α phase. More probable, the new lines position is explained by the mullite environment. The larger width of the shifted lines indicates more disordered mullite structure compared to α alumina.

Earlier, the Cr^{3+} doublet at 694.3.0 and 692.7 nm has been observed in luminescence of Si containing sillimanite Al_2SiO_5 phase and assumed to be connected to the micro-impurities of α-Al_2O_3 [Gaft 2012]. In our work the doublet is observed at a different spectral position closer to that characteristic of θ-Al_2O_3 environment. Since α phase is strongly present in our Si-containing samples, the difference between the results of Ref. [Gaft 2012] and those of the present study can be rather attributed to different environments, which are respectively sillimanite and 2:1 mullite.

Because of a very low Cr^{3+} concentration in UPA samples, their direct excitation is of low efficiency. At the same time, the energy transfer from the host matrix to impurity centres is expected to be very efficient. This explains relatively easy recording of the Cr^{3+} ions luminescence at the interband host matrix excitation in our experiments. In order to gain more information about the bandgap modification during α-Al_2O_3 to mullite transformation, we have performed measurements of the excitation spectra of Cr^{3+} near-IR luminescence at different Si content. The results are presented in Fig. 4.25.

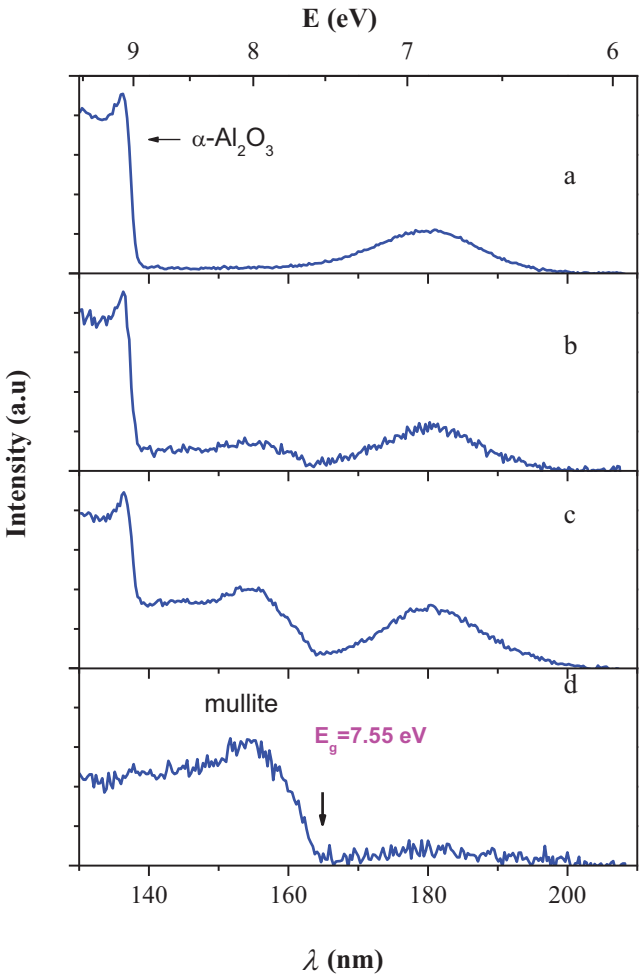

Figure 4.25: Excitation spectra of 690 nm luminescence of TEOS-treated UPA during 1 h (a), 3 h (b), 5 h (c) and 25 h (d). Thermal treatment was conducted at 1400 °C during 8 h.

The luminescence excitation spectra of α-Al_2O_3 are dominated by the interband electronic transitions situated at $h\nu \geq E_g$=9.36 eV (132.47 nm). Additionally, an excitation band appears at 7 eV (180 nm) with Δ_{FWHM}=0.7 eV, previously assigned to the electronic transition from $t_{1u}(\pi)/t_{2u}(\pi)$ nonbonding O-ligand orbitals to $t_{2g}(\pi^*)/e_g(\sigma^*)$ antibonding orbital, localized on Cr^{3+} ion [Tippins 1970].When Si content in alumina increases, another continue grows up at energies above 7.55 eV. In the same time, the α-Al_2O_3 transitions weaken until a complete disappearance at Si concentrations above 20 mol.%, which corresponds to alumina-rich 2:1 mullite. In general, a luminescence excitation spectrum is a convolution of the absorption spectrum and spectral dependence of an energy transfer to the emitting state. The new excitation continuum in Figure 4.25 reflects therefore (like that of pure α-Al_2O_3) the fundamental absorption of a new material. Since the last point corresponds to pure mullite

phase, we attribute the absorption onset at E_g=7.55 eV to the bandgap energy of mullite phase. The obtained value is in good agreement with 7.7±0.2 eV earlier reported by Büchner and Guse [Büchner 1977] for 2:1 mullite single crystal based on electron energy loss measurements and Kramers-Kronig analysis of dielectric tensor components.

4.4.3. Effect of quantity SiO_2 on the optical property

The quantitative analysis of the mullite ratio can be obtained from both XRD and luminescence spectroscopy data. The first needs a normalization factor based on the knowledge of XRD peak sensitivities. The mullite molar ratios of the prepared samples were calculated from the XRD intensity data according to the equation: $F_m^{XRD} = \frac{I_{m120} + I_{m210}}{mI_{m120} + I_{m210} + 2.7 \cdot I_{\alpha 012}}$, where *I*'s denote the respective mullite and α peaks areas. The normalisation factor was estimated from the peak areas of pure mullite and α phases. The mullite ratio obtained from luminescence excitation spectra was calculated from relative intensities (I) of the excitation bands of mullite and α-Al_2O_3: $F_m^{spec} = \frac{I_m}{I_m + I_{\alpha - Al_2O_3}}$. The mullite ratios extracted from XRD and luminescence experiments are shown in Fig. 4.26 versus Si content in UPA samples.

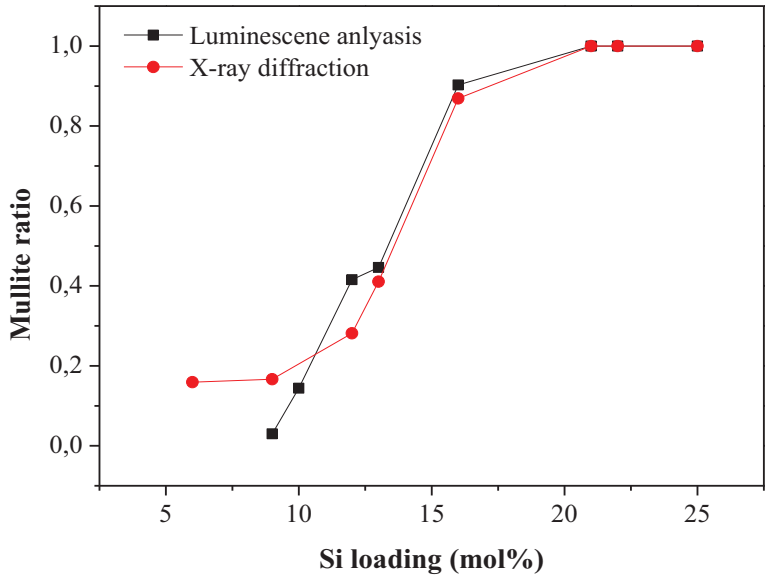

Figure 4.26: Mullite content in ultraporous Al_2O_3 as a function of Si loading derived from X-ray diffraction and luminescence analyses.

An excellent agreement between the data extracted from X-ray diffraction (F_m^{XRD}) and spectroscopy (F_m^{spec}) measurements can be seen for Si content above 9 mol.%. Below this value, the XRD analysis indicates a small presence of mullite while spectroscopic data correspond to the pure α alumina. The origin of this disagreement is not yet clear. The experimental results indicate the mullite phase appearance at Si content of 10 mol.% and the complete transformation to mullite in samples with more than 20 mol.% Si. This last Si content corresponds to the 2:1 mullite composition, which permits to conclude about the alumina-rich 2:1 ($2Al_2O_3 \cdot SiO_2$) phase formation. The Si content variation from 10 to 20 mol.% is accompanied by the intensification of both XRD lines of 2:1 mullite and absorption above 7.55 eV. Neither the XDR lines position nor absorption threshold is changed. All these findings indicate that the phase transition from α-Al_2O_3 to 2:1 mullite does not involve the total sample volume but propagates into the bulk with a phase-transformation reaction front. Accordingly, three phases can coexist in the considered SiO_2/Al_2O_3 system: α-Al_2O_3, silica and their interaction product 2:1 mullite. The lowest Si content when the mullite appears may correspond to the thermodynamic equilibrium between surface mullite and bulk α alumina phases.

4.5. Conclusion

In Chapter 4, we report on chemical, structural and phase transformations of ultraporous nanofibrous aluminum oxyhydroxide (UPA) modified by the impregnation of trimethylethoxysilane (TMES) and tetraethoxysilane (TEOS) followed by an isochronous thermal treatment (4 hours) in the temperature range between 100 and 1600 °C. The mass density, specific surface area and structural fibril thickness of the silica-treated materials were measured and compared with those of pure UPA.

The loaded silica (from 5 to 25 mol.%) strongly affects the UPA modification kinetics leading to a shift of the phase transitions to higher temperatures. Additionally, surface silica prohibits structural water from escaping the structural nanofibrils of UPA and limits those thickening. Consequently, the specific surface area of the silica treated UPA appears to be higher in similar annealing conditions. Along with an increase of annealing temperature leaded to these modifications of phase transformation, the mass density, an average diameter and specific area to compare with UPA.

The transformation of α-Al_2O_3 to mullite was studied by correlated X-ray diffraction and photoluminescence methods. The aluminosilicate solids with different Si:Al ratios were prepared after thermal treatment (1400 °C/ 18 hours) of ultraporous alumina monoliths impregnated with vapor of silica precursors TMES and TEOS at room temperature. The materials show up the near-IR luminescence of Cr^{3+} ions, which concentration in the material is below 10^{-5} wt.%. The zero-phonon doublet at 691.9 (R2) and 693.3 nm (R1) corresponds to ^2E_g-$^4A_{2g}$ transitions of octahedrally coordinated Cr^{3+} ions in a strong crystal field of α alumina. This doublet spectral position shifts at the critical Si concentration C^*_{Si}≥16 mol.%, when mullite phase approaches saturation. The mullite ratio increases with Si content between 10 and 20 mol.%. The total α-Al_2O_3 conversion above 20 mol.% of Si corresponds to 2:1 mullite ($2Al_2O_3 \cdot SiO_2$). We suggest that mullite and α-Al_2O_3 domains coexist, while the mullite phase propagates into the material bulk at the silica addition. The fundamental absorption onset energy 7.55 eV of 2:1 mullite has been measured from the excitation spectra of Cr^{3+} near-IR luminescence. The XRD and luminescence measurements do not indicate the formation of other mullite polymorphs with either lower or higher Si content.

Chapter 5
Model of morphological modifications

In this Chapter 5, a theoretical model will be proposed describing the structural modifications of UPA monoliths during the annealing process, which considers two principal domains of temperature activating diffusional surface mass transport and bulk material sintering. The first takes place at moderate temperatures below the crystallization onset at 870 °C and engages pure additive modification on a single fibril. The second requires take place at the higher temperatures and involves the total mass transport over the UPA fibrils. We show that this model can be successfully applied to the experimental data of the material mass density, specific surface area and the fibril geometry (lengths and diameter) obtained in pure, and silica-treated (TMES and TEOS) UPA. In particular, it permits to obtain activation energies of the mass transport processes and predict the material nanoscale morphology.

5.1. The 3D model of UPA monoliths

The basic building block of raw UPA samples is a fibril, with the mean length about a_0 = 140-160 nm and diameter d_0 = 5-7 nm. These fibrils form the porous structure as a network with multiple connections at the cross points of fibrils.

We assume that during annealing the aspect ratio a/d decreases and elementary fibrils progressively shortened and becoming ellipsoidal-shape particles, when the stable α-Al_2O_3 polymorph is formed at temperatures above 1200 °C (see Chapter 3). However, even in this limit case the interconnected deformed fibrils can be recognised. Therefore we relate the mass density and specific area of UPA materials to the evolution of the shape of elementary fibril. A relevant 3D geometrical model of the raw UPA material is presented in Figure 5.1, where the primary volume:

$$V_0 = a^3 \tag{5.1}$$

contains n_f arbitrary interconnected fibrils. The total volume of fibrils is:

$$V_f = n_f \frac{\pi}{4} a d^2 \tag{5.2}$$

and their mass:

$$M_f = n_f \cdot \rho_f \cdot \frac{\pi}{4} d^2 a \tag{5.3}$$

where ρ_f is a specific density of the fibril's material. Corresponding specific surface area of M_f shall comply with:

$$S_{sp} = n_f \cdot s_f \approx n_f \cdot \pi d a \tag{5.4}$$

where s_f is the surface of a single fibril. In framework of this geometrical approach, as this will be shown below, M_f and S_{sp} depend on the aspect ratio a/d.

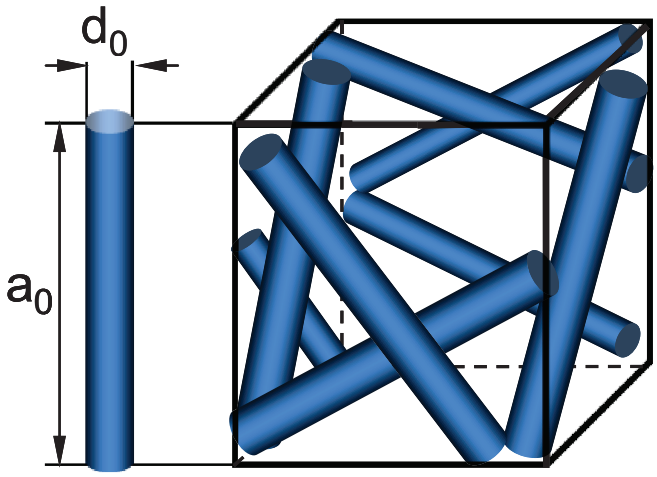

Figure 5.1: 3D representation of UPA structural unit as a elementary volume with arbitrary incorporated fibrils. A structural fibrils is shown with the averaged diameter d_0 and length a_0.

This model approach permits to calculate the mass density and porosity of the UPA materials.

5.1.1. Mass density

We estimated a specific density of the fibril's material close to ρ_f = 2.4 g/cm^3. This reasonably agrees with the data for different crystalline oxyhydrates and aluminum oxides phases with different water content: 2.42 g/cm^3 for gibbsite $Al_2O_3{\cdot}3H_2O$, 2.53 g/cm^3 for bayerite $Al_2O_3{\cdot}3H_2O$, 3.01 g/cm^3 for boehmite $Al_2O_3{\cdot}H_2O$, 3.5 and up to 3.9 g/cm^3 in γ-Al_2O_3 phase stabilised by the structural water (3.67 g/cm^3 - the maximum density of γ-Al_2O_3 at temperatures T ≤ 1200 °C can be obtained), and 3.99 g/cm^3 for α-Al_2O_3 at high sintering temperatures T > 1200 °C.

The mass density of raw UPA material ρ_0 can be calculated as the mass of nanofibrils composed in the volume a^3:

$$\rho_0 = \frac{M_f}{a^3} = n_f \rho_f \cdot \frac{\pi}{4}\left(\frac{d_0}{a_0}\right)^2 \tag{5.5}$$

or average number n of the fibrils in the volume a^3 can be estimated:

$$n_f = \frac{4}{\pi}\frac{\rho_0}{\rho_f}\left(\frac{a_0}{d_0}\right)^2 \tag{5.5a}$$

Using measured mass density $\rho_0 \approx 0.025$ g/cm^3 of raw UPA and the aspect ratio variations a_0/d_0 between 4 and 16, the number of fibrils in the volume a^3 can be estimated from Equation 5.5a as $n_f \approx 10 \pm 6$. We notice that the knowledge of the true pore geometry is not necessary for a definition of the UPA specific density evolution with annealing temperature; the proposed model assumes that it scales with $\rho \propto (d/a)^2$.

5.1.2. Porosity and specific surface area

The porosity can be determined as the relative fraction of the free volume:

$$P = 1 - \frac{V_f}{a^3} = 1 - \frac{M_f}{a^3 \cdot \rho_f} = 1 - \frac{n_f \pi}{4}\left(\frac{d}{a}\right)^2 \tag{5.6}$$

The total surface of nanofibrils in the elementary volume a^3 can be described as:

$$S_f = n_f \cdot s_f = n_f \cdot \pi d a \tag{5.7}$$

Based on these formulas above can calculate the specific surface area of the material (d<<*a*):

$$S_{spec} = \frac{S_f}{\rho_f V_f} = \frac{4}{\rho_f d} \tag{5.8}$$

In a generally case, when one cannot neglect the fibrils diameter (*d*) with respect to length (*a*) the specific surface area is expressed as:

$$S_{spec} = \frac{4}{\rho_f}\left(\frac{1}{a} + \frac{1}{d}\right) \tag{5.9}$$

Equations (5.8) and (5.9) permit an estimation of the specific area of raw UPA monoliths, which confidence range does not exceed 5 %.

And vice versa, these equations can be used for an estimation of the average diameter of nanofibrils as a function of the specific area:

$$d_0 = \frac{4}{\rho_f S_{spec}} \tag{5.10}$$

Under assumption that the general structure of the UPA unit is conserved during thermal modifications of the UPA materials, we can generalise Equation (5.10) as:

$$d(T) = \frac{4}{\rho_f(T) S_{spec}(T)} \tag{5.11}$$

The values of $d(T)$ calculated by using Equation (5.10) from the measured mass density $\rho_f(T)$. One more useful expression relates the material mass density with its specific area, which can be obtained from Equations (5.5) and (5.8):

$$\rho = \frac{m}{V} = \frac{1}{S_{spec}\delta} \qquad \text{or} \qquad \delta \approx 0.03 \cdot \frac{a_0^2}{d_0} \tag{5.12}$$

Where $V = S_{spec} m \delta$ with δ being the "effective nanofibrous thickness".

The mean fibril diameter observed in TEM images of raw UPA (Fig. 3.12) is about 5 nm, which corresponds to that obtained from Equation (5.5) using the original mass density 0.025 g/cm^3 and specific area 300 m^2/g. The similar estimations of effective diameter of nanofibrils in γ (0.04 g/cm^3, 150 m^2/g), θ (0.045 g/cm^3, 100 m^2/g) and α (0.65 g/cm^3, 5 m^2/g) UPA materials result in respective values about 7 nm, 9 nm and 120 nm, which are in agreement with the TEM and SEM observations. We conclude that the model based on the proposed 3D unit successfully describes transformations of fibrous morphology and mass density of UPA materials during thermal treatment.

5.2. Morphological modifications

In this section we consider two principal domains of temperatures, which activate surface mass transport and sintering process. The first takes place at moderate temperatures below the crystallization onset at 870 °C and engages modifications on a single fibril. The second requires considerably higher temperatures and involves the entire material of fibrils. One more particular of the material organisation takes place at low temperatures below ~100 °C, which remains beyond the scope of our interests.

5.2.1. Pure UPA

5.2.1.1. Annealing below 100 °C

In this domain of low temperature the structural water losses are relatively small (n varies are between 3.6 and 1.5 according to Table 3.11). Consequently, the supramolecular structure of the raw $Al_2O_3 \cdot nH_2O$ material is maintained and the changes of the material mass density and specific surface area can be neglected. We assume that only a partial destruction of hydrogen bonds may take place in this temperature range. Moreover, water losses do not lead to any significant modification of the material morphology at nano- and micro- scales.

5.2.1.2. Annealing below 870 °C

The density of UPA changed after annealing in this temperature range remains below 0.04 g/cm^3. The modifications of the amorphous fibrils shape are dominated by the diffusion mass transfer and taken place at the fibril surface. This process leads to a decrease of the fibril

surface-to-volume ratio. Since both agglomeration and sintering of fibrils are not observed in these conditions, we can express the reduction in fibril length $a(t)$ and increase of its diameter $d(t)$ as:

$$a(t) = a_0 - \sqrt{Dt} \tag{5.13}$$

In this formula: a_0 is initial fibril length and D is diffusion coefficient. The mass transport between fibrils and consider the single fibril modification was dismissed. We can express from the conservation of the fibril volume:

$$d^2(t) = d_0^2 \frac{a_0}{a_0 - \sqrt{Dt}} = \frac{d_0^2}{\left(1 - \frac{\sqrt{Dt}}{a_0}\right)} \tag{5.14}$$

From these equations 5.12 and 5.13 the temporal evolution of the fibril aspect ratio during annealing process can obtain:

$$\frac{a}{d} = \frac{a_0}{d_0}\left(1 - \frac{\sqrt{Dt}}{a_0}\right)^{3/2} = \frac{a_0}{d_0}\sqrt{\left(1 - \frac{\sqrt{Dt}}{a_0}\right)^3} \tag{5.15}$$

Where $D = D_0 \cdot \exp\left(-\frac{E_D}{k_B T}\right)$ is the thermally activated process characterized by an activation energy E_D.

Using equation 5.15 and experimentally obtained, we described the diffusion-controlled changes of density and specific area of UPA materials as a function:

$$\rho = \rho_f n_f \frac{\pi}{4} \frac{\left(\frac{d_0}{a_0}\right)^2}{\left(1 - \frac{\sqrt{Dt}}{a_0}\right)^3} \tag{5.16}$$

$$S_{spec} = \frac{4}{\rho_f} \cdot \frac{\sqrt{1 - \frac{\sqrt{Dt}}{a_0}}}{d_0} \tag{5.17}$$

Using the experimental data for $\rho(t)$, $S_{sp}(t)$ and d(T) with a_0 = 140 nm, d_0 = 5 nm and the annealing process duration (t=1.44·10^4 s) the best least-squares fit allows us to estimate the "effective" diffusion coefficient: D_0 = 6·10^{-18} m^2/s and E_D = 23.8±1 kJ/mol. The linear fit of experimental data for the fibril diameter in frames d versus 1/kT at temperatures below 1000 °C is shown in Figure 5.2:

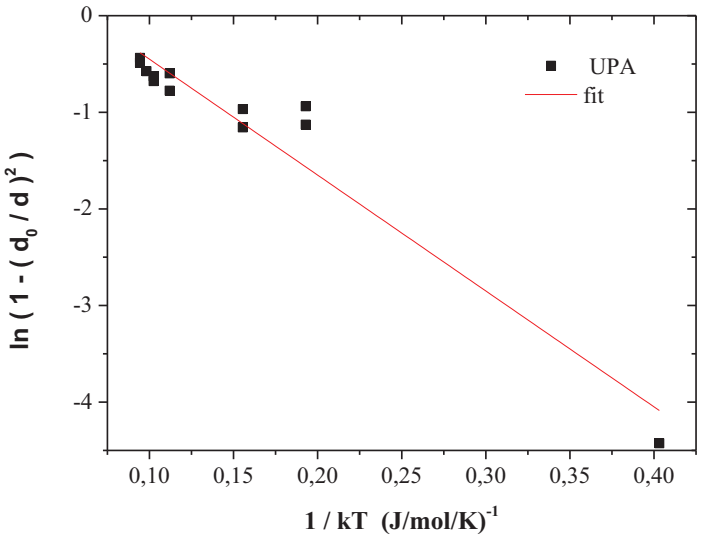

Figure 5.2: Fit of fibril diameter (d) at temperatures below 1000 °C with Equation 5.14.

The good agreement between experimental data and theoretical model in the diffusional surface mass transport related to the aspect ratio *a*/*d* is shown in Fig. 5.3.

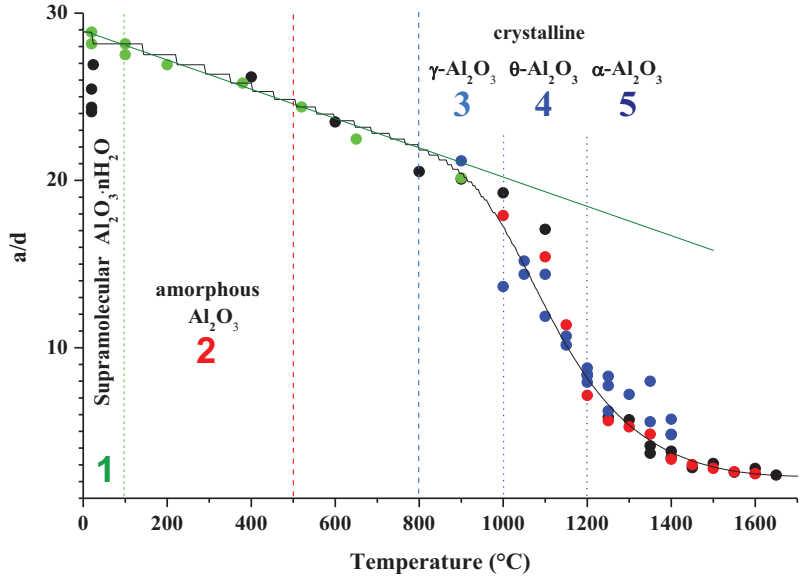

Figure 5.3: Aspect ratio of fibrils versus annealing temperature. The different series of measurements are indicated with different markers ●, ● and ● (Ref. [Mukhin 2012]). Variations of aspect ratio a/d (and UPA mass density) at temperature ~ 25-30 °C are caused by temperature and humidity used for the samples preparation and conservation before measurements.

The obtained value of the diffusion activation energy E_D = 23.8±1 kJ/mol is close to the earlier derived activation energy of structural water removal E_a = 22±5 kJ/mol obtained from

TG data (see Fig. 3.15b of Chapter 3). Therefore, we assume that both processes are intrinsically connected and possess a common mechanism for activation of surface diffusion and for chemical decomposition of oxyhydroxide.

The above formalism is relevant to the conditions when the diffusion mass transport is limited within a single fibril: $\sqrt{Dt} \le a_0$. The native fibrils has a cylindrical shape with the mean diameter d_0 = 5 nm and length a_0 = 140 nm. The average volume of a single fibril is therefore: $V_f = \frac{(\pi d_0^2 a_0)}{4} \approx 2750$ nm^3. The surface mass transport at the annealing results in the shape changes described by Equations 5.1-5.6. Consequently, the aspect ratio decreases by minimizing the fibril surface energy. The surface of an equivalent fibril cylinder reduces until $a_x \approx d_x = l_{max} \approx 15$ nm (or up to the diameter ~ 18 nm for spherical particle). This maximal fibril thickness of 15 nm sets the limit of applicability of the diffusional surface transport model in UPA materials. This however does not take place at temperatures below 1000 °C where the fibrils thickness remains below 10 nm.

The proposed model describes the mass transport within a single fibril and is valid for short annealing times (practically below 10 hours) and moderate temperatures below 870 °C, when the UPA material retains high porosity and low density, whereas sintering process can be neglected. The aspect ratio a/d in these conditions undergoes minor changes between 24 and 20.

5.2.1.3. Annealing above 870 °C

The annealing of UPA materials at high temperatures $T>T^*$=870 °C introduces significant coarsening of the particles, which sizes attain 100-500 nm, that is an order of magnitude larger than the limit singe fibril diameter $l_{max} \approx 15$ nm discussed in the previous paragraph. The mass transport at sintering take place over the contact region between adjacent nanofibrils and progressively involves the overall volume of UPA material. The annealing at temperatures above 1000 °C leads to a significant shrinkage of UPA materials, which is related to an increase of the samples mass density and decrease of free volume. The initial porosity of row UPA sample is 99.3 % and only slightly decreases to 98.8 % after 4 hours annealing at 1000 °C. Further increase of the annealing temperature results in a sharp decrease of porosity down to 71.2 % at 1400 °C, 56.1 % at 1500 °C and to 26.5 % at 1650 °C. It is important to notice significant changes in the fibril morphology, which becomes spherical or ellipsoidal with the aspect ratio $a/d \le 2$.

To describe the structural evolution of UPA materials at high temperatures, it is convenient to analysis the experimental data within the framework of Ivensen's model [Ivensen 1995]. In the following we make used of its simplified version.

We assume that the change of free volume in time follows the relationship:

$$\frac{dV}{dt} = -BV \tag{5.18}$$

Where V is a free space (volume) between the fibrils, which decreases during sintering at high temperatures, $B = B_0 \cdot \exp\left(-\frac{E_b}{k_B T}\right)$, B_0 is the free volume constant and E_b is the activation energy of the bulk mass transport in sintering process. The solution of Equation 5.18 describing changes of the free volume V(T, *t*) ($V = V_{T^*}$ at temperature T*) during sintering time *t* can be presented as:

$$V = V_{T^*} \exp\left(-B_0 t \cdot e^{-\frac{E_b}{k_B T}}\right) \tag{5.19}$$

where V_0 is the free volume in UPA sample at $t = 0$. It is easy to get similar relationship for UPA mass density $\rho(t,T)$ using the sample mass conservation $\rho_0(V_0 + V_f) = \rho(t,T)(V(t,T) + V_f)$ and $\rho_0(V_0 + V_f) \approx \rho_f V_f$ provided, however, that the porosity of the material remains relatively high: $V_0, V(t,T) \gg V_f$:

$$\rho(t,T) = \frac{\rho_0(V_f+V_0)}{V_f+V(t)} = \frac{\rho_0}{1-\frac{(V_0-V(t))}{(V_0+V_f)}} = \frac{\rho_0}{1-\frac{1-exp\left(-B_0 t \cdot exp\left(-\frac{E_b}{kT}\right)\right)}{\left(1+\frac{V_f}{V_0}\right)}} \tag{5.20}$$

where ρ_0 is the initial density of at $t = 0$. Until the material keeps its high porosity, Equation 5.19 can be simplified:

$$\rho(t,T) \cong \frac{\rho_0}{\exp\left(-B_0 t \cdot \exp\left(\frac{E_b}{kT}\right)\right)} \tag{5.20a}$$

This approximation is true if the condition $\left(1 + \frac{V_f}{V_0}\right) \approx 1$ is fulfilled. In the raw UPA V_0 exceeds V_f about 250 times, V_f/V_0 decreases after annealing from 80-85 at ~1000 °C to ~ 2.5 at ~1500 °C.

From the definition of n_f and using $\rho_0 \left(\frac{a_0}{d_0}\right)^2 = \rho(t,T) \left(\frac{a}{d}\right)^2$ one we obtain the expression for evolution of the fibrils aspect ratio a/d during sintering:

$$\frac{a}{d}(t,T) = \frac{a_0}{d_0} \sqrt{exp\left(-B_0 t \cdot exp\left(-\frac{E_b}{kT}\right)\right)} = \frac{a_0}{d_0} exp\left(-\frac{B_0 t}{2} \cdot exp\left(-\frac{E_b}{kT}\right)\right) \tag{5.21}$$

Applying of the least-squares fit with Equation 5.20a to the experimental data of $\rho(t)$ in the sintering regime at temperatures above 870 °C (see Fig. 5.4) and using annealing time t=1.44·10^4 s allows us to obtain values of the activation energy of bulk mass transport E_b = 52.9±4 kJ/mol and free volume parameter B_0 = 9.4·10^{-3} s^{-1}.

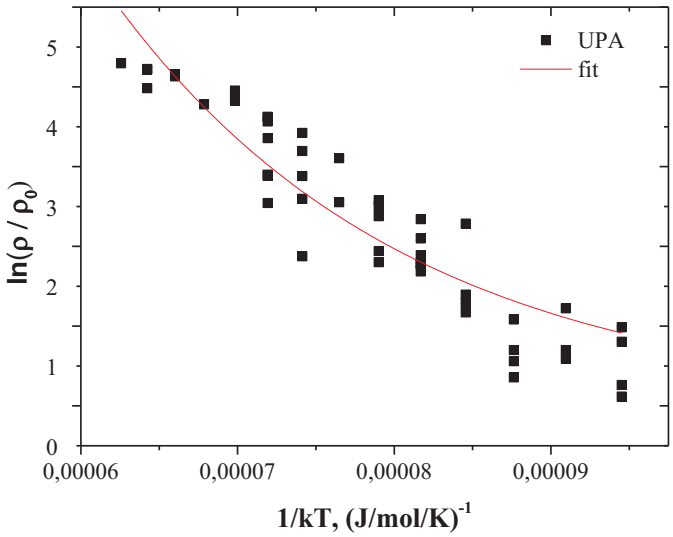

Figure 5.4: Fit of UPA mass density above 1000 °C using Equation 5.20a.

The good agreement between experimental data and theoretical model in the bulk mass transport related to the aspect ratio a/d is shown in Fig. 5.3.

In contrast to the surface diffusional mass transport at moderate temperatures, the sintering engages a profound material restructuring at the atomic scale resulting in the crystalline phase transformation, which activation energy is considerably higher. Since the $\gamma \rightarrow \theta \rightarrow \alpha$ phase transformation is described by common activation energy E_b, the relevant process can be considered as permanent and progressive removal of vacancies from the material bulk, which are apparently connected with the residual structural water. A complete water removal from the UPA structure takes place at the formation of the thermodynamically stable α-phase. The activation energy of the sintering E_b = 52.9±4 kJ/mol is considerably higher than E_D = 23.8±1 kJ/mol the assessment made for moderate annealing temperatures $T \leq$ 870 °C at which the changes of fibrils shape can be associated with the effects of a surface diffusion as well as with shrinking caused by loss of water from amorphous fibril material.

5.2.2. TMES treated UPA

5.2.2.1. Annealing temperatures below 100 °C

In this range of low temperatures, similar to pure UPA, TMES-treated UPA do not significantly lose water and therefore conserve their supramolecular structure. The chemical modifications lead to the linking of $(CH_3)_3$-Si- groups to the surface of alumina nanofibrils. According to our previous discussion in the experimental section, the departure of these groups takes place at higher temperatures between 100 and 400 °C.

5.2.2.2. Annealing below 870 °C

An increase of the annealing temperature affects the deposited TMES and the hydrolysis completes at ~300 °C. The surface of the UPA fibrils is than modified by long chains -Si-O-Si-. This regime is characterised with the diffusional mass along single fibril and can describe fibril diameter, aspect ratio, mass density and specific surface area evolutions of the material by Equations 5.14-5.17, in framework of our theoretical model. In a similar way as in case of pure UPA (Chapter 5.2.1.2), we apply this model to UPA+TMES materials to obtain the process parameters. Figure 5.5 shows the least-squares fit of experimental fibril diameter using Equation 5.14 with a_0 = 140 nm, d_0 = 5 nm and annealing duration t=1.44·10^4 s. This fit results in the diffusion coefficient $D_0 = 2.67 \cdot 10^{-18}$ m^2/s and activation energy $E_D = 23 \pm 2$ kJ/mol. We can conclude that the activation energy of the surface mass transport does not change after the chemical modification of UPA with silica monolayer.

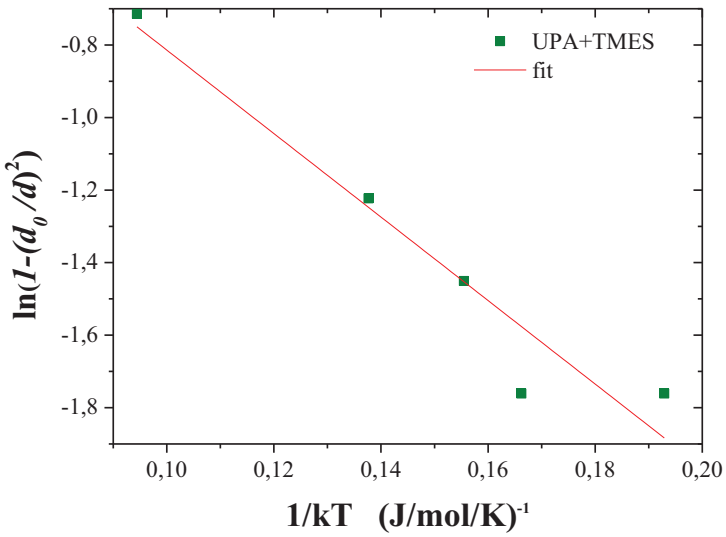

Figure 5.5: Fit of fibril diameter (d) at temperatures below 1000 °C with Equation 5.14.

5.2.2.3. Annealing above 870 °C

The composite UPA+TMES material annealed at high temperatures above 870 °C undergoes a significant shrinkage accompanied by morphological changes of the basic fibril resulted to an increase of the samples mass density and decrease of free volume. While at 1000 °C the initial porosity of raw UPA+TMES material 99.3 % only slightly decreases to 98.8 % after 4 hours annealing, higher temperatures result in a dramatically reduction of porosity down to 85 % at 1400 °C and 78 % at 1600 °C.

The structural evolution of UPA+TMES composite at high temperatures above 870 °C can be explained in framework of our theoretical model (based on Ivensen's model). The experimental data ρ(T) along with their least squares fit with Equation 5.20a (process duration $t = 1.44 \cdot 10^4$ s) is shown in Figure 5.6. This approach provides the activation energy of material sintering E_b = 70.9±7 kJ/mol and free volume constant $B_0 = 2.3 \cdot 10^{-2}$ s^{-1}. Both these obtained values are smaller than in pure UPA material indicating that surface silica favours the bulk mass transport.

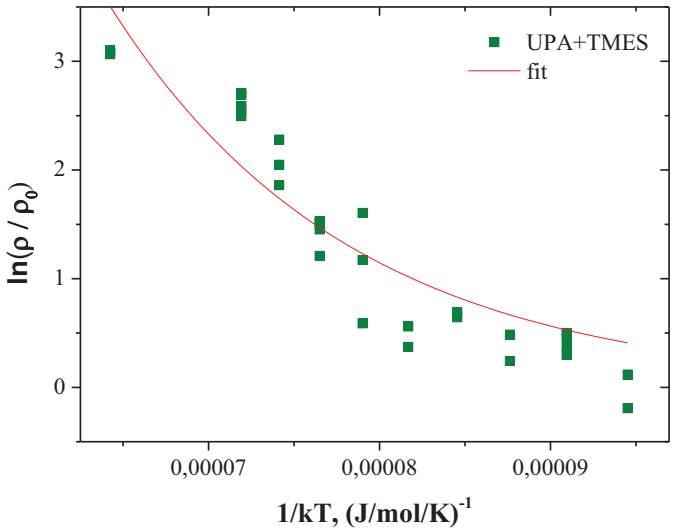

Figure 5.6: Fit of UPA+TMES mass density above 1000 °C using Equation 5.20a.

5.2.3. TEOS treated UPA

5.2.3.1. Annealing temperatures below 100 °C

The impregnation of TEOS in nanofibrous alumina leads to an increase by ~50 % of its mass density without visible increase of the fibril diameter, compared to pure UPA. The TEOS molecule has two oppositely positioned hydroxyls permitting multilayer fibril coverage

with considerably larger elemental Si:Al ratio. By analogy with pure UPA and UPA+TMES materials, we suppose that UPA+TEOS one possesses a supramolecular structure.

5.2.3.2. Annealing below 870 °C

The density of UPA+TEOS material changes after annealing in this temperature range, however, it remains below 0.05 g/cm^3. An increase of temperature leads to the deposition molecules conversion into silica. However compared to UPA+TMES, the TEOS hydrolysis on UPA competes at a higher temperature ~500 °C, which may be explained by a larger thickness of the molecular layer (the deposited TEOS mass on UPA is 5 times higher than that of TMES). In agreement with previous discussion of pure UPA and UPA+TMES materials, the modifications of UPA+TEOS in this temperature range are connected to the diffusion mass transfer over the surface of a single structural fibril, which slightly decreases the aspect ratio. We conclude about the adequate fit of experimental date for fibril diameter with Equation 5.14 presented in Figure 5.7 (using a_0=140 nm, d_0=5 nm and annealing duration t=1.44·10^4 s). As a result, the activation energy: E_D = 20.4±2 kJ/mol and diffusion coefficient D_0 = 2.62·10^{-18} m^2/s of the process were obtained. These values are quite similar (or only slightly lower) to those obtained for UPA+TMES material.

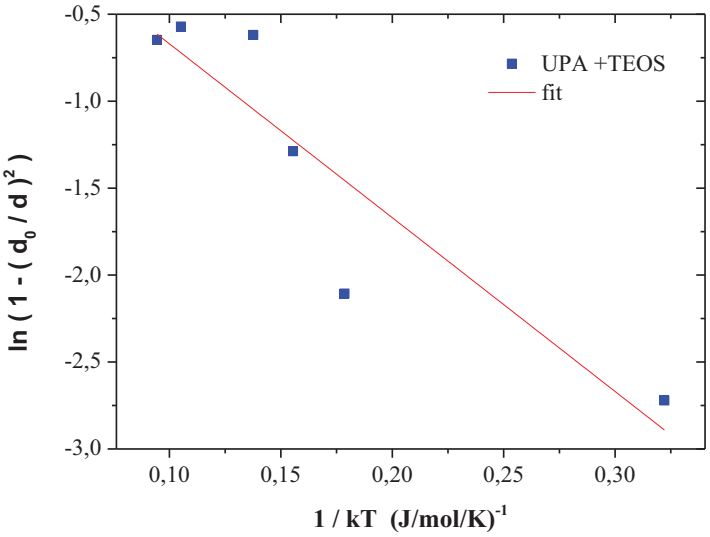

Figure 5.7: Fit of fibril diameter (d) at temperatures below 1000 °C with Equation 5.14.

5.2.3.3. Annealing above 870 °C

The annealing of UPA+TEOS material at high temperatures introduces appreciable morphology modifications seen as an increase of the fibril diameter more than 6 times, which progressively become particles. Those size remains however smaller compared to both previously considered in this regime pure UPA and UPA+TMES materials. At 1400 °C and higher, the composite transforms to mullite with almost stable particles size. The material porosity decreases down to 72 % at 1600 °C.

Similar with the UPA and UPA+TMES we described the structural evolutions of UPA+TEOS material at these temperatures in framework of Ivensen's model. The fit of experimental data for the mass density evolution with Equation 5.20a (for process duration t=1.44·10^4 s) is shown in Figure 5.8. It provides the activation energy of material sintering E_b = 76.5±12 kJ/mol and free volume constant B_0 = 2.86·10^{-2} s^{-1}. These results confirm the trend towards an intensification of the bulk mass transport in silica covered nanofibrils.

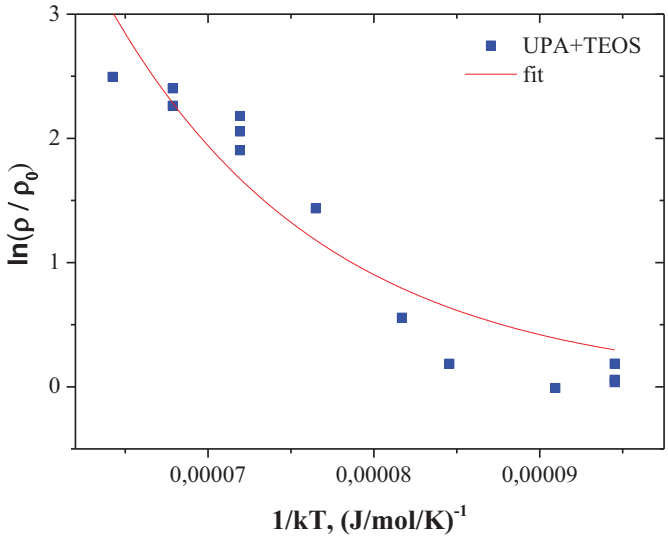

Figure 5.8: Fit of UPA+TEOS mass density above 1000 °C using Equation 5.20a.

5.2.4. Comparison between UPA impregnated with TMES and TEOS

The evolution of mass density and structural fibril diameter with annealing temperature for UPA, UPE+TMES and UPA+TEOS materials are shown respectively in Figure 5.9a and 5.9b.

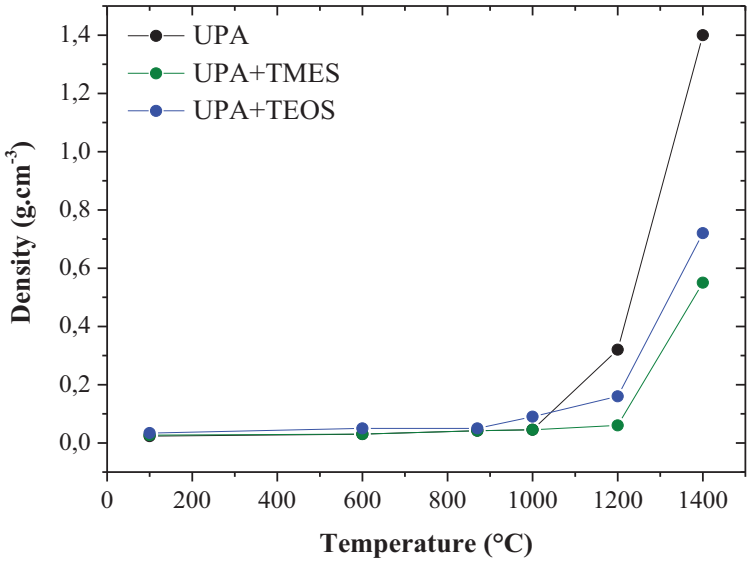

(a)

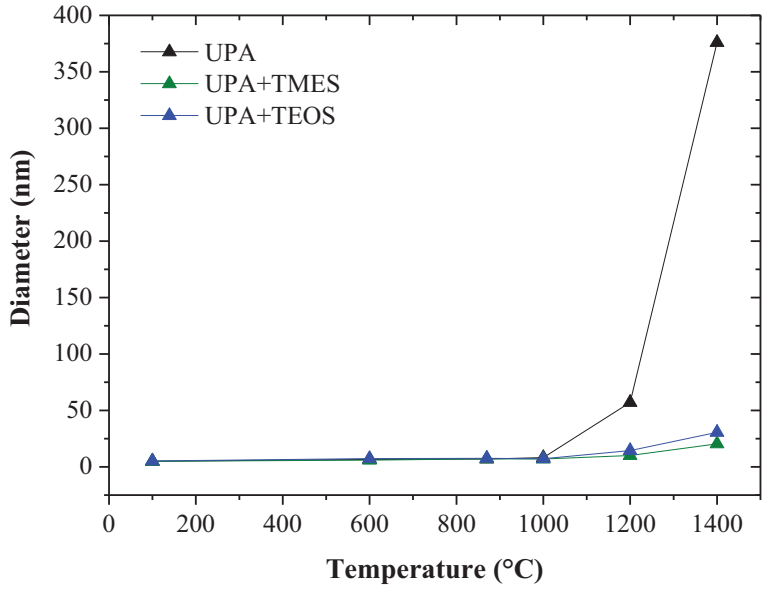

(b)

Figure 5.9: The comparison of density (a) and diameter (b) between UPA, UPA+TMES and UPA+TEOS.

All three materials show no significantly changes of their (initially quite similar) microstructure in the regime of the diffusional surface mass transport, which takes place at temperature below 870 °C. On the other hand, a dramatically change of the material morphology appears at high temperature above 1000 °C related to the material sintering. The proposed theoretical model and comparison between the obtained model parameters summarized in Table 5.1 provides a better understanding of the underlying physical processes.

Table 5.1: Activation energy and coefficients of UPA, UPA+TMES and UPA+TEOS

Regime	Parameters	UPA	UPA+TMES	UPA+TEOS
Mass transport over single fibril	Activation energy (kJ/mol)	23.8	23	20.4
	Diffusion coefficient (m^2/s)	$6 \cdot 10^{-18}$	$2.7 \cdot 10^{-18}$	$2.6 \cdot 10^{-18}$
Bulk mass transport	Activation energy (kJ/mol)	52.9	70.9	76.5
	Free volume coefficient (s^{-1})	$9.4 \cdot 10^{-3}$	$2.3 \cdot 10^{-2}$	$2.9 \cdot 10^{-2}$

According to these results:

(1) In the regime of diffusional surface mass transport, the activation energy does almost not decrease with deposition of a silica layer. Only this layer thickening (almost 5 times) seems to reduce slightly the activation energy. In contrast, the diffusion coefficient significantly decreases after the layer deposition and does almost not change with its thickness.

(2) In the regime of bulk mass transport (sintering), the activation energy sensibly increases after silica deposition and does almost not change with the deposition layer thickening. Accordingly, free volume coefficient strongly increases after the deposition of silica monolayer and does not change significantly when the layer thickness change.

A comparison in the first regime is straighforward and almost stepwise decrease of the diffusion coefficient can be explained by the interface change from free (alumina-air) to solid-solid (alumina-silica). The activation energy of jumps between sites is conditioned by alumina, which organisation is similar. The second regime is connected with the profound reorganisation of the composite material (eventually becoming mullite). The reported physical parameters reflect this reorganisation.

5.3. Conclusion

We proposed a convenient model capable explaining and predicting the evolution under annealing of structural fibril diameter (d), aspect ratio (d/a), mass density (ρ) and specific surface (S) of UPA material, pure and modified with silica. This model considers two regimes of the material modifications: (1) diffusional surface mass transport on a single structural fibril and (2) bulk mass transport involving the total material mass (sintering). The 3D

geometrical representation of the material structure consists of a volume a^3 containing $n_f \approx 10$ arbitrary interconnected fibrils. Based on this representation, the expressions for mass density and specific surface area can be derived.

The structural evolution of pure and silica modified UPA (by TMES and TEOS) was confronted with experimental measurements of the material morphology during thermal annealing in the temperature range between 100 and 1600 °C. The activation energies of the mass transport and pre-exponential constants (diffusion coefficient and free volume) were obtained, providing a better understanding of the underlying physical processes. In the regime of diffusional surface mass transport, the activation energy does almost not decrease with deposition of a silica layer. In contrast, the diffusion coefficient significantly decreases after the layer deposition and does almost not change with its thickness. In the regime of bulk mass transport (sintering), the activation energy sensibly increases after silica deposition and does almost not change with the deposition layer thickening; accordingly, the free volume coefficient strongly increases after the deposition of silica monolayer and does almost not change when this layer thickens.

Chapter 6

Ultra porous alumina for application in microwave planar antennas

Alumina is employed as an insulator in microelectronics, and for high-pressure resistant optical windows in the 0.15-5 μm spectral range. It was also applied for microstrip antenna substrates before being replaced by low-permittivity dielectrics like Duroid®. The broadband dielectric properties of commercial aluminum oxide have been studied [Luneburg 1944] and the commonly reported parameters are: refraction index n~3.1 (at f<10 THz) and dielectric loss $10^{-3}<\tan\delta<10^{-2}$ (0.4<f< 2 THz), which decreases to $3.1\cdot10^{-4}$ (f~0.02 THz) in higher purity 99.6 % alumina. Alumina photonic crystals with the photonic band gap in the frequency range between 0.40 and 0.47 THz have been fabricated and their waveguide properties studied [Martinov 2008] and the prospectus to a control THz waves has been made in this work. Although the principal feasibility of fabrication of photonic structures based on nanofibrous alumina has been demonstrated [Kanaoka 2008], no practical realisation of such systems has been published until now. The importance of measurements of dielectric and waveguide properties of nanofibrous alumina in the THz range of spectra has been underlined [Andreev 2009]. In this Chapter, we report on the first measurements of refractive index and dielectric loss in the GHz-THz frequency range in nanofibrous ultraporous alumina (UPA).

6.1. Motivation

The nanofibrous UPA monoliths were fabricated following to our original method with controlled-conditions as explained in Chapter 3. Whilst, the application in THz optics required low refraction index media, UPA can be a good candidate because of its structural properties. Raw UPA has a mass density of 0.025 g/cm^3, porosity above 99 %, specific area of 300 m²/g [Vignes 1997] and thermal conductivity of 0.01-0.03 W/mK. The raw material is very fragile and does not support any mechanical treatment. Consequently, chemical and thermal treatments can be applied to reinforce the material structure.

The crystallization of γ, θ and α phases in UPA obtained corresponding at 870, 1100 and 1200 °C. This is accompanied by an increase of the characteristic size of alumina fibrils and decrease of the specific surface area of these polymorphs as: 7 nm and 150 m^2/g (γ), 10 nm and 100 m^2/g (θ) and 250 nm and 10 m^2/g (α) [Costanzo 2001]. Moreover, the raw alumina mass density from ~0.02 g/cm^3 increases to 3 g/cm^3 with an increase of the thermal treatment temperature to 1700 °C [Vignes 2008]. Based on these experimental data, the transitions of aluminas are most indicated for THz applications because of their low mass density associated with relative mechanical strength.

In addition to pure UPA materials, UPA treated silica by impregnation of trimethylethoxysilane (TMES) vapour can be used for this goal. UPA+TMES material keeps structural solidness and low mass density after an appropriate annealing, as described in Chapter 4 of this work. Moreover by the impregnation, a monolayer of TMES molecules covering UPA fibrils conveys hydrophobic character to the material. Furthermore, partial hydrophobicity of the formed silica monolayer may be expected after the material annealing.

The THz transparency of the materials is strongly related to water content in the ultraporous structure. Although structural ware can be strongly reduced after annealing from 3 to almost 0.04 molecule per Al atom at the γ phase crystallisation point (870 °C) and below at higher temperatures, the high specific surface area of the material (170 m^2/g for γ phase UPA) favours high water content to be adsorbed. We experimentally obtained the amount of adsorbed water 0.5-0.7 molecules per Al atom for the transition phase UPA (see in Chapter 3). This makes elimination of the adsorbed water mandatory to attain high THz transparency of UPA samples, which required a chemical treatment by appropriate hydrophilic agents.

Below in this Chapter we present the sample preparation for measurements of the refraction index and dielectric loss in the GHz-THz range of frequencies in UPA materials.

6.1.1. Protocol

Samples with well-defined plane faces of circular shape were required to fabricate for these THz measurements. The preparation process was designed and optimised to achieve the good experimental conditions for these measurements. In course of this work, the materials were impregnated with TMES or not, annealed at different temperatures from 600 to 1150 °C, and milled in ceramic bowl by hand and the powder was putted into pattern with diameter 32 mm to form compact samples after the applying the moderate static pressures below 1000 bar. The preparation conditions and samples characteristics are indicated in Table 6.1.

Table 6.1: Preparation conditions of UPA samples for THz measurements

Sample	1st thermal treatment, °C	TMES treatment	Pressure Bar	2nd thermal treatment, °C	Crystalline phase	Density g/cm^3	Thickness mm
1	600	Yes	340	No	amorphous	0.688	4.0
2	600	No	1000	No	amorphous	0.978	2.9
3	800	Yes	340	No	amorphous	0.728	4.2
4	870	No	340	No	γ	0.846	3.6
5	600	Yes	340	1050	γ	0.726	4.4
6	800	Yes	340	1050	γ	0.648	4.4
7	1100	Yes	340	No	γ	0.666	3.3
8a	870	No	1000	No	γ	1.150	2.7
8b*	″	″	″	″	γ	1.150	2.4
9a	1150	Yes	340	No	γ	0.234	8.9
9b*	″	″	″	″	γ	0.234	7.4
10a	1150	No	600	No	θ	0.824	3.5
10b*	″	″	″	″	θ	0.824	5.4

* Samples 8b, 9b and 10b (similar respectively to 8a, 9a and 10a) received an additional hydrophobic chemical treatment after the preparation.

Two methods of the compaction were applied as depicted in Figure 6.1. The simplest one-stage method **1**, used for samples 2, 4, 8 and 10, consisted in UPA growth followed by a thermal treatment (4 hours) and compaction of disks at a static pressure. The mass density of these samples is close to 1 g/cm^3. A slight modification of method **1**, consisting in the introduction of chemical impregnation with TMES vapour at room temperature overnight before thermal treatment and compaction, was used for samples 1, 3, 7 and 9 (method **1'**).

Because of problems with a fragility of disks compacted after annealing of TMES treated UPA, sample 5 and 6 were undergone to a two-stage process **2**, in which an intermediate thermal treatment was introduced at temperature T_1 below the crystallisation threshold of γ phase (870 °C). According to this method, raw UPA material was impregnated with TMES vapour and first heated to 600 °C (sample 5) or 800 °C (sample 6) in order to convert TMES to silica and eliminate structural water. The best shaped disks without any visible cracks were achieved with this method **2**.

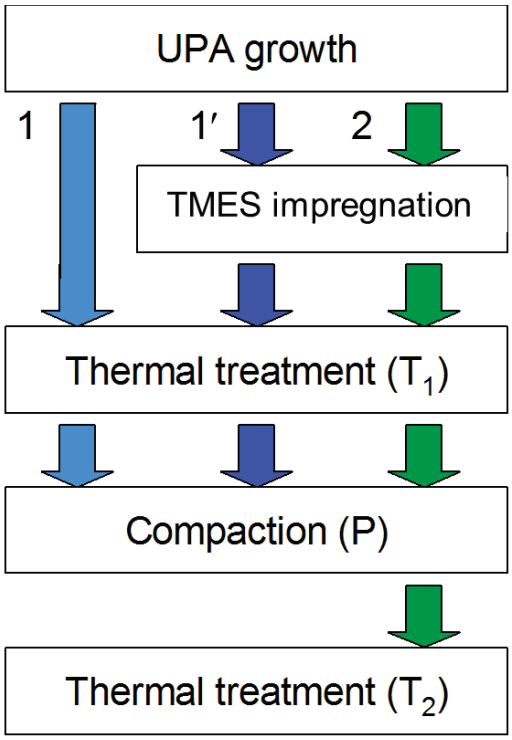

Figure 6.1: The synthesis process of sample.

Samples prepared according to methods **1** and **1'** are shown in Figure 6.2. UPA samples non-treated with silica can be easily compacted by method **1**. In contrast, silica treated UPA disks produces by this method contain shape failures. Method **2** results in quasi-perfect defect-free disks that conserved high porosity of UPA monoliths. As this can be seen from Table 6.1, the mass density of disk samples varied between 0.2 and 1.2 g/cm^3 depending on preparation conditions.

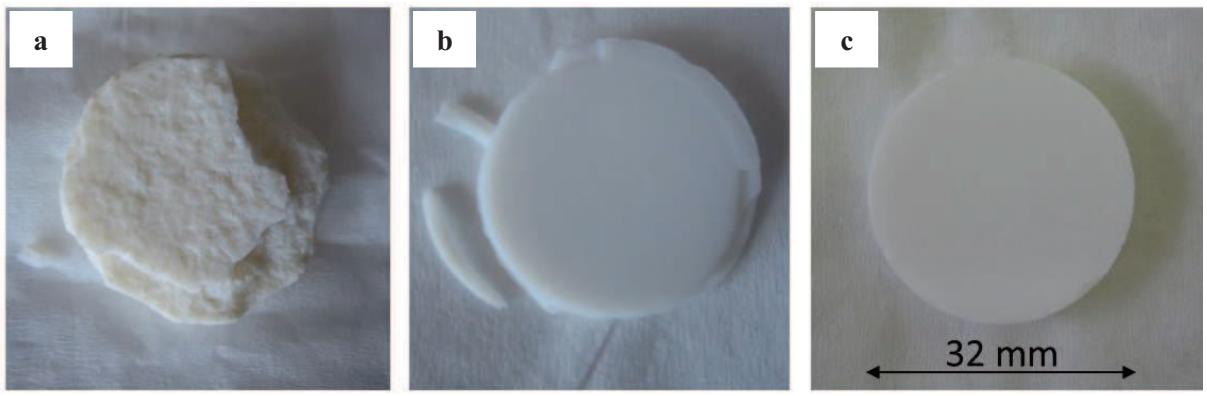

Figure 6.2: Images of compacted silica-treated γ-UPA samples after one-stage (a, b) and two-stage (c) thermal treatment.

6.1.2. Hydrophobic treatment

The hydrophobic treatment was applied to reduce the significant content of adsorbed atmospheric water in samples (50-70 mol.%). This experiment had been carried out at A. N. Frumkin Institute of Physical Chemistry and Electrochemistry RAS (Moscow, Russia). The treatment included immersion of the sample into 2 vol.% solution of Metoxy-{3-[(2,2,3,3,4,4,5,5,6,6,7,7,8,8,8-pentadecafluorooctyl)-oxy]-propyl}-silane (MAF) in dehydrated decane for 2 h followed by rinsing with ethanol and drying in the oven at 130 °C for 1 h. After drying the samples, the successful hydrophobization procedure was checked by the measurement of contact and rolling angles formed by 10 μL water droplet according to method described in reference [Boinovich 2015]. Typical values of contact angle for hydrophobically treated samples exceeded 160°, and rolling angles were less than 13°.

6.2. THz measurement

In order to estimate the complex permittivity of such *ad hoc* UPA samples, we have resorted to the experimental measurement of their scattering-matrix parameters (Figure 6.3) realized in collaboration at the laboratory MPQ (Laboratoire Matériaux et Phénomènes Quantiques, CNRS) at the University Paris 7.

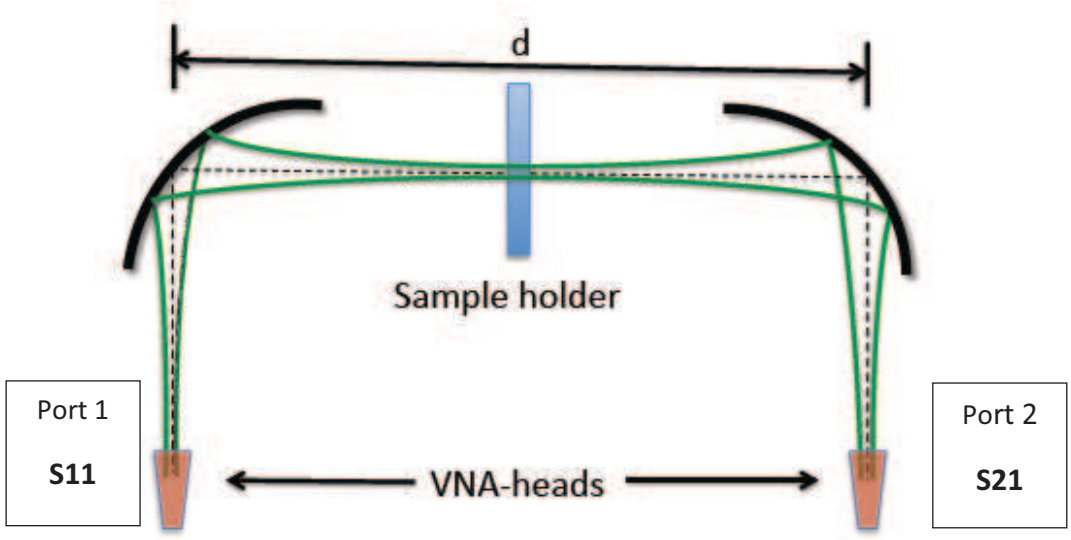

Figure 6.3: Schematic experimental set-up for measuring S-parameters of UPA samples with d=60cm.

The experimental installation is based on a Abmm® Vector Network Analyser MVNA-8-350 [Goy 1999, Mola 2000], endowed with a set of multipliers that allow to cover W-band

(75-110 GHz), D-band (110-170 GHz) and the 170-240 GHz band. In the present work, the D-band millimetric extension was used, for which quasi-optical components were available. From an optical point of view, the set-up is composed by two identical horn antennas, and by two identical off-axis ellipsoidal mirrors (bulk aluminum, machined in-house). The two horns launch a Gaussian beam (98 % of the power in the fundamental mode) with Full width at half maximum (FWHM) =10^{o} and waist radius $w_0 \cong 5.0$ mm, located 7.9 mm behind the aperture. Each ellipsoidal mirror bends the beam by 90^{o}, and image the horn waist radius at the common focal point with magnification M=1 (see Figure 6.3). As a result of this, the waist of the first horn (Port 1) is imaged on the waist of the second horn (Port 2) with overall unitary magnification. In the region between the two mirrors we have a focal point where the beam has a radius comparable with w_0, so that a sample with clear aperture of 20 mm collects ~100 % of the power launched in the fundamental mode, and it is collimated. The sample was put in the holder (Fig. 6.4). Material properties are inferred from the measurement of the Scattering matrix of our dielectric slab.

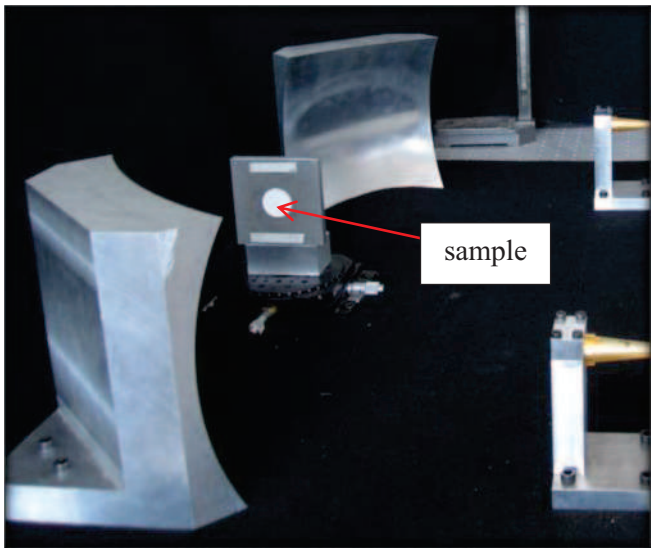

Figure 6.4: The sample in the holder in set-up measurement.

The signal launched from Port 1 is received in Port 1 (S11 scattering matrix element) and Port 2 (S21 scattering matrix element). The parameter S11 gives the complex reflected signal, while S21 provides the transmitted one. Both parameters are available in amplitude and phase *vs* frequency. After calibrating the zero optical path length (= the path before the insertion of the sample, but including the empty framework), the power transmission level sets around ~0.0 dB with -0.01 dB ripples as calibration residuals, while the phase delay is ~0.0^{o}, with

peak-to-peak residuals typically around 10^o (but lower than this, down to 7^o-8^o in some sub-bands). Deviations from these flat calibration levels, once the sample is introduced in the optical path, provide us the losses and the refractive index of the material. Usually Fourier time domain filtering is required to avoid multiple reflections within the optical path (and within the slab itself). To validate our set-up we have used Teflon as a test material, since it is very well known and extensively used at millimeter waves.

6.3. Results and discussion

6.3.1. Refractive index and dielectric loss

The measurements are referenced to Philippe Goy, Michel Goss (Free space vector transmission reflection from 18-760 GHz) [Goy 1999]. The change in phase $\Delta\Phi$ (in the degree) due to the introduction of the slab of thickness e and refractive n, instead of the same thickness of air of refractive index close 1, can be predicted an integer number turn of k:

$$(n-1)\, e/\lambda = (\Delta\Phi/360) + k$$

where λ is wavelength of the microwave in air. When the dielectric material is relatively losses, measurement of the tanδ is extracted from observed decay of transmission α (in dB/cm) at the frequencies where the oscillatory transmission is maximum through formula:

$$\tan\delta = 1.1\alpha\ (\text{dB/cm})/nF\ (\text{GHz})$$

Measurements of the refraction index n and dielectric losses tanδ of prepared UPA samples (from Table 6.1) in the frequency range 135-165 GHz are shown in Figure 6.5 and the obtained values are summarized in Table 6.2.

Table 6.2: Refractive index (n) and dielectric loss (tanδ) of UPA samples (from Table 6.1) in frequency range of 135-165 GHz

Sample	1	2	3	4	5	6	7	8a	8b*	9a	9b*	10a	10b*
n	1.469	1.541	1.476	1.563	1.445	1.406	1.485	1.687	1.927	1.121	1.081	1.513	1.421
tanδ ($x10^{-3}$)	4.70	4.35	4.20	5.60	3.10	2.80	4.00	8.17	3.30	9.90	1.20	17.7	2.00

* Samples 8b, 9b and 10b (similar respectively to 8a, 9a and 10a) received an additional hydrophobic chemical treatment after the preparation.

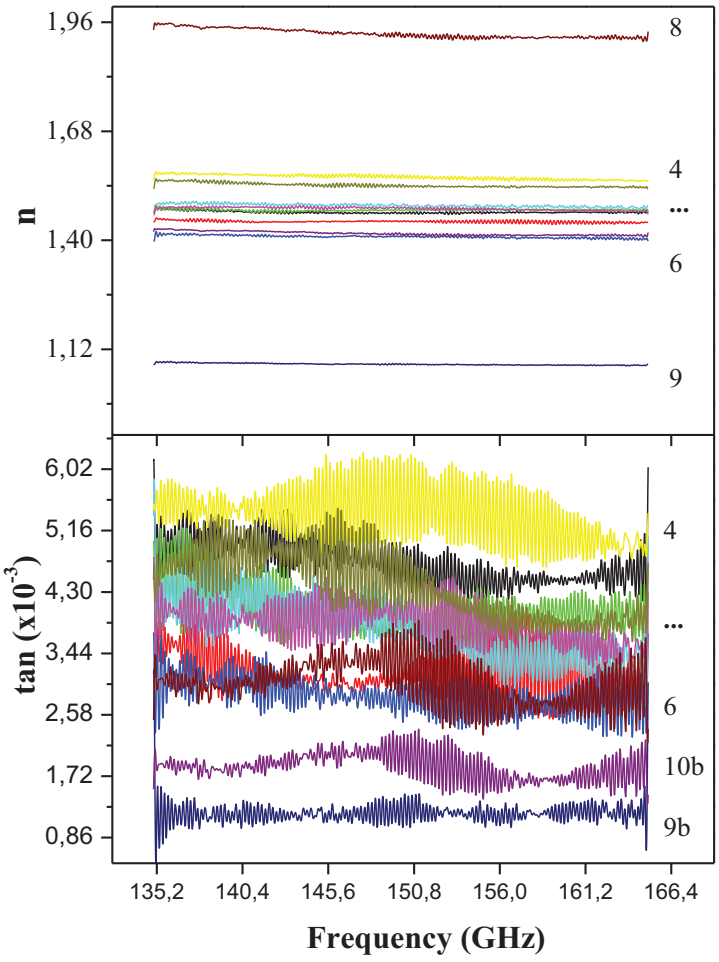

Figure 6.5: Refractive index (n) and dielectric loss (tanδ) of UPA samples from Table 6.1.

The range of refractive index values achieved at frequency 150 GHz after calculation from theory which is a quite broad scope of values $1< n < 2$ and the loss tan $10^{-3}< \tan\delta< 10^{-2}$. Factors affecting refractive index and the dielectric loss of the samples and comparison with reference materials will be discussed in the following Chapter.

6.3.2. Factors affecting

6.3.2.1. Effect of mass density

The refraction index of samples was found to correlate with their mass density as demonstrates Figure 6.6. Some deviations are related to small variations of the samples composition due to the chemical treatments. The linear fit of these data results in

$n = 1.1 + 0.7\rho$ which extrapolation to the high-density solid Al_2O_3 is in a good agreement with the direct measurements n~3.1 performed by Rajab et al. [Rajab 2008].

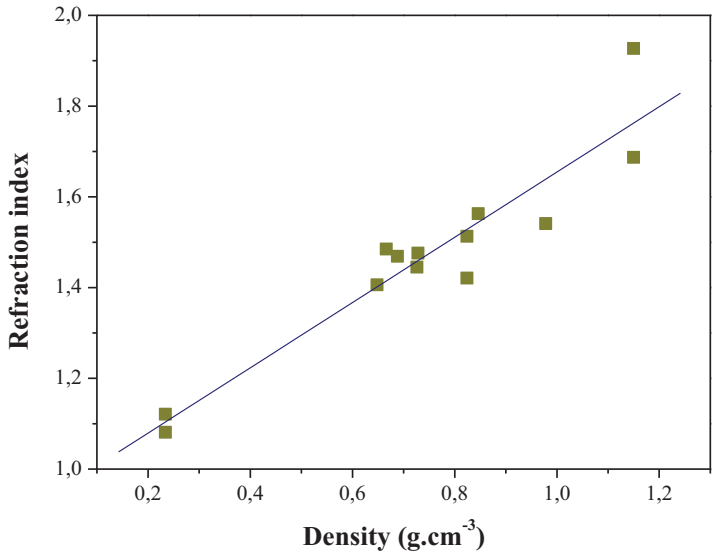

Figure 6.6: Refractive index versus mass density of UPA samples measured at f=150 GHz.

6.3.2.2. Effect of silica treatment

The dielectric loss of silica-treated samples ~$4 \cdot 10^{-3}$ was generally found smaller compared to that of the non-treated samples: $4 \cdot 10^{-3}$–$18 \cdot 10^{-3}$, which is shown in Figure 6.7.

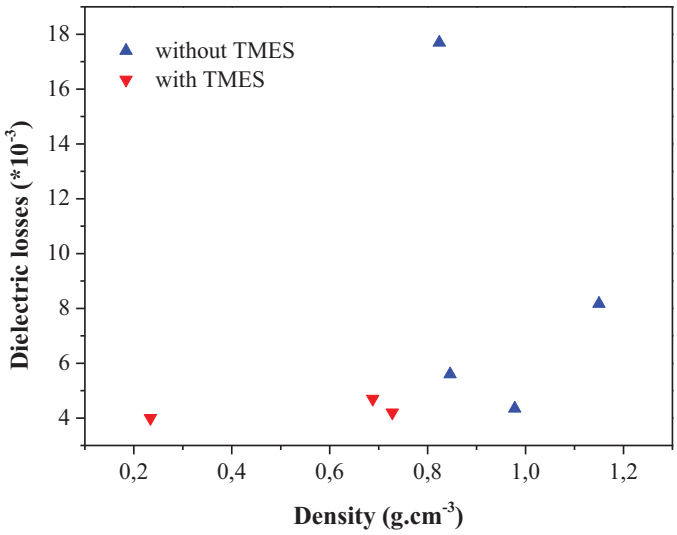

Figure 6.7: *Dielectric loss versus mass density of UPA samples with TMES and without TMES measured at f=150 GHz.*

6.3.2.3. Effect of fabrication method

The samples prepared with the one-stage method show dielectric losses tanδ in the range of $4 \cdot 10^{-3}$ - $18 \cdot 10^{-3}$, which are higher compared to those $\sim 3 \cdot 10^{-3}$ obtained with the two-stage method as shown in Figure 6.8.

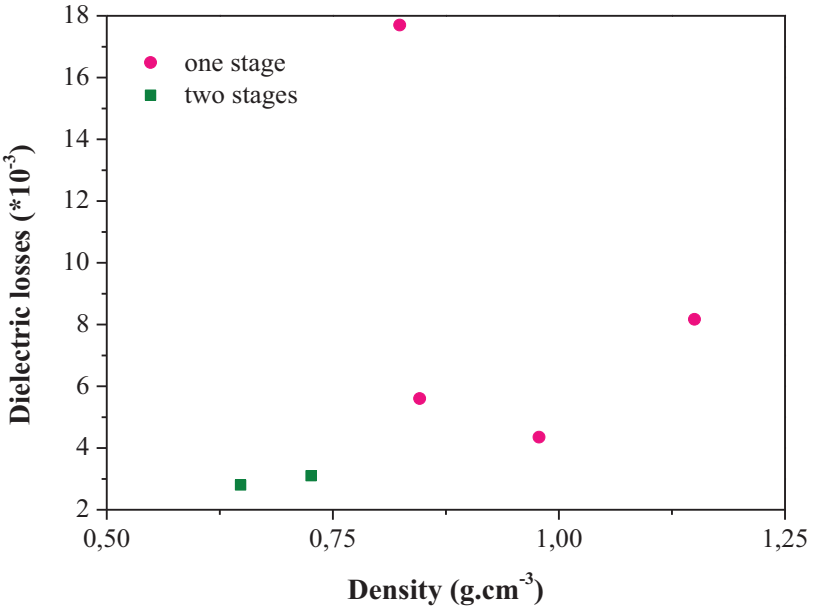

Figure 6.8: Dielectric loss versus mass density of UPA samples prepared after one-stage and two-stage treatments measured at f=150 GHz.

6.3.2.4. Effect of hydrophobic treatment

The additional hydrophobic treatment of samples improves their THz transparency. Figure 6.9 shows that the dielectric loss decreases in the treated samples by an order of magnitude and reaches in the less dense sample $\sim 10^{-3}$ in the frequency range ~150 GHz.

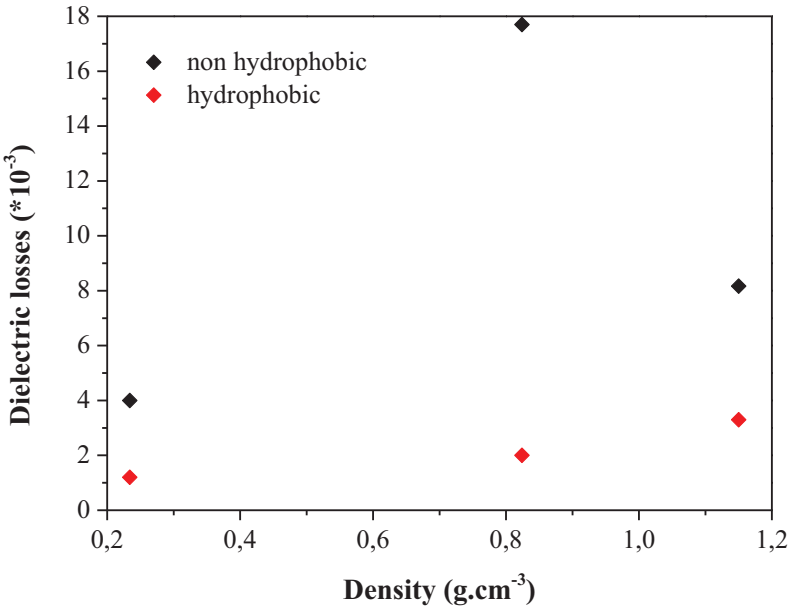

Figure 6.9: Dielectric loss versus mass density of UPA samples without and with additional hydrophobic chemical treatment measured at f=150 GHz.

6.3.3. THz transmission

The complementary measurement of the higher-frequency electromagnetic response in THz FTIR shows a transparency window below 2.5 THz, which opens after the hydrophobic treatment. In particular, the transmittance of sample 9 increases from 0.025 to 0.25 at 1 THz frequency after the treatment. Taking into account the absorption coefficient of liquid water $\alpha \approx 200$ cm^{-1} (f=1 THz) [Xu 2006], measured by us number of the adsorbed water molecules in the UPA structure n=H_2O/Al_2O_3=0.6, UPA mass density ρ=0.234 g/cm^3 and thickness d=0.74 cm (see Table 6.1), one can estimate the expected transmission to be $T = \exp\left(-\alpha d \cdot \rho M_{H_2O} / \rho M_{Al_2O_3}\right)$=0.025, which is in a good agreement with our THz transmission measurements in the non-treated UPA sample shown by curve (b) in Figure 6.10.

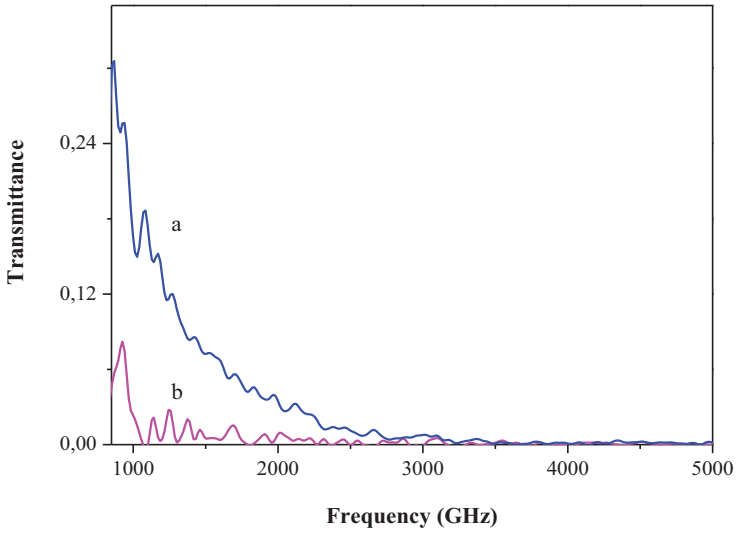

Figure 6.10: THz transmittance of UPA samples 9b (a) and 9a (b) respectively with and without additional hydrophobic chemical treatment.

After hydrophobic treatment, the transmission of sample (a) in Fig. 6.10 was considerably improved, which corresponds to the removal of about 60 mol.% of water and reducing n to 0.26. Since γ-UPA contains a very small amount of structural water (~1 mol.%), the main part of the still remaining water in our sample still belongs to the adsorbed water by the ultraporous structure. Its complete removal will decrease the absorbance by a factor of ~26, which would make nanofibrous UPA highly transparent material in the full THz spectral range and suitable for fabrication of refractory THz optics.

6.3.4. Comparison with reference materials

The best sample 9b of this series showed low refraction index 1.1 and dielectric losses 10^{-3}. This sample has the lowest density, which also explains why its refractive index is very low. The high transmittance of sample 9b is due to its relative hydrophobicity received after the additional chemical treatment. We notice that sample 9b was realized with one-stage method **1'**; then, the comparison with the two-stage method (Chapter 6.3.2.3) may provide an additional possibility to reduce the losses. However since the adsorbed water is still present in the fibrous structure of UPA, the major improvement consists in obtaining its stronger hydrophobicity.

The main result of measurements at GHz frequencies is that optimization of the fabrication process allows ultra-small value of refractive index $\sqrt{\varepsilon_R} \approx 1.1$ and fairly

encouraging value of dielectric losses $\tan\delta \approx 10^{-3}$. Such values compare favorably with those of both common alumina, respectively $\sqrt{\varepsilon_R} \approx 3.2$ and $\tan\delta \approx 10^{-3}$, and Duroid®, $\sqrt{\varepsilon_R} \approx 1.4$ and $\tan\delta \approx 5 \cdot 10^{-4}$.

If we compare our results to those presented in other works dedicated to microwave properties of UPA (e.g. [Penn 1997, Huang 2005]), we can see that the refraction index we find in one of our samples (9b) is one of the closest to n=1 ever reported in literature, nicely scaling to higher values with increasing density. More often, values of n≥2 are presented. On the other side, if we look at dielectric losses, our tanδ is higher with respect to that reported by Penn et al. [Penn 1997]. This effect is likely ascribable to the combined action of humidity and porosity, as reported in Ref. [Molla 1999], who find loss tangent values close to ours, of the order of some 10^{-3}, in the range 12-18 GHz and in a moist environment. An improved hydrophobic treatment should allow us to solve this problem.

6.4. Conclusion

The UPA materials possess interesting dielectric properties making them potentially candidates for refractory optics in THz frequency region. We have developed a method for fabrication of the appropriate samples for GHz-THz optical measurements of refraction index and dielectric losses. Our first measurements show ultra-small value of refractive index $\sqrt{\varepsilon_R} \approx 1.1$ and fairly encouraging value of dielectric losses $\tan\delta \approx 10^{-3}$ attained in our best prepared samples. Different factors affecting the refractive index and the dielectric loss values (fabrication method, mass density, etc.) were discussed. We show that the THz transmission of the samples can be considerably improved by an additional hydrophobic treatment. This hydrophobic treatment permitted to reduce the adsorbed water content from 0.6 to 0.26 water molecule per Al atom of the ultraporous structure. Further improvement of the material hydrophobicity may allow us to obtain the transparent materials for THz frequency range.

General conclusions and perspectives

In this PhD work we investigated the growth process and evolution of structural properties of ultraporous alumina (UPA) monoliths during thermal treatment in the range between 20 and 1600 °C. Pure and silica modified UPA were realized and their structural properties compared. The first measurements of dielectric properties of UPA in GHz-THz range of frequencies have been performed and prospectus for UPA application in microwave planar antenna discussed. A more detailed explanation of the results of this work is given below.

The analysis of principal impurities and their influence on the growth kinetics using technical, high-purity and monocrystalline aluminum was performed. The growth of alumina monolith was found to depend on impurities in the original metals, which higher purity provided faster growth and bigger monoliths at the end. Based on these measurements, we can conclude about partial elements filtering by the Hg-Ag amalgam during the growth process for Si, Fe, Cu, Mn, Ti and Mg, while almost no or little filtering affects Ga and Ag elements. Hg may be entrained into UPA from the amalgam during the growth process, however can be easily removed at the thermal post-treatment stage.

We studied chemical, structural and phase transformations of pure UPA during thermal treatment in the temperature range between 20 and 1600 °C. The annealing results in appreciable structural modifications of UPA materials. The size of elementary structural fibril, specific surface area, mass density and content of structural, adsorbed water and crystalline phase were measured as a function of the annealing temperature. Two kinds of adsorbed and structural water were distinguished and quantified. While the content of adsorbed water (~0.6 molecules per Al atom) in pure UPA depends on the specific surface area and does not appreciably vary below 1000 °C, the content of the structural water strongly decreases from ~3 molecules per Al atom at room temperature to 0.04 at the crystallisation onset temperature of 870 °C (γ-Al_2O_3). The activation energy 22±5 kJ/mol was obtained from experimental data.

We also studied chemical, structural and phase transformations of UPA modified by an impregnation of trimethylethoxysilane (TMES) and tetraethoxysilane (TEOS) followed by an isochronous thermal treatment (4 hours) in the temperature range between 100 and 1600 °C. The size of elementary structural fibril, specific surface area, mass density and content of structural, adsorbed water and crystalline phase were measured as a function of the annealing temperature. We showed that the loaded silica (from 5 to 25 mol.%) strongly affects the UPA modification kinetics leading to a shift of the phase transitions to higher temperatures, while surface silica prohibits structural water from escaping the structural nanofibrils of UPA and limits those thickening.

The correlated XRD and PL analyses were performed explaining the conversion of α phase UPA to 2:1 mullite with an increase of silica loading. The fundamental absorption onset energy 7.55 eV of 2:1 mullite has been measured from the excitation spectra of Cr^{3+} near-IR luminescence. The XRD and luminescence measurements do not indicate the formation of other mullite polymorphs with either lower or higher Si content.

We proposed a convenient model capable explaining and predicting the evolution under annealing of structural fibril diameter (d), aspect ratio (d/a), mass density (ρ) and specific surface (S) of UPA material, pure and modified with silica. This model considers two regimes of the material modifications: (1) diffusional surface mass transport on a single structural fibril and (2) bulk mass transport involving the total material mass (sintering). The 3D geometrical representation of the material structure consists of a volume a^3 containing $n_f \approx 10$ arbitrary interconnected fibrils. Based on this representation, the expressions for mass density and specific surface area can be derived. The structural evolution of pure and silica modified UPA (by TMES and TEOS) was confronted with experimental measurements of the material morphology during the thermal annealing. The activation energies of the mass transport and pre-exponential constants (diffusion coefficient and free volume) were obtained, providing a better understanding of the underlying physical processes.

Finally, we present first measurements of dielectric properties (refractive index and losses) of nanofibrous ultraporous alumina in the GHz-THz frequency range. Different factors affecting the refractive index and the dielectric loss values (fabrication method, mass density, etc.) were discussed. To conduct these experiments, we developed a method for fabrication of compact samples suitable for GHz-THz measurements. An ultra-small value of refractive index $\sqrt{\varepsilon_R} \approx 1.1$ and fairly low value of dielectric losses $\tan\delta \approx 10^{-3}$ were attained in our best prepared samples. We showed that the hydrophobic treatment can reduce the adsorbed water content from 0.6 to 0.26 water molecule per Al atom of the ultraporous structure improving the samples transparency. Further improvement of the material hydrophobicity may allow us to obtain the transparent materials suitable for refractory optics in the THz frequency range.

The UPA materials have been thoroughly examined last decade and their interesting structural and functional properties were reported. Apart for their potential application as supported matrixes for nanoparticles (making feasible *single nanoparticle like* bulk materials), important application in optics of long-wave spectral region can be foreseen (GH-THz frequencies). Consequently, the future studies of these materials can be directed to this field. Along with the research on the better material THz transparency required appropriate

hydrophobic chemical treatment, attempts to elaborate gradient-density materials has to be undertaken. Moreover, future studies have to take into consideration the material mechanical properties, in order to propose a functional material for large-scale applications.

Scientific productions

Publication

1. O. Khatim, **T. H. N. Nguyen**, M. Amamra, L. Museur, A. Khodan, A. Kanaev, Synthesis and photoluminescence properties of nanostructured mullite /α-Al_2O_3, Acta Materialia 71 (2014) 108-116.
2. O. Stepanenko, A. Tartari, M. Amamra, **T. H. N. Nguyen**, M. Piat, I. Favero, S. Ducci, A. Khodan, L. B. Boinovich, A. M. Emelyanenko, A. Kanaev, and G. Leo, Ultra-porous alumina for applications in microwave planar antennas, Advance devices materials, 2016, Vol1, No4.
3. A. Khodan, **T. H. N. Nguyen**, M. Amamra, M. Esaulkov, J-L. Vignes, A. Kanaev, Structural, chemical and phase transformations in nanofibrous aluminum oxyhidroxyde (In preparation).
4. **T. H. N. Nguyen**, A. Khodan, M. Amamra, A. Kanaev, Structural and chemical properties of 3D materials based on nanofibrous aluminum oxyhidroxydes with the surface modified by hydrolysis of ethoxysilanes (In preparation).

Communication

1. **Thi Hang Nga Nguyen**, Mohamed Amamra, Jean Louis Vignes, Andrei Kanaev, Alexei P. Shcherban, Vladimir D. Virich, Anatoly D. Solopichin, Gennnady P. Kovtun

Poster: Kinetics and purity of ultraporous Al2O3 monoliths grown from poly- and mono-crystalline metallic aluminum, E-MRS 2014 Spring meeting, May- Lille France.

2. Oleksandr Stepanenko, Giuseppe Leo, Andrea Tartari, Michel Piat, **Thi Hang Nga Nguyen**, Mohamed Amamra, Andrei Kanaev.

Oral: Ultra-porous alumina for GHz and THz applications, The 8th Terahertz Days Conference, Mars 2015, Savoie, France.

3. O. Stepanenko, A. Tartari, M. Amamra, **T. H. N. Nguyen**, M. Piat, A. Kanaev, and G. Leo.

Poster: Ultra-porous Aluminum Oxides for GHz and THz Components, Progress in Electromagnetics Research Symposium (PERS), 06-09 July 2015, Prague, Czech Republic

4. **T.H.N. Nguyen**, A. Khodan, M. Amamra, J-V. Vignes, A. Kanaev

Oral: Structural and phase transformations of pure and silica treated nanofibrous Al_2O_3, ICNMS 2016: 18th International Conference on Nanotechnology and Materials Sciences, June 2016, Copenhagen, Denmark.

References

-A-

[Aksay 1991] Ilhan A. Aksay, Daniel M. Dabbs and Mehmet Sarikaya, J Am Cerom SOC 74 [10] 58 (1991) 2343.

[Als-Nielsen 2000] Jens Als-Nielsen and Des McMorrow, Elements of Modern X-ray Physics, (2000) by John Wiley & Sons, Ltd.

[Alwitt 1976] R.S. Alwitt, J.W. Diggle, A.K. Vijh (Eds.), Marcel Dekker, New York, (1976).

[Andreev 2009] A. V. Andreev, M. N. Esaulkov, A. N. Khodan, M. M. Nazarov, A. A. Konovko, D. A. Sapozhnikov, I. N. Smirnova, A. P. Shkurinov, Proc. IRMMW-THz Conf. (2009).69-254.

[Azad 2006] A.M. Azad, Meter. Sci. Eng. A, 468 (2006) 435-473.

-B-

[Badkar 1976] P. A. Badkar, J. E. Bailey, Journal of Materials sciences, 11 (1976) 1794-1806.

[Beauvy 2004] Beauvy. M, Vignes J-L, Michel M, Mazerolles L, Frappart C, Di Costanzo T, patent (CNRS-CEA) No FR2847569, 28-05-2004.

[Bilde-Sørensen 1996] J.B.Bilde-Sørensen, B.F.Lawlor, T.Geipel, P.Pirouz, A.H.Heuer, and K.P.D. Lagerlo¨f, Acta Metall. Mater., 44 [5]-52 (1996) 2145.

[Beguin 1991] B. Beguin, E. Garbowski, M. Primet, J. Catal. 127 (1991) 595-604.

[Boinovich 2015] L. B.Boinovich, A. M. Emelyanenko, Colloids Surf., A, 481 (2015) 167-175.

[Bonevich 1993] Bonevich, J. E. and Marks, L. D., Maf. Res. Sot. Symp.Proc., (1993) 286, 3.

[Boumaza 2009] A. Boumaza, L.Favaro, J.Ledion, G.Sattonnay, J.B. Brubach, P.Berthet, A.M.Huntz, P.Royc, R.Tetot, Journal of Solid State Chemistry 182 (2009) 1171-1176.

[Bourdillon 1984] A.J. Bourdillon, S. M. El-Mashri and A. J. Forty, Philos. Mag. A, 49 [3] (1984) 341.

[Bouslama 2012] M. Bouslama, M. C. Amamra, Z. Jia, M. Ben Amar, K. Chhor, O. Brinza, M. Abderrabba, J.-L. Vignes, and A. Kanaev, ACS Catal. 2, (2012) 1884-1892.

[Bouslama 2011] Bouslama, M.; Amamra, R.; Tieng, S.; Brinza, O.; Chhor, K.; Abderrabba, M.; Vignes, J.-L.; Kanaev, A. Appl. Catal., A 2011, 402, 156.

[Bowen 1924] N. L. Bowen and J. W. Greig, J. Am. Ceram. Soc., 7 (1924) 238-54.

[Büchner 1977] Büchner U, Guse W. Physica Status Solidi (b) 1977; 80: 615.

[Brunauer 1938] Brunauer Stephen, Emmett. P.H, Telle Edward (1938), Journal of the American Chemical Society 60 (2): 309-319.

[Brunauer 1937] Brunauer and Emmett, This Journal, 69, (1937) 2682.

-C-

[Cai 2002] Shu-Hui Cai, Sergey N. Rashkeev, Sokrates T. Pantelides and Karl Sohlberg, Physical review letters, number 23 (2002)V 89.

[Cai 2003] Shu-Hui Cai, Sergey N. Rashkeev, Sokrates T. Pantelides, Karl Sohlberg, Physic review, B 67, (2003) 224104.

[Carim 1997] A.H. Carim, G.S. Rohrer, N.R. Dando, S.Y. Tzeng, C.L. Rohrer, A.J. Perrotta J. Am. Ceram. Soc. 80 (1997) 2677-2680.

[Cava 2007] S.Cava, S.M Tebcherani, I. A. Souza, S.A. Pianaro, C.A. Paskocimas, E. longo, J. A. Varela, Materials Chemistry and Physics 103 (2007) 394-399.

[Chandradass 2008] J.Chandradass, D.S. Bae, D.S., M. Balasubramanian, Mater. Manuf. Proc. 23 (8), (2008) 786.

[Chang 2001] P. L. Chang, F. S. Yen, K. C. Cheng, H. L. Wen, Nano Lett. 1, N° 5, (2001) 253-261.

[Costanzo 2001] T. di Costanzo, 'Réactivité d'une alumine monolithique poreuse. Stabilisation de diverses phases d'alumine de transition. Elaboration de matériaux monolithiques poreux', Thèse de doctorat de l'Université Paris VI, 2001.

[Costanzo 2001] T. di Costanzo, C. Frappart, L. Mazerolles, J.-C. Rouchaud, M. Fédoroff, D. Michel, M. Beauvy, J.-L. Vignes, Ann. Chim. Sci. Mat. 26[2] (2001) 67-78.

[Costanzo 2004] T. di Costanzo, A. A. Fomkin, C. Frappart, A. N. Khodan, D. G. Kuznetsov, L. Mazerolles, D. Michel, A. A. Minaev, V. A. Sinitsin, J.-L. Vignes, Mater. Sci. Forum 453-454 (2004) 315-322.

[Cullity 1978] B.D. Cullity, Elements of X-ray Diffraction, 2nd Ed., (1978) by Addison-Wesley.

-D-

[Dan 2004] Li Dan, Xia Y (2004) Adv Mater 16:1151.

[Djuricic 1997] B. Djuricic, S. Pickering, P. Glaude, D. McGarry, P. Tambuyser, J. Mater. Sci. 32 (1997) 589-601.

[Dokko 1977] P.C. Dokko, J A Pask, and K S. Mazdiyasni, J. Am. Ceram. SOC , 60 [3-41] 55 (1977) 150.

[Dynys 1982] F.W. Dynys, J. W. Halloran, Journal of the American Ceramic Society. 65 [9] (1982) 442-448.

-E-

[Epicer 1990] T. Epicier, M.A. O'Keefe, and G Thomas, ActaCrystallogr., Sect A. Cryst Phys., Diffr., Theor. Gen Crystallogr.,46 (1990) 948-62.

-F-

[Formahals 1934] Formhals A., U.S. Patent (1934) No. 1975504.

[Fong 1999] Fong H., I. Chun & D.H. Reneker (1999) Polymer 40, 4585.

[Fong 1999] Fong H. & D.H. Reneker,.J. Polym. Sci: Part B Polym. Phys. 37 (1999) 3488.

[Francis 2007] Francis Rouessac and Annick Rouessac, Chemical Analysis, Modern Instrumentation Methods and Techniques, (2007) second edition.

[Frappart 2000] C. Frappart, Elaboration et caractérisation de monolithes poreux d'alumine obtenus par oxydation d'aluminum. Insertion d'oxydes nanométriques, PhD thesis, University Paris 11, 2000.

-I-

[Ivensen 1995] V.A. Ivensen, Ceramics 34 (1995) 528-533.

-J-

[Jayaram 1989] Jayaram. V and Levi. C. G, Acta metall., (1989) 37(2), 569.

[Jin 2003] Y.Z. Jin, Y.Q. Zhu, K. Brigatti, H.W. Kroto, D.R.M. Walton, Appl. Phys. A: Mater. Sci. Proc., 77 (1) (2003) 113.

-G-

[Gaft 2012] Gaft M, Strek W, Nagli L, Panczer G, Rossman GR, Marciniak L. J Luminescence 2012; 132: 2855; Trinkler L, Berzina B, Jakimovica D, Grabis J, Steins I. Opt Mater (2011) 33: 817].

[Giese 1976] R. F. Giese Jr, Acta Cryst. B32 (1976) 1719-1723.

[Giess 1999] E. A. Giess, J. M. Roldan, P. J. Bailey, and E. Goo, Ceramic Transactions, Vol 15, Microelectronic Systems. American Ceramic Society, Westerville, OH, (1999) 167-72.

[Gentilman 1986] R.L. Gentilman, lnhared Opt Transm Mater., Proc. SPIE, 683 (1986) 2-11.

[Goy 1994] Phillippe Goy, Michel Gross, Communication C10.5 at the 24th European Microwave Conference, Cannes, France, where the complete analyzer system will be shown in operation stand 35, 5-8th(1994) September.

[Guo 2009] B. Guo, H. Yim, Z.P. Luo, J. Aerosol Sci., 40 (4) (2009) 379.

-H-

[Hahn 1995] Hahn, T. (Ed.), Internationul Tables of Crystallography, Vol. A. (1995) Luwer Academic Publishers, London.

[Hart 1953] Hart, R. K., Trans. Faraday Soc. 50 (1953) 269.

[Henken 2009] K. R. Henken, A. Hutchison, John Wiley & Sons, Chichester (2009) 9-68.

[Horiuchi 1999] T. Horiuchi, L. Chen, T. Osaki, T. Sugiyama, K. Suzuki, T. Mori, Catal. Lett. 58 (1999) 89-92.

[Horiuchi 1993] T. Horiuchi, T. Sugiyama, T. Mori, J. Mater. Chem., 3 [8] (1993) 861-865.

[Huang 2000] T. Huang, M. N. Rahman, T.-I. Mah, and T. A. Parthasarathay, J. Am. Ceram. Soc., 83,10 (2000) 204.

[Huang 2005] C.-L. Huang, J.-J. Wang, C.-Y. Huang, 'Sintering Behavior and Microwave Dielectric Properties of Nano Alpha-Alumina', Mat. Lett., (2005) 59, 3746-3749.

-K-

[Kanaoka 2008] H. Kanaoka, S. Kirihara, Y. Miyamoto, J. Mater. Res., 23 (2008) 1036-1041.

[Katada 1995] N. Katada, H. Ishiguro, K. I. Muto, M. Niwa, Adv. Mater., Chem. Vap. Deposition. 1 [2] (1995) 54-60.

[Kirm 1999] Kirm M, Zimmerer G, Feldbach E, Lushchik A, LushchikCh, Savikhin F. Phys Rev B 1999; 60: 502.

[Khatim 2013] O. Khatim, M. Amamra, K. Chhor, T. Bell, D. Novikov, D. Vrel, A. Kanaev, Chem. Phys. Lett. 558 (2013) 53-56.

[Klug 1987] F. J. Klug, S. Prochazka, and R. H. Doremus, J. Am. Ceram. Soc., (1987) 70, 750-9.

[Krischner 1966] Krischner.H Ber.Dtsch. Keram.Ges. 43 (1966) 479-484.

[Kronberg 1957] M. L. Kronberg, ActaMetall, 5, 24 (1957) 507.

-L-

[Larrondo 1981] Larrondo L. & R.S.J. Manley, J. Polym. Sci. Polym. Phys. Edu. 19 (1981) 909.

[Lejus 1964] A.M. Lejus, Rev.HautesTemp.Refract.1 (1964) 53.

[Levin 1998] Igor Levin, David Brandon, J. Am. Ceram. Soc, 81 (1998) 1995-2012.

[Levin 1998] I. Levin and D. G. Brandon, Philos. Mag. Lett., 77, 2 (1998) 117-24.

[Levin 1997] I. Levin, L. A. Bendersky, D. G. Brandon, and M. Ruhle, Acta Metall. Mater., 45, 9,(1997) 3659-69.

[Levin 1998] I. Levin, T. Gemming, and D. G. Brandon, Phys. Status Solidi, A, 166 [1] (1998) 197-218.

[Lee 2003] H. C. Lee, H. J. Kim, S. H. Chung, K. H. Lee, H. C. Lee, J. S. Lee, J. Am. Chem. Soc., 125 (10) (2003) 2882.

[Lee 2007] C. K. Lee, E. Cho, H.-S. Lee, K. S. Seol, and S. Han, Phys. Rev. B 76, (2007) 245110.

[Lippen 1964] Lippens, B. C. and De Boer, J. H., ActaCryst.,17 (1964) 1312.

[Liu 1991] P. Liu, J. Skogsmo, Acta Cryst, B47 (1991) 425-433.

[Luneburg 1944] C. R. Luneburg, "Mathematical Theory of Optics" (1944) Brown University.

-M-

[Ma 2009] M.G. Ma , J.F. Zhu, Mater. Lett.63 (2009) 881.

[Martinov 2008] P. N. Martinov, R. S. Askhadullin, P. A. Yudintzev, A. N. Khodan, New Industr. Technol. 4 (2008) 48-52 (in Russian).

[McArdle 1993] J. L. McArdle, G. L. Messing, J. Am. Ceram. Soc. 76 [1] (1993) 214-222.

[McHale 1997] J.M. McHale, A. Auroux, A.J. Perrotta, A. Navrotsky, Science 277 (1997) 788-791.

[Mizuno 1991] M. Mizuno, J. Am. Ceram. Soc., 74, 22 (1991) 3017.

[Mizushima 1993] Y. Mizushima, M. Hori, J. Mater. Res. 8 [11] (1993) 2993-2999.

[Mohan 2007] D. Mohan, Jr, C. U. Pittman, J. Hazard. Mater. 142, (2007) 1-53.

[Molla] J. Molla, M. Gonzalez, R. Vila, and A. Ibarra, Effect of humidity on microwave dielectric losses of porous alumina', J. Appl. Phys., (1999) 85, 1727-1730.

[Mola 2000] Monty Mola, Stephen, Phillippe Goy, Michel Gross, Review of Scientific instruments, Volume 71, No 1, (2000) January.

[Morrisser 1985] K.J. Morrisser, K.K. Czanderna, R.P. Merrill and C.B. Carer, Ultramicroscopy 18 (1985) 379-386.

[Mukhin 2012] V.I. Mukhin, A.N. Khodan, M.M. Nazarov, A.P. Shkurinov, Radiophys. Quant. Electron. 54 (2012) 591-599.

[Museur 2013] L. Museur, M. Bouslama, M. Amamra, and A. Kanaev, P hys. Status Solidi RRL 7, No. 11, (2013) 1026–1029.

[Musikant 1981] S. Musikant, Emerging Opt. Mater., Proc SPIE, 297 (1981) 2-12.

[Mukhin 2012] V.I. Mukhin, A.N. Khodan, M.M. Nazarov, A.P. Shkurinov, Radiophys. Quant. Electron. 54 (2012) 591-599.

-N-

[Navrotsky 2003] A. Navrotsky, Geochem. Trans. 4 (2003) 34-37.

[Nixon 1971] W. C. Nixon, Phil. Trans. Ray. Soc. Lond. B. 261 (1971) 45-50.

[Nixon 1990] R.D. Nixon, S. Chevacharoenkul, R F Davis, T N Tiegs, American Ceramic Society, Westerville, (1990) OH.

[Nordahl 1998] C. S. Nordahl, G. L. Messing, ThermochimicaActa. 318 [1-2] (1998) 187-199.

[Noordin 2010] M.R. Noordin, K.Y. Liew, A. Kumar (Ed.), Nanofibers (2010) InTech.

-O-

[Odanović 2004] Z. Odanović and M. Djurdjević, J. Serb. Chem. Soc. 69 [12] (2004)1111-1120.

[Okada 2000] K. Okada, A. Hattori, Y. Kameshima, A. Yasumori, R. N. Das, J. Am. Ceram. Soc. 83 [5] (2000) 1233-1236.

[Okada 2000] K. Okada, A. Hattori, T. Taniguchi, A. Nukui, J. Am. Ceram. Soc. 83 [4] (2000) 928-932.

[Okumiya 1971] Okumiya, Ymaguchi, Yamada, O. & ONO, S. Bull. Chem. Soc. Jpn, 44 (1971) 418-423.

[Ollivier 1997] B. Ollivier, R. Retoux, P. Lacorre, D. Massiot, G. Férey, J. master. Chem.7 (1997)1049-1056.

[Ozawa 1996] M. Ozawa, O. Kato, S. Suzuki, Y. Hattori, M. Yamamura, J. Mater. Sci. Lett. 15 (1996) 564-567.

[Ozawa 1998] M. Ozawa, O. Kato, S. Suzuki, J. Mater. Sci. 33 (1998) 737-741.

-P-

[Palmero 2011] P. Palmero, V. Naglieri, M. Azar, V. Garnier, M. Lombardi, L. Joly-Pottuz, J. Chevalier, L. Montanaro, Verres Céramiques & Composites, Vol. 1, N°1 (2011) 62-75.

[Panda 2007] P.K. Panda, S. Ramakrisna, J. Mater Sci (2007) 42: 2189.

[Pan 2008] [Pan C, Chen S-Y, Shen P. J Cryst Growth (2008) 310: 699.

[Patra 2005] Patra A, Tallman RE, Weinstein BA. Opt Mater (2005) 27: 1396.

[Park 2004] J. H. Park, M. K. Lee, C. K. Rhee, W. W. Kim, Mater Sci. Eng. A, 1263 (2004) 375-377.

[Penn 1997] S. J. Penn, N. M. Alford, A. Templeton, X. Wang, M. Xu, M. Reece, and K. Schrape, J. Am. Ceram. Soc., (1997) 80, 1885-88.

[Pijolat 1987] M. Pijolat, M. Dauzat, M. Soustelle, Thermochim. Acta. 122 (1987) 71-77.

[Pinnel 1972] M.R. Pinnel, J.E. Bennet, J. Mater. Sci. 7 (1972) 1016-1026.

[Peng 2002] X.S. Peng, L.D. Zhang, G.W. Meng, X.F. Wang, Y.W. Wang, C.Z. Wang, G.S. Wu: J. Phys. Chem. B 106,(2002) 11 163.

[Poezd 1978] I.P. Poezd, E.D. Radchenko, E.Y. Shenko, D.F. Poezd, A.V. Agafonov, S.N. Alekseev, Oil Refining Petrochemistry 2 (1978) 11-12 (in Russian).

[Prochazka 1983] Prochazka and F. J. Kiug, J. Am. Ceram. SOC., 66 [12] (1983) 874-80.

-R-

[Rajab 2008] K. Z. Rajab, M. Naftaly, E. H. Linfield, J. C. Nino, D. Arenas, D. Tanner, R. Mittra, M. Lanagan, J. Micro. Elect. Pack. 5 (2008) 101–106.

[Redrern 1963] Coats.A.Wand Redrern. J.P., Thermogravimetric Analysis, A Review, Analyst, (1963) Vol. 88 December.

[Reneker 1996] Reneker. DH, Chun I (1996) Nanotechnology 7:216.

[Repelin 1990] Y. Repelin and E. Husson, Mater. Res. Bull 25 (1990) 611-21.

[Roy 1953] R. Roy and E. E. Francis, Am Mineral.7 (1953) 725-28.

-S-

[Saito 1998] Y. Saito, T. Takei, S. Hayashi, A. Yasumori, K. Okada, J. Am. Ceram. Soc. 81 [8] (1998) 2197-2200.

[Sawicka 2006] K.M. Sawicka, P.Gouma, J. Nanopart. Res.(2006) 8:769.

[Shigeo 1962] Shigeo Aramaki, Rustum Roy, Vol.45 (1962) No.5.

[Schneider 2015] Hartmut Schneider, Reinhard X. Fischer and JurgenSchreuer, J. Am. Ceram. Soc., 98 [10] (2015) 2948-2967.

[Schubert 2000] Schubert. U, Hu¨sing .N, Wiley-VCH, Germany vol 208 (2000) 203.

[Scherban] A. P. Scherban, V. D. Virich, A. D. Solopichin, G. P. Kovtun, H. N. Nguyen, M. Amamra M. Kayser, A. Kanaev, Proc. EMRS (2014) Spring Conference, May 26-30, Lille, France.

[Skoog 1998] Skoog, Holler, Nieman, Priciples of Instrumental Analysis, (1998) fifth edition.

[Snytnikov] Snytnikov VN, Stoyanovskii VO, Ushakov VA, Parmon VN. Kinet Catal (2005) 46: 260.

[Souza Santos 1958] P. Souza Santos, A. Vallejo-Freire, J. Parsons, J. H. L. Watson, September (1958), Volume 14, Issue 9, 318-320.

[Stumpf 1950] H.C. Stumpf, A. S. Ruseel, J. W. Newsome, C .M. Tucker, In. Eng. Chem.42, (1950)1398-1403.

[Stepanenko 2015] O. Stepanenko, A. Tartari, M. Amamra, T. H. N. Nguyen, M. Piat, I. Favero, S. Ducci, A. Khodan, L. B. Boinovich, A. M. Emelyanenko, A. Kanaev, G. Leo, Advanced Device Materials (2015), in press (DOI: 10.1080/20550308.2015.1120442).

[Sundaray 2004] Sundaray. B, Subramanian. V, Natarajan. T.S, Appl Phys Lett (2004) 84:1222.

-T-

[Tan 2005] Tan. S-H, Inai. R, Kotaki. M, Ramakrishna. S, (2005) Polymer 46:6128.

[Tang 2001] C.C. Tang, S.S. Fan, P. Li, M.L. Chapelle, H.Y. Dang: J. Cryst. Growth 224, (2001) 117.

[Tchieda 2016] Victor K. Tchieda, Emilio D'Amato, AgostinaChiavola, MariapaolaParisi, Angelo Chianese, Mohamed Amamra, Andrei Kanaev, Clean – Soil, Air, Water (2016) 43 (9999) 1 –10.

[Tippins 1970] H. H. Tippins, Phys Rev. B 1 (1970) 126-135.

[Teoh 2007] G. L. Teoh, K. Y. Liew, W. A. K. Mahmood, J. Sol-Gel Sci. Technol., (2007) 44(3): 177.

[Torrecillas 1999] R. Torrecillas, et at, J. Eur. Ceram. Soc., 19,(1999) 2519-27.

[Tuttle 2008] R.W. Tuttle, A. Chowdury, E.T. Bender, R.D. Ramsier, J.L. Rapp, M.P. Espe, Appl. Surf. Sci.,(2008), 254: 4928.

[Tummala 1991] R. Tummala, Am Ceram. SOC. 74 [5] (1991) 8955908.

-V-

[Valbis 1991] Valbis J, Itoh N. Rad Effects Defects Solids 1991; 116: 171.

[Vignes 1997] J.-L. Vignes, L. Mazerolles, D. Michel, Key Eng. Mater. 132-136 (1997) 432-435.

[Vignes 2008] J.-L. Vignes, C. Frappart, T. Di Costanzo, J.-C. Rouchaud, L. Mazerolles and D. Michel: J. Mater. Sci., 43 (2008) 1234–1240.

[Vinogradov 2008] V.V. Vinogradov, A.V. Agafonov, Catal. Industr 5 (2008) 17-21 (in Russian).

-W-

[Wanger 1964] R.S., W.C. Ellis: Appl. Phys. Lett. 4 (1964) 89.

[Wang 1999] J. A. Wang, X. Bokhimi, A. Morales, O. Novaro, T. Lo´pez, and R.Go´mez, J. Phys. Chem. B 103 (1999) 299.

[Wang 2007] J. Wang, Y. Wang, M. Qiao, S. Xie, K. Fan, Mater. Lett, 61(28), (2007) 5074.

[Watson 1957] J. H. L. Watson, A. Vallejo-Freire, P. de Souza Santos, J. Parsons, Kolloid-Z. 154 (1957) 4-15.

[Waseda 1995] Y. Waseda, K. Sugiyama, and J. M. Toguri, Z. Naturforsch., A: Phys. Sci., 50 [8] (1995) 770-74.

[Warren 1969] B.E. Warren, X-ray Diffraction, (1969) by General Publishing Company.

[Wefers 1987] K. Wefers and C.Misra, Alcoa Laboratories Technical, Report (1987) No. 19.

[Wen 2000] Hui-Ling Wen, Fu-Su Yen, Journal of Crystal Growth 208 (2000) 696-708.

[Wen 1998] Wen Q, Lipkin DM, Clarke DR. J Am Ceram Soc (1998) 81: 3345

[Wislicenus1908] H. Wislicenus, Kolloid-Z.2 (1908) XI-XX.

[Wislicenus 1926] Wislicenus, H., Colloid Chemistry, 1 (1926) 628.

[Wislicenus 1642] Wislicenus, H., Kolloid-Z.,100 (1942) 66.

-X-

[Xiandeng 2000] Xiandeng Hou and Bradley T. Jones, Inductively Coupled Plasma/Optical Emission Spectrometry, Encyclopedia of Analytical Chemistry R.A. Meyers (Ed.) (2000) 9468–9485 John Wiley & Sons Ltd, Chichester.

[Xu 2006] J. Xu, K. W. Plaxco, S. J. Allen, J. Chem. Phys., 124 (2006) 036101.

[Xue 1992] L. A. Xue, I. W. Chen, J. Mater. Sci. Lett. 11 (1992) 443-445.

-Y-

[Yamaguchi 1964] Yamaguchi, G., Yanagida, H. and Ono, S., Bull. Chem. Sot. Jpn (1964) 37, 752.

[Yang 1988] X. Yang, A. C. Pierre, D. R. Uhlmann, Journal of non-Crystalline Solids. 100 (1988) 371–377.

[Yang 2009] Q. Yang, Y. Deng, W. Hu, Ceram. Intern 35(1), (2009) 531.

-Z-

[Zimmerer 1991] Zimmerer G, Nucl. Instrum. Methods Phys. Res. A (1991) 308: 178.

[Zhang 1998] H. Zhang, J.F. Banfield, J. Mater. Chem. 8 (1998) 2073-2076.

[Zhou 1991] Zhou, R. S. and Snyder, R. L., ActaCryst.,(1991) 847, 617.

[Zhou 1991] Rong Sheng Zhou, Robert L.Snyder, ActaCryst, B47 (1991) 617-630.

[Zhu 2002] H.Y. Zhu, J.D. Riches and J.C. Barry, Chem. Mater., 14, (2002) 2086.

[Zhou 2002] J. Zhou, S. Z. Deng, J. Chen, J. C. She, N. S. Xu, Chem. Phys. Lett., 365 (5-6) (2002) 505.

[Zuo 2006] Y. Zuo, Y. Zhao, X. Li, N. Li, X. Bai, S. Qiu, W. Yu, Mater. Lett, 60 (24), (2006) 2937.

[Zura 1978] G.Mc. Zura, K.P. Goodboy, J.J. Koenig in Kirk-Othmer Encyclopedia of Chemical Technology, John Weiley, New York. 2, (1978) 218-244.

Annex 1

Technical aluminum (Al-Tech, 11069-2001 Ukraine)

Element	%mass
Al	99.85
Si	0.06
Fe	0.08
Cu	0.01
Mg	0.02
Mn	0.02
Zn	0.02
Ga	0.03
Ti	0.008
Other elements	0.02

High purity aluminum (Al-HP, Goodfellow): 99.999%

Element	ppm
Si	0.8
Fe	0.3
Cu	0.3
Mg	1.2

High purity mono-crystalline aluminum (Al-Mono HP, PhTI Kharkov – Ukraine)

Element	%mass
Al	99.999
Si	0.0002
Fe	0.00007
Cu	<0.000003
Mg	<0.0000007
Mn	<0.000002
Zn	<0.000005
Ga	<0.000004
Ti	<0.00002
Hg	<0.00004
Ag	<0.00001
Other elements	≈0.0002

Abstract

In this PhD work we investigated growth process and evolution of structural properties of ultraporous alumina (UPA) monoliths during thermal treatment in the range between 20 and 1600 °C. A simple theoretical model was proposed permitting description and prediction of the material structure. A particular extension of this study concerns the mullite formation with an increase of the silica loading. Furthermore, first measurements of dielectric properties (refraction index and losses) in GHz-THz range of frequencies were performed, indicating this material to be potentially interesting for fabrication of the refraction optics.

The experimental installation for UPA elaboration is described, and the analysis is presented of principal impurities and their influence on the growth kinetics using technical, high-purity and monocrystalline aluminum. The obtained materials were characterized by XRD, TEM, SEM, ICP/OES, TGA and PL methods. UPA modified with TMES and TEOS vapor impregnations were also obtained and analyzed. The fibril size, specific surface area, mass density and content of structural, adsorbed water and crystalline phase were measured for different UPA materials as a function of the annealing temperature. The correlated XRD and PL analyses was performed explaining the conversion of α phase UPA to 2:1 mullite, which fundamental band gap was set to 7.55 eV.

The proposed model distinguished two principal regimes of thermal modifications: surface diffusional mass transport over a single fibril and bulk mass transport involving total material mass (sintering). The activation energies of the mass transport and pre-exponential constants (diffusion coefficient and free volume) in both regimes were obtained, providing a better understanding of the underlying physical processes in different UPA materials. Based on these results, we conclude about a common origin of morphological, chemical composition and phase transformations.

Keywords*: ultraporous nanofibrous alumina, phase transformations, silica-modified, thermal treatment, morphology, activation energy.*

Résumé

Dans le travail de thèse, nous avons étudié le processus de croissance et l'évolution des propriétés structurales de l'alumine ultra-poreuse (UPA) monolithique pendant le traitement thermique dans le domaine des températures entre 20 et 1600 °C. Un modèle théorique a été proposé permettant de décrire et prédire sa structure. La formation de mullite à partir d'alumine imprégnée par la silice a été également étudiée. Les premières mesures conduites sur les propriétés diélectriques des UPA dans le domaine de fréquences GHz-THz montrent des possibilités d'application dans le domaine de l'optique réfractrice.

L'installation expérimentale pour l'élaboration des monolithes ultra poreux est décrite. L'étude de la cinétique de croissance à partir d'aluminium technique, ultra pur et monocristallin a permis d'analyser l'influence des différentes impuretés présentes. Les matériaux ont été caractérisés par les méthodes DRX, MET/MEB, ICP/OES, TGA et PL. Les UPA modifiées chimiquement par imprégnation de TMES et TEOS en phase vapeur ont également été analysées. L'étude en fonction de la température des différents matériaux a été menée sur la taille des fibreuse, la surface spécifique, la densité massique, ainsi que la quantité de l'eau structurelle et adsorbée, d'une part, et la structure cristalline d'autre part. L'utilisation des méthodes DRX et PL corrélées a permis d'expliquer une transformation de la phase α de l'UPA en mullite 2:1.

Le modèle proposé distingue deux principaux régimes de modification thermique de la structure des UPA: transport de masse sur la surface d'une fibre ou de la masse globalement (frittage). Des énergies d'activation du transport massique et des constantes pre-exponentielles ont été obtenues pour les deux régimes. Les résultats obtenus permettent de conclure que les transformations morphologiques, de la composition chimique et de la phase cristalline sont d'origine commune.

Mots clés*: alumine ultra-poreuse nano fibreuse, transformations de phase, silice modifiée, traitement thermique, morphologie, énergie d'activation.*